Mapping the Anatomical basis for motor control of a single vibrissa muscle across Rat Brain

Doctorate thesis

to obtain a doctorate (PhD)

from the Faculty of Medicine

of University of Bonn

Aman Maharjan

from Kathmandu, Nepal

2025

Written with authorization of
the Faculty of Medicine of the University of Bonn

First reviewer: Prof. Dr. Marcel Oberlaender

Second reviewer: Prof. Dr. Heinz Beck

Day of the oral examination: 07/07/2025

From the Max Planck Institute for Neurobiology of Behavior – caesar:

Contents

List of abbreviations

CNN	Convolutional Neural Network
CTB	Cholera Toxin subunit B
EDC	Extrinsic Digitorum communis
FN	Facial Nucleus
L5PN	Layer 5 Pyramidal Neurons
M1	Primary Motor Cortex
MNs	Motoneurons
NeuN	Neuron-specific nuclear binding protein
preMNs	premotor neurons
RCNN	Region-based Convolutional Neural Network
ResNet	Residual Network
S1	Primary Sensory Cortex
S2	Secondary Somatosensory Cortex
vMN	vibrissal Motoneurons

1 Introduction

Rat vibrissae are critical sensorimotor tools, enabling them to navigate, explore, and interact with their environment through highly specialized tactile feedback (Diamond et al., 2008; Mitchinson et al., 2006; Petersen, 2019). The sensory processing pathway of the rodent vibrissal system has been extensively studied due to the presence of anatomically distinct regions in brainstem, thalamus and cortex (Diamond et al., 2008; Petersen, 2007; Woolsey & Van der Loos, 1970). While the general mechanisms underlying vibrissae movement, such as rhythmic whisking, are well understood (Berg & Kleinfeld, 2003), the detailed pathways enabling precise, individual control of vibrissae remain to be studied. In this thesis, I investigate part of the neural system that enables flexible control of vibrissae movements.

The vibrissa motor control pathway is distributed across multiple neural levels, involving cortical, subcortical, and brainstem. It has its endpoint in the intrinsic and extrinsic muscles (Hill et al., 2008). These muscles are directly innervated by motoneurons (MNs) located in the facial nucleus (FN) of the brainstem (Herfst & Brecht, 2008). The MNs receive input from premotor neurons distributed across various brainstem nuclei, including the reticular formation and trigeminal sensory nuclei (Kleinfeld et al., 1999; Takatoh et al., 2013). Premotor neurons are, in turn, influenced by pre-premotor neurons located in cerebral cortex and higher-order brainstem regions (Takatoh et al., 2013).

In the next few paragraphs, I will review the anatomy of the rat vibrissa before delving into the muscles responsible for vibrissa movements, focusing on the roles of intrinsic and extrinsic muscles in generating protraction and retraction. Following this, I will discuss the control of vibrissa movements at different levels of the nervous system. Additionally, I will examine the challenges in investigating brain regions that control these muscles through pathways that extend beyond direct monosynaptic connections to motoneurons.

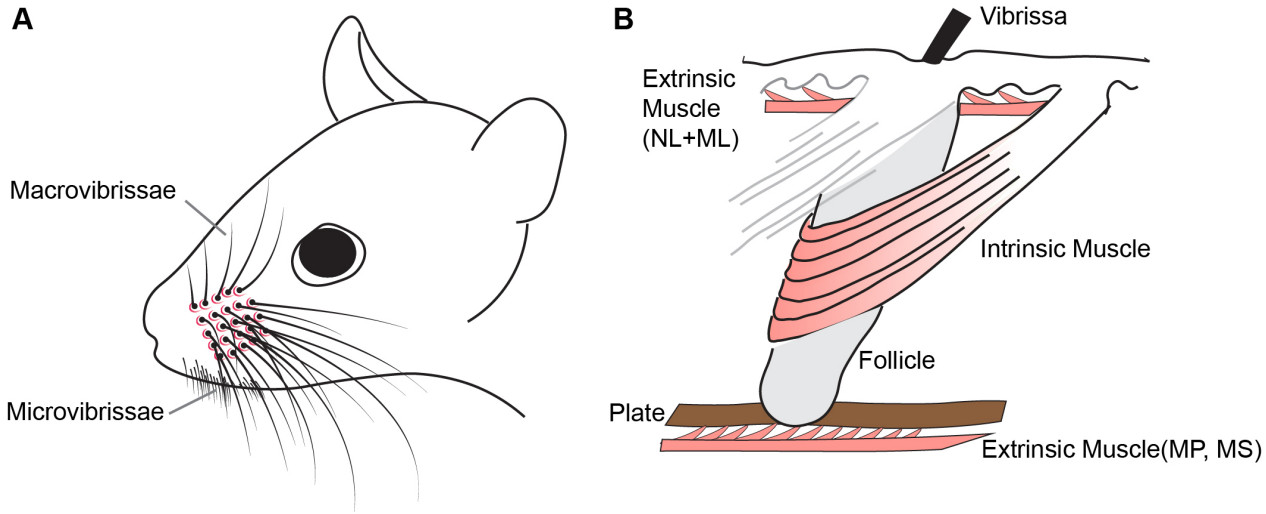

Figure 1: Schematic diagram of a rat whisker illustrating muscles involved in whisker movement. (A) Schematic representation of rat vibrissal array, illustrating macrovibrissae and microvibrissae. Macrovibrissae, located on the mystacial pad, are longer and arranged in an orderly grid of rows and arcs, while microvibrissae, located in external mystacial and lower jaw field, are smaller and less distinct, blending with fur hairs. (B) Schematic drawing of a vibrissa follicle, highlighting the associated intrinsic and extrinsic muscles. The intrinsic muscle forms a sling-like structure around the follicle, directly connecting adjacent vibrissa. The extrinsic muscles anchor the follicle to surrounding tissues. NL, *M. nasolabialis*; ML, *M. maxillolabialis*; MP and MS, Partes maxillares profunda and superficialis, respectively. Adopted from Dörfl, 1982; Haidarliu et al., 2010.

1.1 Overview of vibrissae and associated muscles

The rat vibrissa, or a whisker, is a stiff tapered hair embedded in a follicle-sinus complex in the skin of the rat's face, particularly along the upper lip (Wineski, 1985). There are two types of vibrissae based on size (Figure 1A): macrovibrissae and microvibrissae. Microvibrissae near the nose and lower jaw are shorter in length and are difficult to distinguish from fur. They function mainly in object recognition tasks (Brecht et al., 1997). Macrovibrissae, located on the mystacial pad, are arranged in an orderly grid of rows and arcs. The typical architecture of macrovibrissae includes four straddlers (α - δ) and five rows (A-E) of vibrissae. Each row contains from 4-7 vibrissae that are arranged in arcs (Dörfl, 1982). They are involved in spatial task but are not essential in object recognition (Brecht et al., 1997). The mystacial pad muscles are the primary drivers of vibrissae movement during whisking. These muscles are broadly classified into two types: intrinsic and extrinsic muscles.

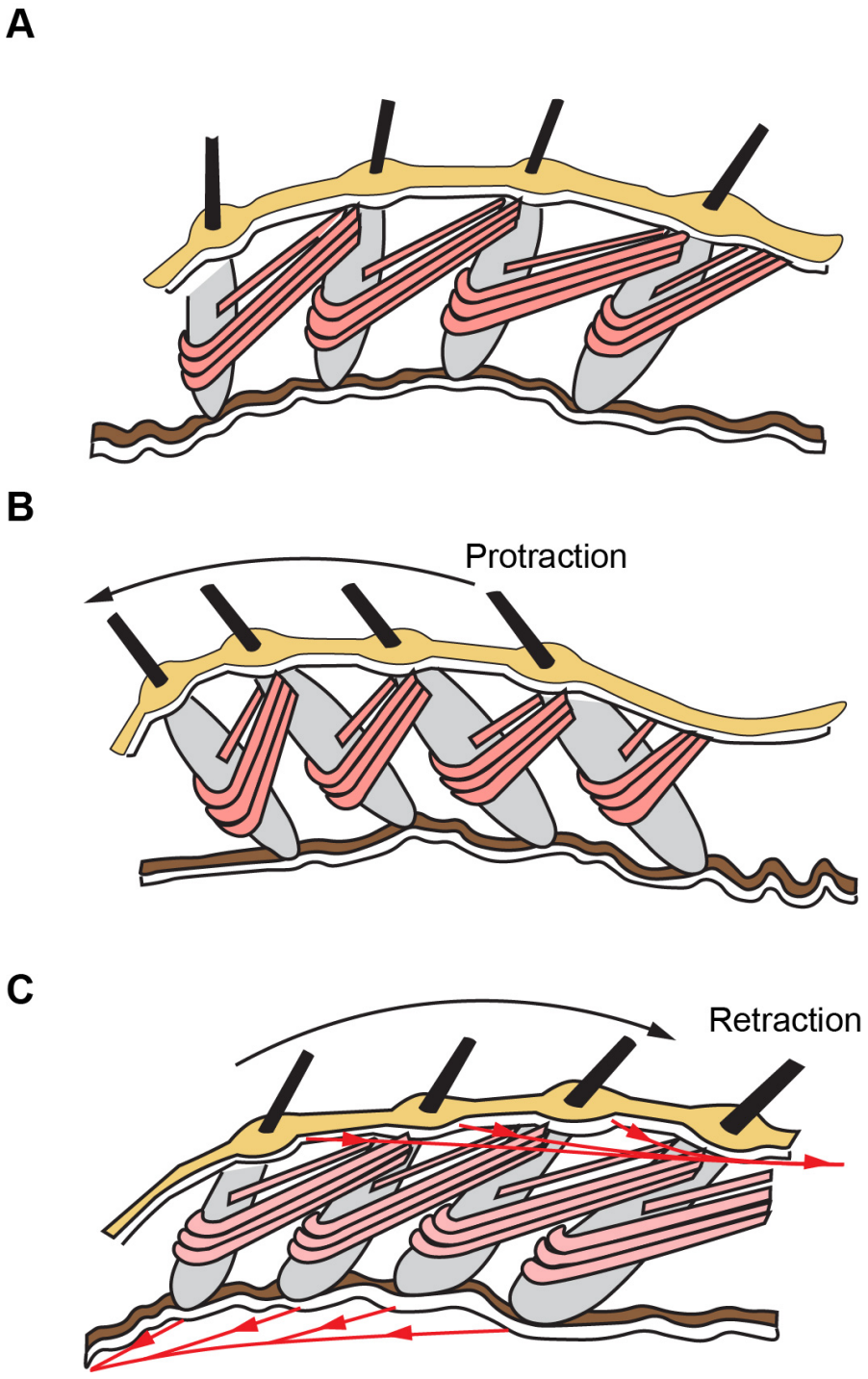

Figure 2: Various positions of the vibrissa follicles during vibrissa movement. (A) Position of the vibrissa follicles at rest within the mystacial pad (B) Protraction, forward movement, of the vibrissae driven by contraction of the intrinsic vibrissa muscle (C) Retraction, backward movement, of the vibrissae driven by contraction fo the superficial and deep extrinsic vibrissa muscles, represented by red arrows Adopted from Haidarliu et al., 2023.

The intrinsic muscle is small, tightly organized fibers that form a sling-like structure around the base of each vibrissa (Figure 1B) and connect to the adjacent follicle of the same row (Dörfl, 1982). It is only partially inserted into the corium and their position is radial within the mystacial pad (Haidarliu et al., 2010). The intrinsic muscle is primarily innervated by motoneurons located in the ventrolateral facial nucleus (Guest et al., 2018; Klein & Rhoades, 1985). The muscle contraction primarily drive the protraction of individual vibrissa (Figure 2B), allowing fine control over vibrissa movements (Haidarliu et al., 2023).

The extrinsic vibrissa muscles in rats are a group of muscles located superficial, radial as well as deep (Figure 1B) within the mystacial pad (Haidarliu et al., 2010). *Nasolabialis*, *Maxillolabialis*, *Nasolabialis superficialis* and *Buccinatorius* Pars are the superficial muscles. Pars media superior and Pars media inferior part of *Nasolabialis profundus* muscle are the radial muscles. And Pars interna profunda, Pars maxillaris superficialis and Pars maxillaris profunda of *Nasolabialis profundus* are the deep muscles. These muscles are connected to the skin and surrounding structures, rather than being directly attached to the vibrissa follicles like the intrinsic muscle. The extrinsic muscles are innervated by motoneurons located in the dorsolateral facial nucleus (Klein & Rhoades, 1985). Together these muscles contribute to the generalized movement of vibrissae, such as rhythmic whisking and retraction (Figure 2C).

When mapping the anatomical basis of motor control for a single muscle, intrinsic muscle serve as a better study model than extrinsic muscles. Because of the direct attachment of intrinsic muscle to the vibrissa, each muscle is specialized to protraction of an individual vibrissa. Consistent with the anatomical findings, stimulation of the single vMNs could evoke protraction of a single vibrissa (Herfst & Brecht, 2008). This allows for correlation of the anatomical pathway and specific vibrissa control. In contrast, extrinsic muscles coordinate movements across multiple vibrissae as well as broader facial area. Also, a single clear localized intrinsic muscle simplifies experimental approach and reduces the variability over broad extrinsic muscles.

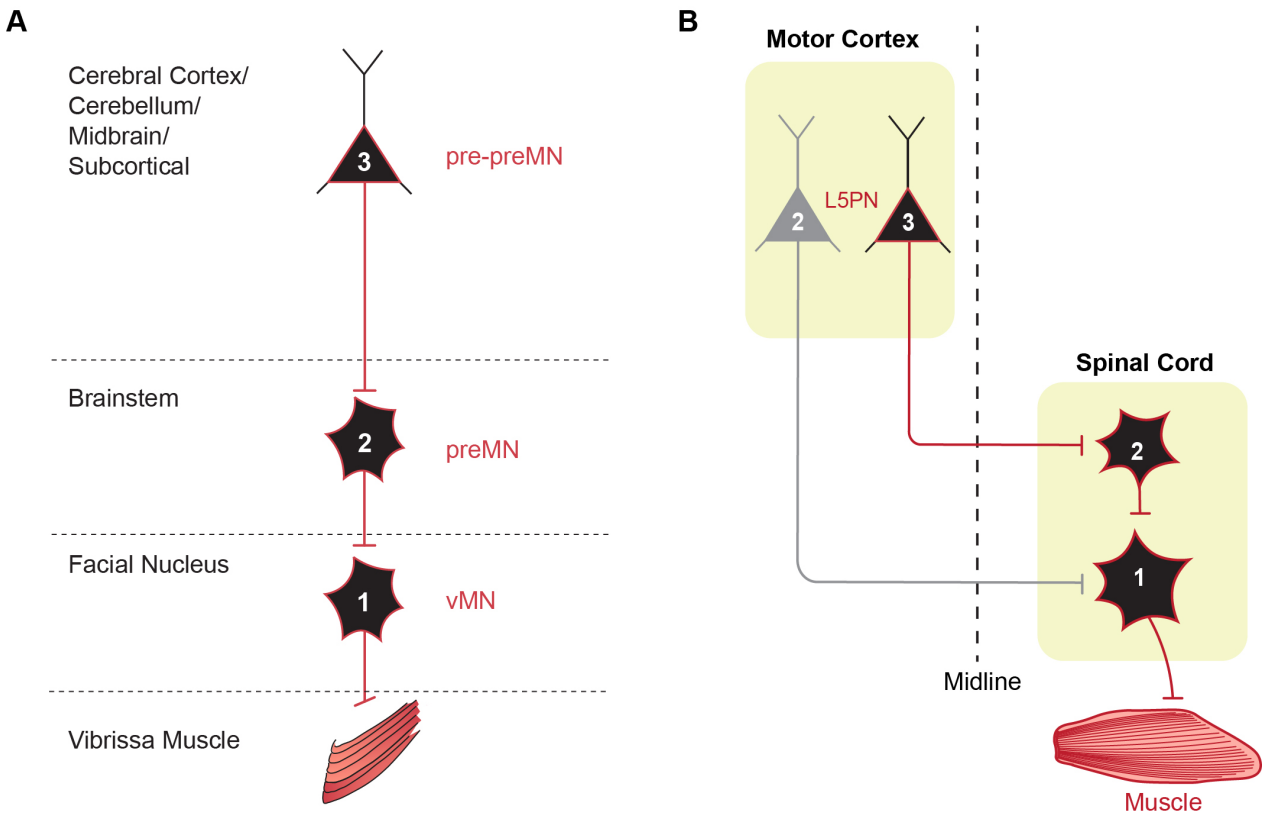

Figure 3: Schematic overview of the vibrissa motor control pathways. (A) A vibrissa motor control pathway include motoneurons (vMNs) in the facial nucleus, premotor neurons (preMNs) in the brainstem, and pre-premotor neurons (pre-preMNs) in the cerebral cortex, cerebellum, midbrain, and subcortical regions. (B) Monosynaptic pathways, such as those for primate finger movements, provide direct cortical input from L5PN to motoneurons, while disynaptic pathways, seen in rodent whisker muscles and other primate muscles, involve premotor neurons.L5PN, pyramidal neuron in layer 5; vMN, vibrissa motoneuron; preMN, premotor neuron; pre-preMN, pre-premotor neuron; 1, first-order neuron; 2, second-order neuron; 3, third-order neuron. Adopted from Rathelot and Strick, 2006.

1.2 Control of vibrissa movement

Vibrissal Motoneurons (vMNs) are the final common pathway for execution of vibrissa movement (Figure 3A). The vMNs that control the muscles involved in vibrissa movement are located in the lateral facial nucleus (Ashwell, 1982; Herfst & Brecht, 2008). Approximately 60 vMNs dedicated to each intrinsic muscle are located in the ventrolateral part of the facial nucleus (Guest et al., 2018; Klein & Rhoades, 1985). These vMNs are organized in a slab-like structure with a row-specific arrangement. The vMNs for A-row vibrissae are

positioned laterally and those for E-row are located medially (Guest et al., 2018). Interestingly, the dendrites of these vMNs extend beyond their soma location into a medial-caudal region of the FN. Despite this, dendritic fields of the vMNs remain largely disjoint (Guest et al., 2018) which may contribute to the precision of motor control for individual vibrissae.

Lateral facial nucleus receives input from several premotor brain regions in brainstem (Figure 3A). The premotor neurons play a critical role in controlling whisker movements by serving as intermediaries between higher motor region and motoneurons in the facial nucleus (Moore et al., 2013; Takatoh et al., 2013). The rhythmic whisking is mediated by the vibrissal intermediate reticular nucleus(vIRt). The non-rhythmic whisking is controlled by diverse premotor centers in the reticular formation, spinal trigeminal subnuclei (Sp5), and other brainstem nuclei (Deschênes et al., 2016; Hattox et al., 2002; Isokawa-Akesson & Komisaruk, 1987; Kleinfeld et al., 2014; Mercer Lindsay et al., 2019; Moore et al., 2013). Anatomical evidence from retrograde tracing (Takatoh et al., 2013) and physiological evidence from microstimulation (Sreenivasan et al., 2015) demonstrate that IRt primarily controls vibrissa protraction through intrinsic muscle , while Sp5i retracts vibrissa via extrinsic muscles.

Premotor neurons are diverse and receive motor commands from cortical, subcortical, midbrain and cerebellar regions (Figure 3A). Among these structures, the ability to generate and control movement is a hallmark feature of the cerebral cortex, and the basis for flexible behavior in mammals. The most direct pathway for cortical control of movement is established by pyramidal tract neurons in layer 5 (L5PTs), which send descending axons to the spinal cord or brainstem (Figure 3B) (Takatoh et al., 2013). However, it has become increasingly clear that the corticospinal and corticobulbar neurons do not form direct connections with the motoneurons (MNs). Monosynaptic connections appear to be specific for hand muscles in primates with dexterous finger movements In contrast,general motif for cortical control of movement is disynaptic , where cortical outputs from L5PNs are relayed through premotor neurons in the brainstem or spinal cord before reaching motoneurons

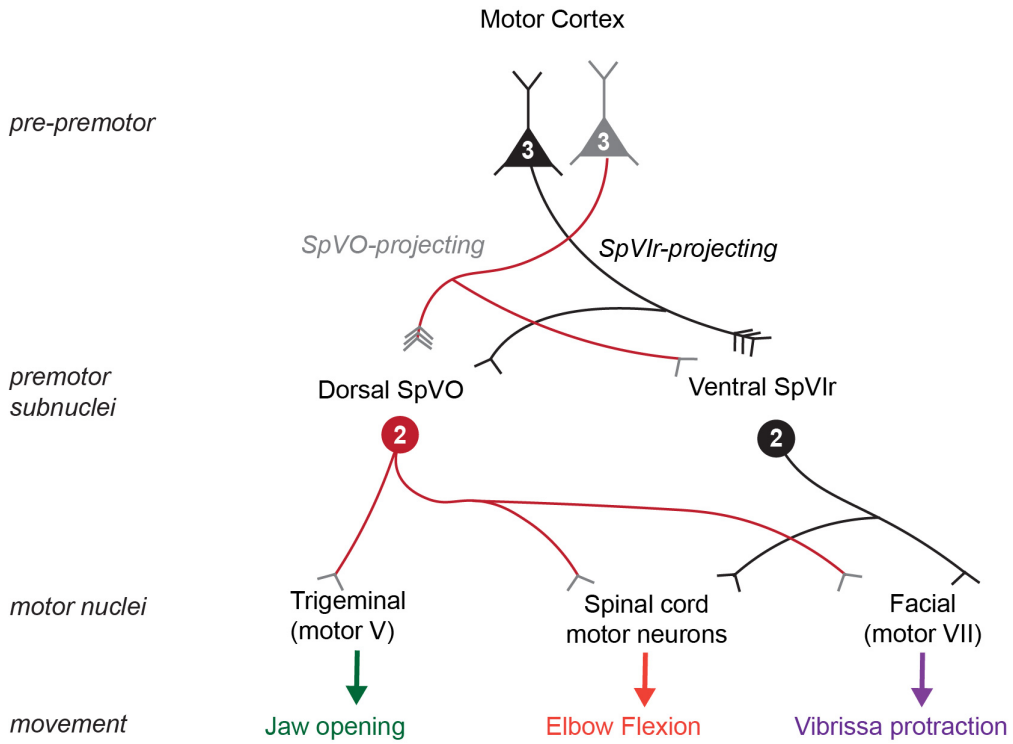

Figure 4: Complexity of muscle control at the brainstem level for whisker and other muscles. The model summarizes the complex neural circuitry in the brainstem that controls whisker muscles and other muscles in rodents. Neighboring neurons in motor cortex send signals to the brainstem, where intermediary neurons relay commands to motor neurons. SpVO, Spinal trigeminal par oralis; SpVIr, Spinal trigeminal interpolaris rostralis. Adopted from Mercer Lindsay et al., 2019.

(Figure 3B) (Matyas et al., 2010; Mercer Lindsay et al., 2019; Sreenivasan et al., 2015). This disynaptic networks can display an enormous complexity. For example, single L5PTs in M1 were recently found to connect to diverse sets of premotor neurons that are distributed across several subareas of the spinal trigeminal nucleus (Sp5) (Mercer Lindsay et al., 2019). And each preMN connected to diverse sets of MNs, which innervate a variety of muscles, often spanning different body parts (Mercer Lindsay et al., 2019). The specific populations of preMNs and consequently MNs that are innervated by a L5PN varies, even between neighboring L5PNs (Figure 4). Stimulating single L5PNs in M1 hence results in cell-specific activation of diverse sets of muscles, including different facial and forelimb muscles. Thus, a major challenge in understanding the cortical control of vibrissa movements lies in the need to reconstruct disynaptic L5PN to vMN pathways with cellular level

and single-muscle resolution.

The primary focus of this thesis is to map the anatomical basis of motor control, with a specific emphasis on understanding the organization of disynaptic pathways connecting the cerebral cortex to motoneurons. For this purpose, I used rabies virus, a retrograde transneuronal tracer (Kelly & Strick, 2000, 2003). The virus initially infects motoneurons that project to the site of injection and directly innervate the target muscle. From the motoneurons, it travels retrogradely to infect upstream premotor neurons that provide input to these motoneurons. Subsequently, the virus continues to spread retrogradely to cortical neurons that are disynaptically connected to the motoneurons via these premotor neurons. This stepwise tracing enables detailed identification of cortical and subcortical networks involved in motor control.

I report that the most direct cortical outputs to a single facial vibrissa muscle originate from regions within the primary motor cortex (M1) as well as from areas outside M1, including the primary somatosensory cortex (S1, also known as the ”barrel cortex”), secondary motor cortex (M2), secondary somatosensory cortex (S2), and the anterior insular cortex (AI). Over 60% of the cortical output arises from areas outside M1. Except for the S1 barrel cortex, output from all these cortical regions operates bilaterally, with each vibrissa muscle receiving nearly equal descending inputs from M1, M2, S2, and AI in both hemispheres. Within M1, subregions show differential contributions to either contralateral or ipsilateral vibrissa muscle control, further emphasizing the distributed nature of cortical motor outputs. To explore whether a similar distribution of cortical control exists for another muscle, rabies virus was injected into forepaw muscles. The results indicate that the distribution of cortical control differs between muscles: in M1, forepaw and whisker muscle representations partially overlap; in S1, they are disjoint; and in M2 and S2, they fully overlap. Interestingly, unlike the whisker muscles, forepaw control showed no labeling in the anterior insular cortex. These findings demonstrate the unique and muscle-specific organization of cortical areas involved in motor control.

2 Material and methods

The methods in this thesis are adapted from Guest et al., 2018, incorporating established protocols for tracing, injection techniques, reconstruction, and data analysis. These methods are reliable for mapping multitransynaptic anatomical pathways. To improve efficiency, machine learning algorithms for neuron detection were tested.

2.1 Experimental

2.1.1 Injections

Experimental procedures were conducted at the University of Pittsburgh in compliance with animal welfare guidelines of the Max Planck Society and the National Institutes of Health. Approvals were obtained from the Institutional Animal Care and Use and Biosafety Committees. Rabies virus and animal handling protocols were based on established guidelines (Kelly & Strick, 2000; Tang et al., 1999) and exceeded the Department of Health and Human Services recommendations for Biosafety in Microbiological and Biomedical procedures.

2.1.1.1 Vibrissa muscle injections

Male Wistar rats aged postnatal days 28-35 (P28-35) were anesthetized using an intraperitoneal injection of a ketamine-xylazine mixture (70/6 mg/kg). The rats were then secured in a stereotaxic frame (Helmut Saur Laboratories). The fur around the target C3 vibrissa was trimmed, and a small incision was made adjacent to the follicle. To optimize visualization of the mystacial pad, the rat's head was tilted 20˚ upward in the ventral-dorsal direction and observed under a surgical stereoscope (Leica MZ6). The C3 vibrissa was visually identified and marked at its base with a surgical pen. Using a manual manipulator (Narishige Model BE8), a steel injection needle connected to a Hamilton syringe was inserted approximately 1 mm below the surface at the follicle base. A volume of 500-700 nL of ra-

bies virus (N2c strain, 1x10⁹ pfu/mL, provided by M. Schnell, Thomas Jefferson University) was pressure-injected under visual guidance. Following the injection, rats were allowed to survive for 3-5 days post-injection. During this period, no observable symptoms were noted.

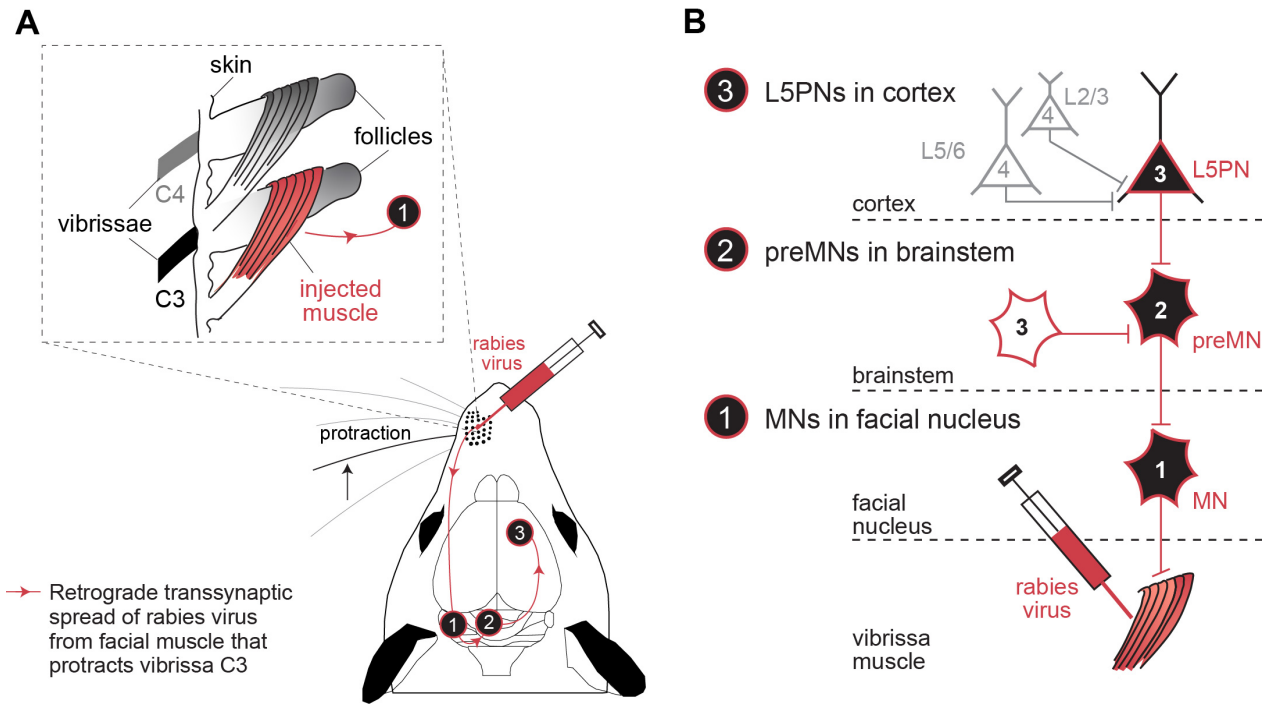

Figure 5: Schematic of rabies virus injection into rat whisker muscle and expected synaptic labeling. (A) Wild-type (N2c) rabies virus was injected into a single intrinsic muscle that protract the C3 whisker. (B) Retrograde transsynaptic spread of rabies virus from the muscle infects first motoneurons (MNs) in ventrolateral facial nucleus, then pre-motor neurons (preMNs) in brainstem, then pyramidal neurons in cortical layer 5 (L5PNs), and then neurons beyond L5 (e.g. in L2/3) – i.e., 3rd-order brains have rabies labeling restricted to L5.

2.1.1.2 EDC muscle injections

A volume of 45-50 µL of N2c rabies virus (>10⁸ pfu/mL) was injected into the extensor digitorum communis (EDC) muscle of the right forelimb in Sprague Dawley rats. Rats were allowed to survive for 3 days post-injection to allow the virus to propagate within the neural circuits. Starting 3 days after the injection, rats were transcardially perfused with Phosphate Buffer (PB) at 12-hour intervals. Following perfusion, brains were carefully

extracted and fixed overnight in 4% paraformaldehyde (PFA) to preserve the tissue for subsequent analysis.

2.1.2 Histology

For vibrissa injections, the brains were first cut into two parts: a frontal section containing the cortex and a caudal section containing the cerebellum and brainstem. The caudal section was sliced into consecutive 50 µm thick coronal slices using a vibratome. The frontal section was sliced either coronally or tangentially. For tangential sections, the right and left hemispheres were blocked separately, and slices were cut tangentially to vS1 at a 45° angle to the midline. To permeabilize and block the slices, they were incubated in 100 mM phosphate buffer (PB) supplemented with 4% normal goat serum (NGS) and 0.5% Triton X-100 (TX) for 2 hours at room temperature. This process prepared the sections for antibody staining. Following permeabilization, the slices were incubated with primary antibodies. Rabbit anti-NeuN (1:500) and Mouse anti-RABV-P 31G10 (1:1000, 2 mg/mL) were diluted in PB containing 1% NGS and applied to the sections. The incubation lasted for 48 hours at 4°C to ensure specific binding of the antibodies to their targets. After the primary antibody step, secondary antibodies were applied. Goat anti-mouse IgG Alexa-488 (1:500) and goat anti-rabbit Alexa 647 (1:500) were diluted in PB supplemented with 3% NGS and 0.3% TX. The slices were incubated with these antibodies for 2-3 hours at room temperature to visualize the labeled proteins. Finally, the slices were mounted onto glass slides. To preserve the samples and optimize imaging quality, the slides were embedded in Slowfade Gold and covered with a coverslip.

For EDC injections, the brains were sliced into coronal sections. These sections were then distributed systematically across ten separate wells for further processing. Every tenth section was stained with Nissl stain to visualize the general cellular architecture. The remaining sections were processed using the avidin-biotin peroxidase system (Vectastain, Vector Laboratories) to prepare them for immunolabeling. Rabies-infected neurons were

identified by applying a monoclonal antibody targeting the nucleoprotein of the rabies virus.

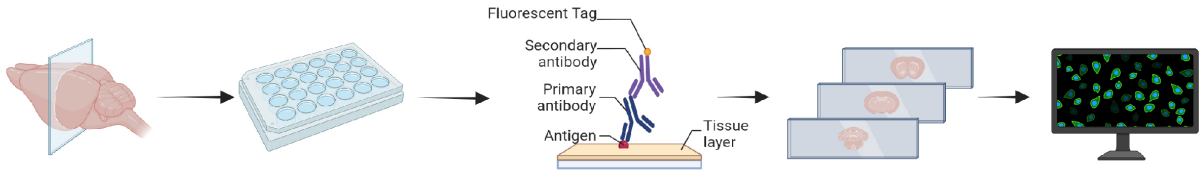

Figure 6: Schematic of tissue processing steps for brain slicing, staining, and confocal imaging. The brain was sectioned into 50 µm slices and transferred to a well plate. The sections were then double immunolabeled. After staining, the tissue was mounted onto slides and imaged using confocal microscopy

2.1.3 Image acquisition

For vibrissa injections, imaging was conducted using a confocal laser scanning system (Leica Application Suite Advanced Fluorescence SP5; Leica Microsystems) equipped with a resonance scanner and spectral detectors with hybrid GaAsP photocathode technology. Mosaic scanning software (Matrix Screener, provided by Frank Sieckmann, Leica Microsystems) facilitated the acquisition of high-resolution images. Dual-channel mosaic scans of entire brain sections were captured using a 10x glycerol-immersion objective (HC PL APO 10x, 0.04 N.A) at a resolution of 0.868 x 0.868 µm per pixel, with 1.7x digital zoom, 8x line averaging, and an 8-kHz scanning speed.

For EDC injections, imaging was conducted using a brightfield microscope system (BX51, Olympus) equipped with advanced mosaic scanning software (Surveyor) to ensure comprehensive coverage of brain sections. Mosaic images were captured using a 10x dry objective lens, which provided a resolution of 0.926 x 0.926 µm per pixel.

2.2 Reconstruction and alignment

Amira software was utilized to generate 3D reconstructions of complete brains (Stalling et al., 2005). Images from each brain slice were imported into the software, where Rabies-

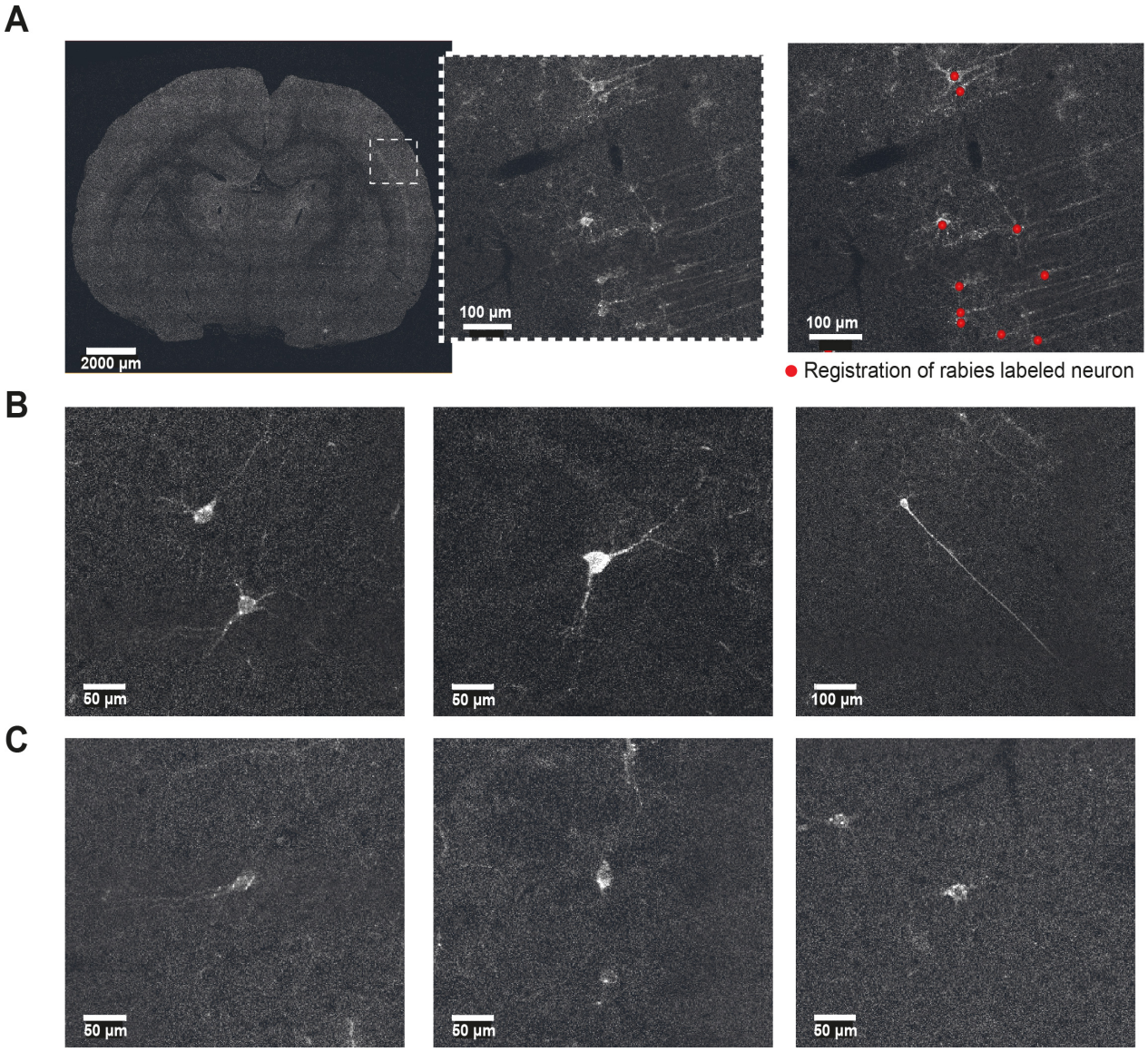

Figure 7: Example images of rabies-infected neurons and landmark identification using Amira software. (A) Rabies-infected neurons are distinguished from background noise by their infected cellular structures, including the soma and dendrites. Left: Coronal brain slice. Middle: Zoomed-in section of the cortical layer from the slice. Right: Identified neurons infected using Amira software. (B) Examples of strongly rabies-infected neurons displaying distinct structural features. (C) Examples of weakly rabies-infected neurons.

488-stained images were used to identify rabies-infected neurons, and NeuN-677-stained images were used to outline the pia and delineate brain regions (Dercksen et al., 2014). Additionally, Viewer software, developed in Pittsburgh, was employed to enhance visualization through its intuitive interface, enabling a detailed examination of brain morphology. The specific methods for identifying rabies-infected neurons, delineating brain regions, and

aligning reconstructed brain slices will be discussed in the following paragraphs.

2.2.1 Detection of rabies-infected neuron

Rabies-488-infected images of each brain slice, acquired using an SP5 confocal microscope, were used to locate rabies-infected neurons involved in muscle control of injected vibrissae intrinsic whisker muscle. The images were loaded in Amira software. The resolution notations applied to maintain a consistent standard size across slices (Stalling et al., 2005). The landmark function in the software was used to annotate the neuronal cell bodies, somata. Some neurons exhibited strong structural features such as visible dendrites, while others displayed weaker labeling of the cell nucleus and cellular structure. Annotations were made regardless of variability in labeling intensity and primarily focused on the visibility of somata. This approach facilitated consistent detection across brain sections and ensured reliable comparisons between different experimental datasets.

2.2.2 Outline of the brain region

Outlines or contours of the brain sections were drawn manually using the Filament Editor in Amira Software (Dercksen et al., 2014). In the same outline file, brain areas were labeled based on the Paxinos Rat Brain Atlas (Paxinos & Watson, 2006). High-resolution confocal images as well as wide-field images were used for the coronal sections and tangential sections respectively. The barrel columns are better visible in the wide-field images as these sections were cut tangential to vS1 in each hemisphere. In every tangential sections outline file, pia, barrel columns, blood vessels and white matter was reconstructed. In coronal section files, all the brain regions relevant in the motor control pathway was reconstructed. For example - the border separating motor, somatosensory and insular cortex were determined based on the cytoarchitecture visible in the NeuN labeling. Border between motor and somatosensory cortex were distinguished based on absence and presence of layer 4. And border between sensory and insular cortex were made based on the location above rhinal fissure and reduction in layer thickness.

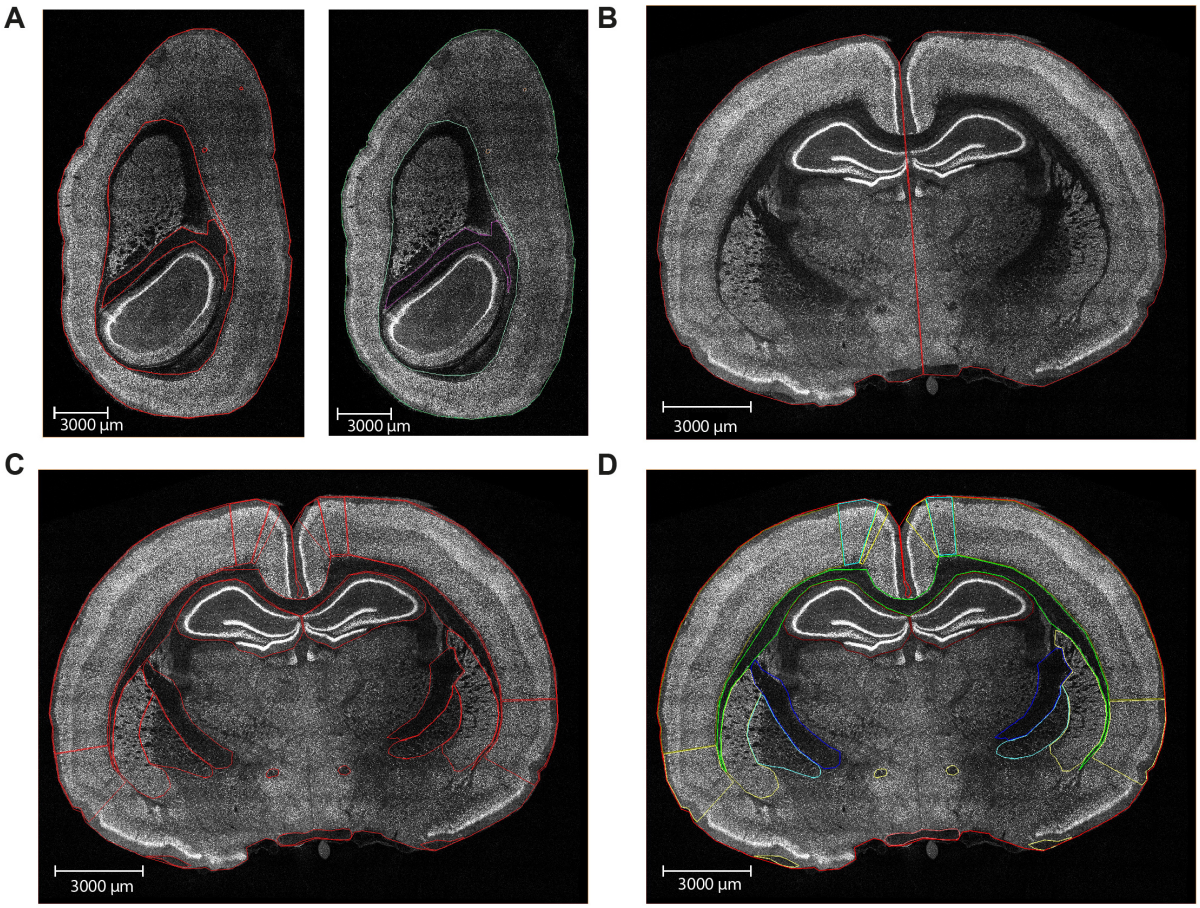

Figure 8: Example images of tangential and coronal brain tissue sections with brain areas outlines and labeling. (A) Example contours in a tangential slice. Left: Pia and white matter were contoured. Right: Contour assigned to different brain regions based on the Paxinos reference atlas. (B) Example contours of the cortex, separating the hemispheres using imaginary midline. (C) Example contours of the pia and subcortical structures in the same slice shown in (B). (D) Example contours assigned to different brain structures based on the Paxinos reference atlas, providing anatomical alignment for analysis.

2.2.3 Alignment of brain slices

Alignment of the coronal brain sections and tangential brain sections were done using two different methods. The coronal brain section outlines were aligned with respect to the midline and in reference to the sagittal brain from Paxinos Rat Brain Atlas. In brain sections with cortex, upper boundary of each outline was fitted to the standard curvature from the upper boundary of the corresponding sagittal plane of the cortex from atlas. And in brain

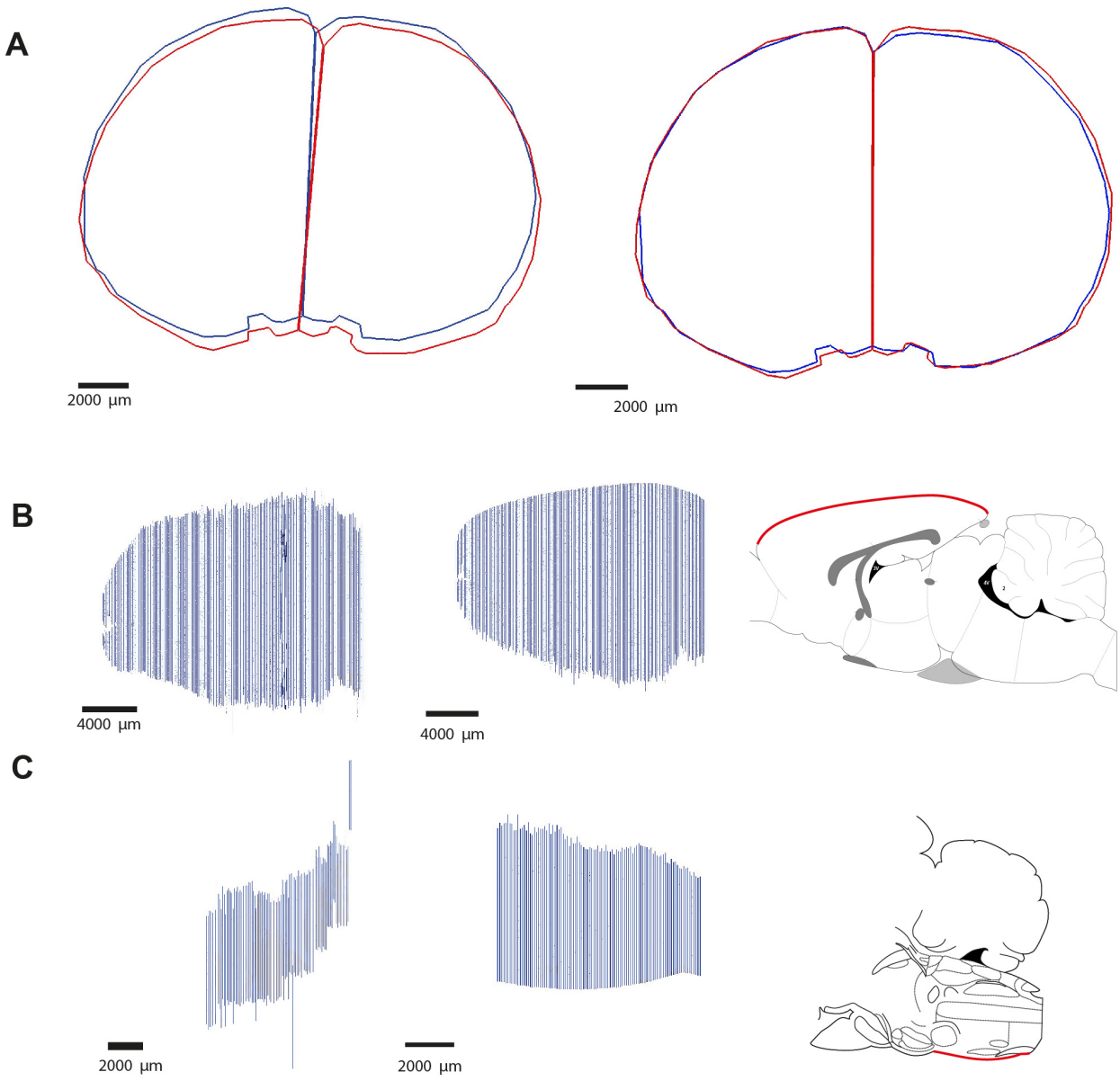

Figure 9: Manual and automatic alignment procedures for brain slice outlines. (A) Alignment of contours from two consecutive brain slices. Left: Two contours before alignment. Right: Upright adjustment of the contours, making the midline perpendicular to the horizon. (B) Sagittal view of the cortex contours before and after height adjustment. Left: Before height adjustment. Middle: After height adjustment. Right: Sagittal view of the reference atlas. The highlighted red line is used as a reference to align the highest points of the cortical slices. Adopted from Paxinos and Watson, 2006. (C) Sagittal view of the brainstem contours before and after height adjustment. Left: Before height adjustment. Middle: After height adjustment. Right: Sagittal view of the reference atlas. The highlighted red line is used as a reference to align the lowest points of the brainstem slices. Adopted from Paxinos and Watson, 2006.

sections with brainstem, the lower boundary of each outline was fitted to the standard curvature from the lower border of the corresponding sagittal plane of the brainstem from the atlas. However, the tangential brain section outline were aligned by blood vessel patterns (Egger et al., 2012). After alignment, outlines were converted into surfaces and smoothed using 'Smooth Surface' in Amira (iterations: 20, lambda: 0.6).

The landmark file consisting of the coordinates of the rabies-infected neurons were then aligned based on the transformation file generated when aligning the outline files. After the transformation, the whole brain reconstruction of each experiments with detailed rabies-infected neurons coordinates were generated.

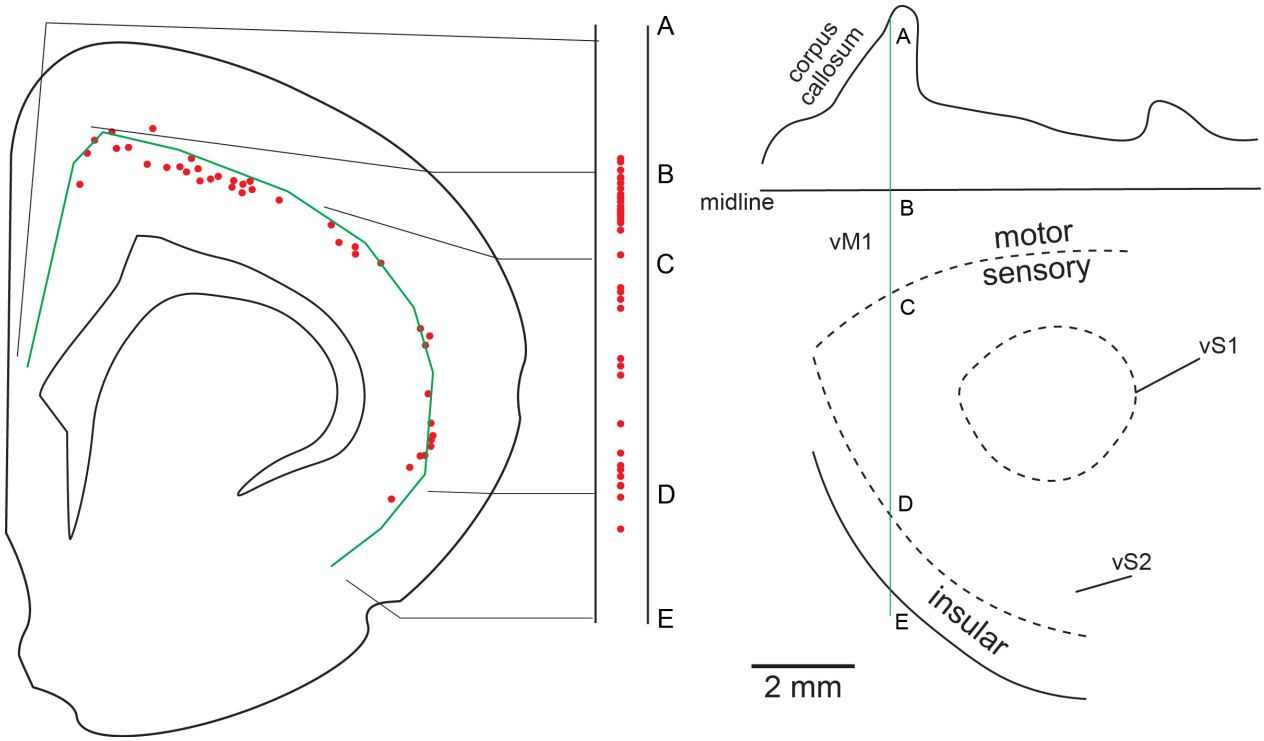

Figure 10: Flattened reconstruction of the cortex constructed from coronal slices. Half of a coronal section of the cortex (left) were straightened (middle) to form a flattened reconstruction (right) of the cortex. The red circle represents the rabies-infected neurons in the layer 5 of the cortex. Capital letters on the middle panel and on the vertical line in the reconstruction indicate the cytoarchitecture boundary. The vertical green line on the reconstruction indicates the level of the section displayed on the left. Each section was aligned on the junction of the medial wall with the lateral surface (i.e., the midline). Dashed line indicates the cytoarchitecture boundary in the cortex. vM1, vibrissa Primary motor cortex; vS1, vibrissa primary somatosensory cortex; vS2, vibrissa secondary somatosensory cortex Adopted from Dum and Strick, 1991.

2.2.4 Flat map reconstruction

To compare the distribution of rabies-infected neurons in cortex, flat maps of cortex were reconstructed using ReconWin software (Dum & Strick, 1991). All the outline of the brain sections with the coordinates of the neurons were uploaded to the ReconWin software. Because all the third-order brains had only neurons labeling of layer 5 neurons, these layer 5 neurons in the cortex were projected to a predefined line in layer 5. Brain markers such as corpus callosum, midline, rhinal fissure, somatosensory-motor line were marked on the line based on the cytoarchitecture. Therefore, for every brain sections, this resulted in a line consisting of markers and neurons in-between the markers corresponding to the cortical location. When all the sections are aligned based on the midbrain, we get a flat map like in (Figure 10) . For the quantitative analysis of the disynaptic projections from the cortex, this two-dimensional map is interpretable. Additional features can be calculated with this software, such as the density mapping to compare total neurons distribution within 100 μm.

2.3 Machine learning

In the experiments where the rabies-infected neurons have spread beyond just the layer 5 of the cortex, the total of rabies-infected neurons in the whole brain also increase dramatically. Due to this reason, manual annotation becomes impractical and laborious to complete. To tackle this challenge, I formulated it as an object detection task (Figure 11). A machine learning model was used to label the rabies-infected neurons across experiments, with high performance metrics. The training of the machine learning model was done using the viewer software developed in the laboratory of Prof. Strick.

2.3.1 Dataset

The manually labeled landmarks in the second-order, third-order and fourth-order experiments were used as the training dataset for the machine learning model. All the rabies-488

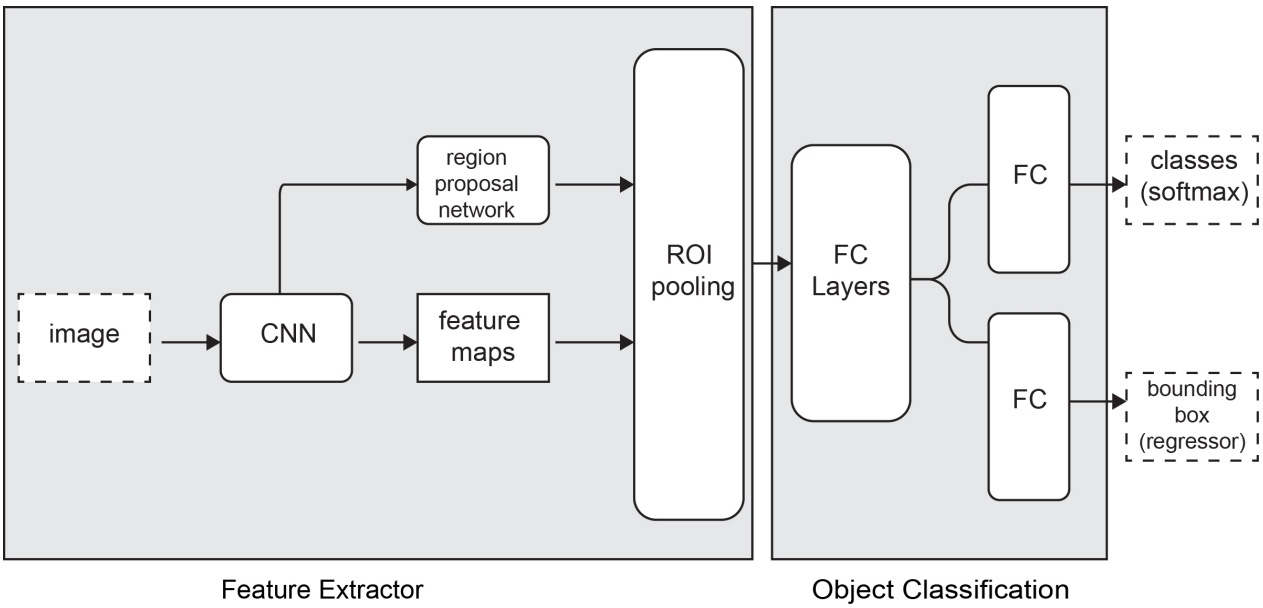

Figure 11: Schematic of the Faster R-CNN architecture. The input image is processed by a CNN to generate feature maps. A region proposal network (RPN) identifies regions of interest (ROIs), which are passed through ROI pooling to extract fixed-size feature maps. These features are classified to identify objects, and a bounding box regressor refines their spatial localization.

images and NeuN-648 images were uploaded to the viewer software. The coordinates of rabies-infected neurons from the Amira software were compiled in a json file. These files were used as the ground truth. In the viewer software, a bounding box of size 60 µm x 60 µm was created with the landmark coordinate at the center of the box. The bounding box captured the more than 80% of the somata of the rabies-infected neurons. All the bounding boxes with neurons were utilized in the training phase of the neural network model.

2.3.2 Algorithm

The faster Region-based convolutional neural network (faster-RCNN) algorithm was utilized for object detection. It is an improved version of RCNN. The workflow is explained below.

The rabies-488 high resolution confocal images of brain sections were used for the analysis. This algorithm includes a regional proposal network (RPN) that identifies potential areas where neurons might exist. The image is passed through a CNN backbone - residual

network (ResNet) which extracts important features (Girshick et al., 2014). The features may include the neuron shapes, boundaries and fluorescence intensity. In each proposed region, the classification determines if the region contains neuron or background, and spatial boundaries (bounding boxes) of detected neurons are adjusted for accuracy. After the processing, the algorithm outputs neuron labels, bounding boxes and confidence scores. The bounding boxes mark the exact locations of neurons. The confidence score of each neuron is measured as the probability of correct detection.

A Faster-RCNN Model performance was evaluated comparing predicted bounding boxes with ground truth annotations. Detections with a confidence score exceeding 0.85 were considered positive. A detection was classified as true positive if the Intersection over Union (IoU) between the predicted and ground truth bounding boxes was greater than 0.6. Performance metric, including recall, precision, and F1 score, were calculated to assess the efficacy of each model.

The test datasets for the Faster RCNN model consisted of every 10th coronal brain section. A total of 11 slides were used from frontal to caudal direction. This sample datasets provides a representative datasets for evaluating model's performance in neuron detection across different cortical regions.

2.4 Data analysis

All statistical tests and significance values are reported in the Results section. Sample sizes are provided in the Results or figure legends. Unless otherwise specified, data are presented as mean ± standard error of the mean (SEM). Statistical analyses were conducted using MATLAB, Python, and Prism software, with significance defined as $p < 0.05$. No data were excluded from the study.

3 Methodological results

The results are divided into two main chapters: methodological results and biological results. The methodological results focus on the classification of experiments into second, third and higher synaptic order based on the retrograde transsynaptic transport of rabies virus. Two second-order brains have been previously described in Guest et al., 2018. I also analyzed the performance of the machine learning models for object detection, focusing on its accuracy in detection of rabies virus-infected neurons in higher-order brains.

3.1 Classification of synaptic order

A total of 18 brains were collected following injection of rabies virus into intrinsic vibrissa muscle(n=15) and extensor digitorum communis (EDC) muscle (n=3) of the rat. In all three brains from EDC muscle injections, rabies-infected neurons were restricted to layer 5 of cerebral cortex. In all the brains from vibrissa injections, rabies-infected neurons were observed outside the ventrolateral facial nucleus. These brains were systematically categorized into synaptic orders—second, third, and higher based on the distribution of rabies-infected neurons in different brain regions such as facial nucleus, brainstem and layer 5 of cerebral cortex. I will describe them in following sections.

3.1.1 Second-order brains

In the second-order brains (n = 2), rabies-infected neurons were restricted in the brainstem (Figure 12A). i.e, there was no rabies-infected neurons in the cortex, cerebellum, and midbrain (Figure 12D). The total number of rabies-infected neurons remained relatively low (n= 138 and n= 896). Further analysis confirmed that these infected neurons are located in several brainstem nuclei that have been previously identified, including those previously reported to be presynaptic to vibrissa motoneurons (vMNs) (Takatoh et al., 2013) or to facial motoneurons in general (Hattox et al., 2002). Additionally, the number of infected neurons

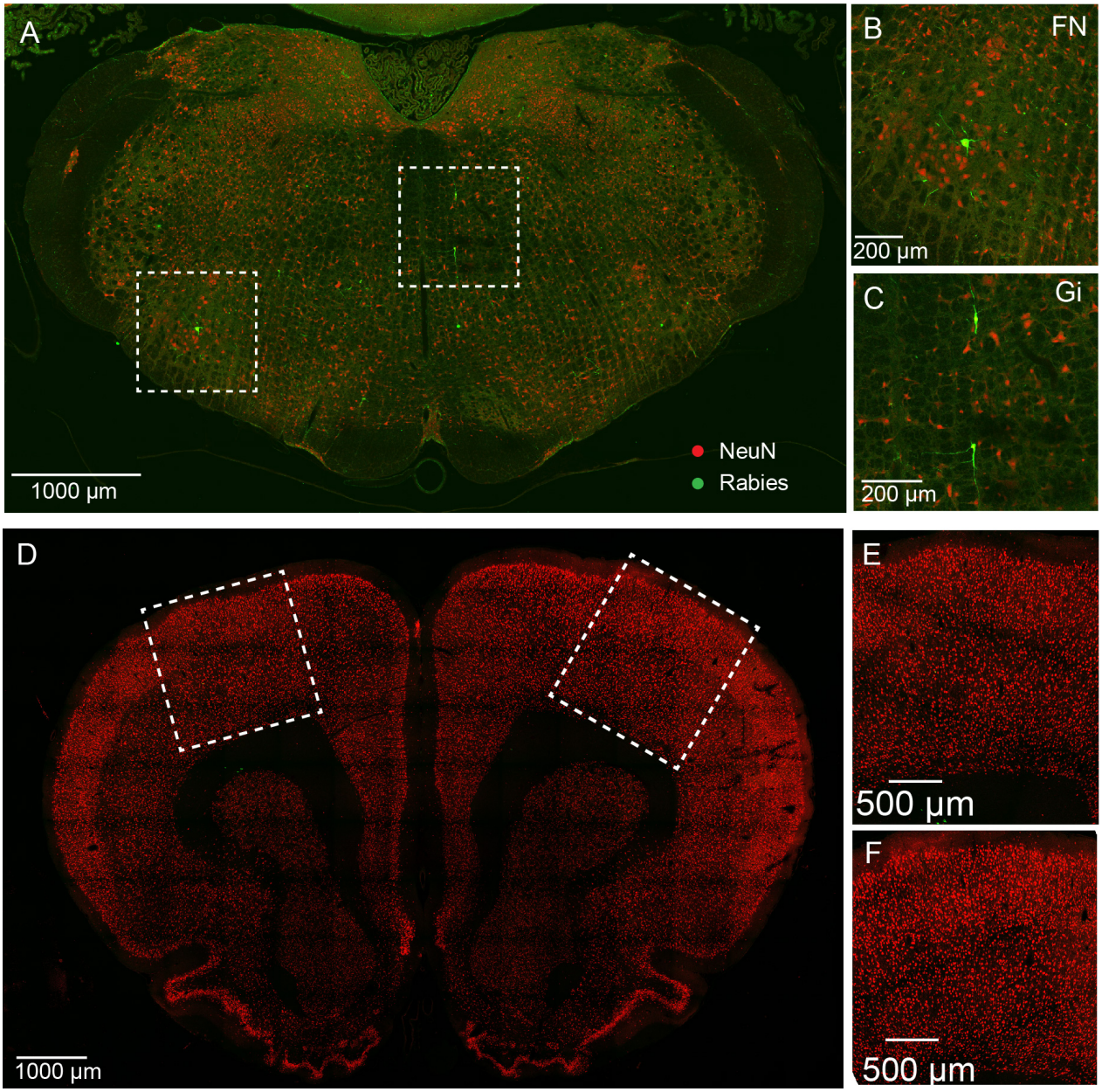

Figure 12: Example confocal images of rabies virus-infected neurons in a second-order brain. (A) Brainstem: rabies-infected neuron in facial nucleus (B, zoomed image showing MNs) and Gigantocellular reticular nucleus (C, zoomed image showing premotor neurons). (D) Cortex: No labeling is observed in cortex. Ipsilateral M1/S1 (E) and Contralateral M1/S1 (F).

is asymmetrical between hemisphere (ipsilateral = 830, contralateral = 204). Ipsilateral hemisphere has four times more infected neurons than the contralateral hemisphere.

Within the ipsilateral facial nucleus (FN), infected motoneurons (MNs) were restricted to the ventrolateral region, with only a small subset of infected MNs (n=6 and n=3). Notably, no

labeling was found in the contralateral FN, indicating that MNs controlling a single muscle of vibrissa do not form direct inter-hemispheric projections. The limited number of infected MNs further support notion that vibrissa motor control circuit is highly specific, targeting only subset of MNs for precise vibrissa movement.

Among all the premotor brainstem nuclei, gigantocellular reticular nucleus (Gi) (n = 258 and 27), intermediate reticular nucleus (IRt) (n=97 and 19), and the dorsal medullary reticular formation (MdD) (n=87 and n=34) in ipsilateral brainstem had the highest number of infected neurons. In total, their distribution is half (49% and 57%) of all the infected neurons in both brains. In contrast, the number of infected neurons in these three regions in the contralateral hemisphere was minimal (10% and 7.24%) of all infected neurons. These findings show the strong ipsilateral dominance of motor projection, further reinforcing the importance of reticular nuclei in unilateral vibrissa control.

There were infected neurons also in the trigeminal nuclei (SP5C/I/O, Pr5), where labeling was exclusively ipsilateral (n=81 and n=5) with no infected neurons found in the contralateral hemisphere. Since, the trigeminal nuclei are primarily associated with sensory processing, sensorimotor integration at the second-order is strictly unilateral. This also suggest that sensory-related structures also contribute to motor control (Matyas et al., 2010). The lack of contralateral labeling also suggest that sensory feedback required for vibrissa motor control does not cross hemisphere at this early synaptic order.

3.1.2 Third-order brains

In six brains, rabies-infected neurons were observed cerebral cortex. In all these brains, labeling was confined to layer 5 (L5) of cortex. These six brains included three injections into the vibrissa muscle and three injections into the EDC muscle of the forelimb.

In three brains with rabies injection to vibrissa muscle, rabies-infected motoneurons (MNs) in the FN were restricted to the ventrolateral region and were found exclusively in the ipsilateral hemisphere (Figure 13). The absence of infected MNs in contralateral FN suggests

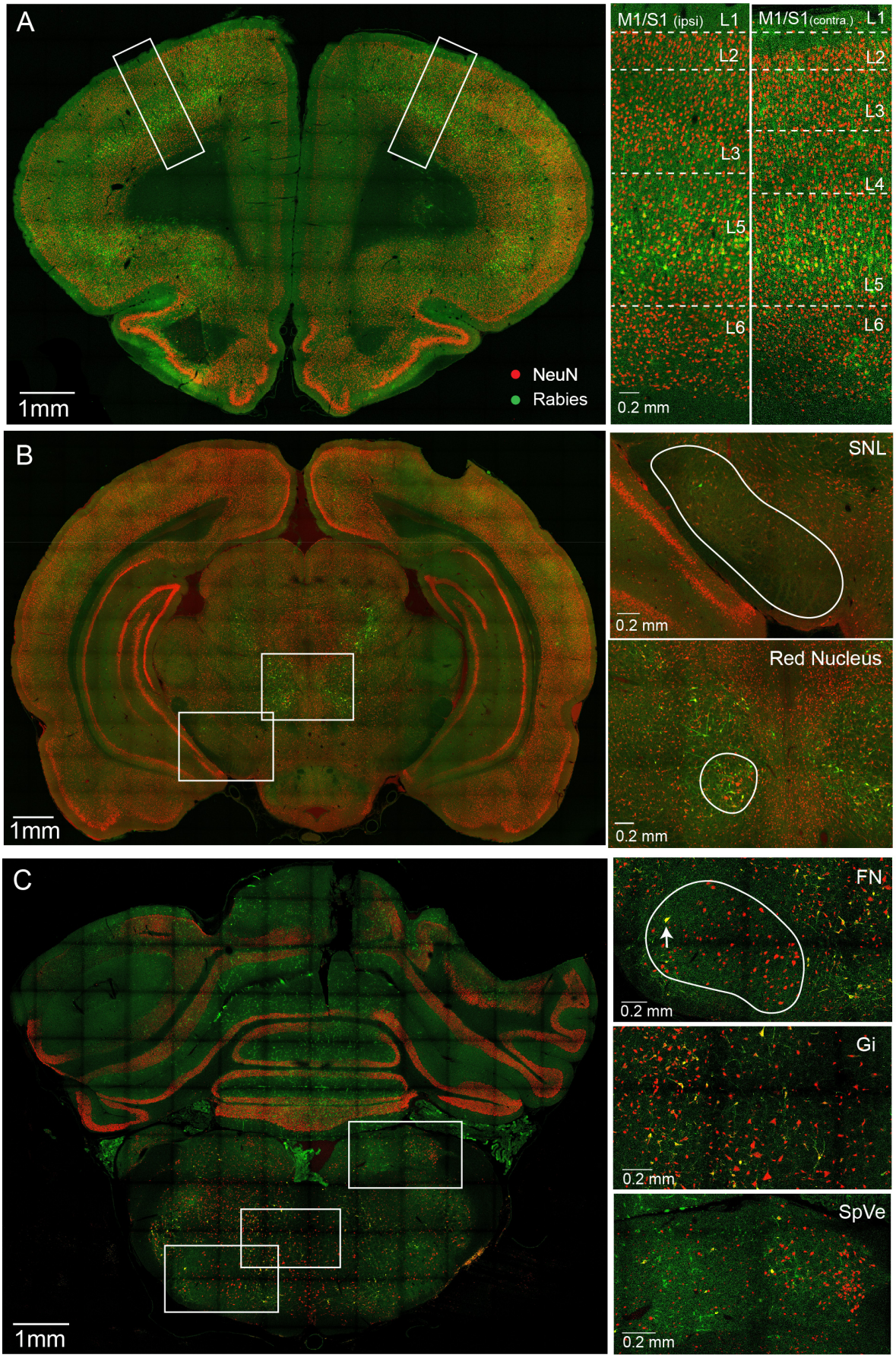

Figure 13: Example confocal images of rabies virus-infected neurons in a third-order brain. (A) Cerebral Cortex (B) Midbrain (C) Cerebellum and Brainstem. Zoomed images of the boxes in each panel is shown on the right. SNL, Substantia Nigra; Spinal Vestibular nuclei

that motoneurons of a single vibrissa muscle do not receive disynaptic projections from contralateral facial nucleus. The total number of infected MNs remained relatively low (n= 9, 21, 28) with some variability across the brains. Despite the variation, the overall spatial distribution of infected neurons remained consistent further reinforcing the topographic organization of MNs within the FN. Further analysis of these findings is presented in section 4.1.1.

Rabies-infected neurons were observed in previously identified premotor brainstem nuclei in all three brains following the rabies injection to vibrissa muscle (Table 7). However, there was a significant increase in the number of infected neurons in these nuclei (n=9366, 8492, 13699). Similar to second order brain, gigantocellular reticular nucleus (n= 1051, 1179, 1596) , intermediate reticular nucleus (n = 1220, 882, 302) and dorsal medullary reticular formation (n = 927, 294, 1102) had the highest number of infected neurons in the ipsilateral hemisphere. There was also increase in number of new brainstem nuclei infected showing a more extensive network of motor control in brainstem. This findings highlight the projection of neurons within the brainstem nuclei as well as between brainstem nuclei. Further analysis of these findings is reported in section 4.1.2.

In addition to the brainstem and cortex, cerebellum and midbrain also has disynaptic projection to the MNs(Figure 13B and C). There are infected neurons in midbrain structures like superior colliculus and red nucleus. The analysis of infected neurons was limited to the cerebral cortex in brains where rabies virus was injected into the EDC muscle.

In all third order brains, infected neurons were detected in primary motor cortex (M1), and also in additional cortical regions, including primary somatosensory cortex (S1), secondary motor cortex (M2), secondary somatosensory cortex (S2) and insular cortex (Figure 13A). Labeling was present in both hemispheres, suggesting a bilateral cortical contribution to motor control. A similar distribution pattern was found in brains where the rabies virus was injected into the EDC muscle, indicating that forelimb motor circuits, like those of the vibrissa system, extend beyond M1 to engage multiple cortical areas. Detail analysis of

the infected L5PNs is done in following section 4.1 of next chapter.

3.1.3 Higher-order brains

In the higher-order brains (n=10), rabies-infected neurons were observed beyond layer 5 (L5) of the cortex, with spread to upper and deeper cortical layers, indicating further progression of retrograde transsynaptic transport. The increase of infected neurons was only quantified for facial nucleus. Expansion of infected neurons across all higher-order brains was not systemically quantified in this thesis. Example images from all the higher-order brains are shown in Figure 14, 26- 34.

In the facial nucleus, for the first time, labeling was observed bilaterally. Eight brains had bilateral FN labeling, where as two brains showed labeling in the ipsilateral FN. This indicates that these higher order brains can be further classified into different orders. The number of total infected MNs range from 13 to 203 (Table 11). Even though the maximum observed infected neurons (n=203) represents a significant increase compared to second- and third-order brains, it is still a fraction of total MNs population in FN (Figure 14C). This suggests that even at higher-synaptic order, MNs do not project to each other or to additional brain regions. Detail analysis of distribution of MNs in facial nucleus of higher order brains are examined in section 4.2.1 in next chapter.

In the brainstem, more nuclei were infected with virus (Figure 14C). The rabies infection extend to every brainstem nuclei. This reveals that all the brainstem regions are included in motor control at this synaptic order.

In cortex, infected neurons was no longer confined to L5PNs but extended into upper and deeper cortical layers. Interestingly, this spread was primarily observed in regions that had been labeled in third-order brain, such as M1, S1, M2, and insular cortex (Figure 14A). This increase suggests a structured, hierarchical integration of cortical regions into the motor control network. The spread of infected neurons appeared to follow a frontal-to-rostral progression, This pattern highlights the transition from motor to brain regions dedicated to

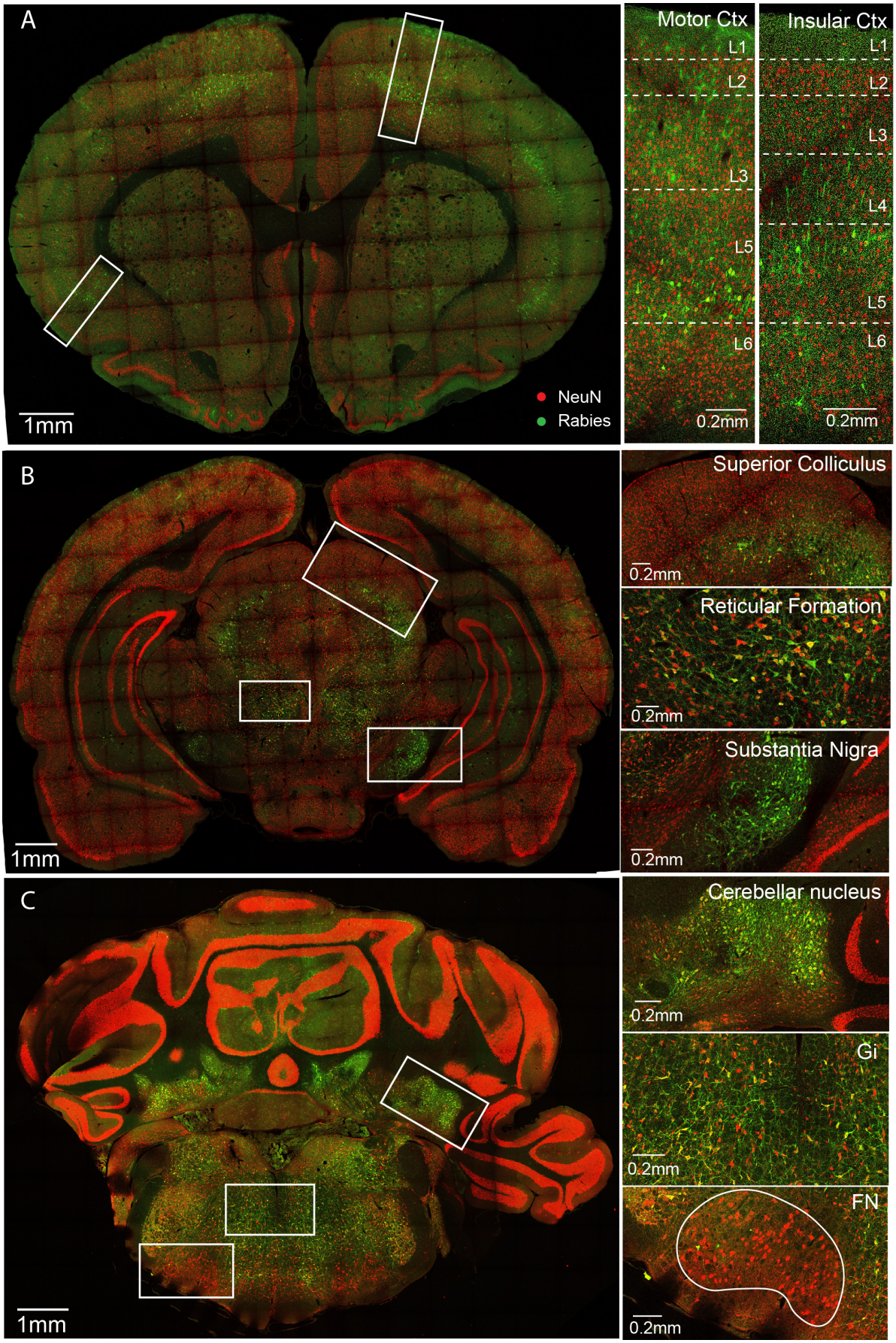

Figure 14: Example confocal images of rabies virus-infected neurons in a third-order brain (HB1). (A) Cerebral Cortex (B) Midbrain (C) Cerebellum and Brainstem. Zoomed images of the boxes in each panel is shown on the right.

other modalities like vision.

Several additional brain regions exhibited rabies infected neurons. Notably, labeling was observed in the hippocampus, visual cortex, and parietal cortex.The cerebellum also showed significant labeling, particularly in deeper cerebellar nuclei. The labeling further progressed into Purkinje cells. This further highlights the widespread connectivity of higher-order motor circuits. Furthermore, hemispheric differences were evident in several brain regions of midbrain (Substantia nigra - Figure 14B). These findings collectively indicate that at higher-order brains, motor control networks extend into diverse brain areas, integrating sensory, cognitive, and motor planning functions to refine movement execution.

3.2 Machine learning

Five Faster R-CNN models were developed from different training datasets (Table 1). Rabies virus-infected neurons which were marked manually from three different higher-order brains were used as training datasets. The training datasets from all three brains consisted of rabies virus infected neurons from cortex, midbrain, cerebellum and brainstem. All the model were tested on the ground truth. Model 1, trained on all neurons from a single higher-order brain (soma only), exhibited highest recall (0.977) indicating strong ability to identify almost all ground truth. However, it has lower precision (0.690), showing higher rate of false positives. Conversely, Model 2 and 3, trained on datasets with and without artifacts respectively from a different higher-order brain demonstrated higher precision (0.821 and 0.848) but lower recall (0.639 and 0.604), indicating that it missed significant portion of actual neurons while maintaining accuracy in positive detections. Model 4 and 5 was trained on larger datasets with neurons from two higher-order brains, achieved a balance performance with F1 scores of 0.732 and 0.735. The results highlight a trade-off between precision and recall. Model 1 prioritizes sensitivity and Model 2 and 3 prioritize specificity. Model 4 and 5 demonstrate a robust and balanced performance, mostly due to larger and more diverse training datasets.

Table 1: Comparison of Faster R-CNN model performance.

Model ID	Training dataset	Number of training boxes	Recall	Precision	F1-score
1	all neurons from a higher-order brain (soma only)	84905	0.690	0.997	0.809
2	all neurons from a different higher-order brain (artifact + soma)	87995	0.821	0.639	0.710
3	same training data as Model 2 (soma only)	87609	0.848	0.604	0.699
4	neurons from two higher-order brains (soma only)	153624	0.805	0.686	0.732
5	retrained Model 3 + neurons from another higher-order brain (soma only)	153624	0.815	0.684	0.735

Table 2: Paired t-test of the performance metrics between model pairs.

	Recall		Precision		F1-score	
Model pairs	**t Stat**	**p-value**	**t Stat**	**p-value**	**t Stat**	**p-value**
Model 1 vs Model 2	-4.17	0.001	10.17	0.000	2.42	0.0357
Model 2 vs Model 3	-3.48	0.005	7.72	0.000	2.50	0.0311
Model 4 vs Model 5	-3.07	0.01	0.61	0.55	-1.16	0.2701

Paired t-tests were conducted to compare the performance metrics (recall, precision, and F1-score) between specific model pairs (Table 2).

- **Model 1 vs Model 2**: Model 2 had significant decrease in precision (t-statistics=

10.17; p-value= 0.000) and showed significant increase in Recall (t-statistics= -4.17; p-value= 0.001). Model 2 showed significant less accuracy than Model 1 (t-statistics= 2.42; p-value= 0.03).

- **Model 2 vs Model 3**: The removal of artifact in training datasets in Model 3 improved the Recall compared to Model 2(t-statistics=-3.48; p-value= 0.005). However, it did not improve the precision (t-statistics= 7.72; p-value=0.000) and F1-score (t-statistics= 2.50; p-value= 0.0311) Comparison between Model 2 and Model 3 showed a statistically significant difference (t= -3.48, p-value= 0.005), with Model 3 showing higher recall.

- **Model 4 vs Model 5**: Model 5 showed significant increase in Recall (t= -3.07, p-value = 0.01). However, there was no significant different in precision and F1-score between Model 4 and Model 5.

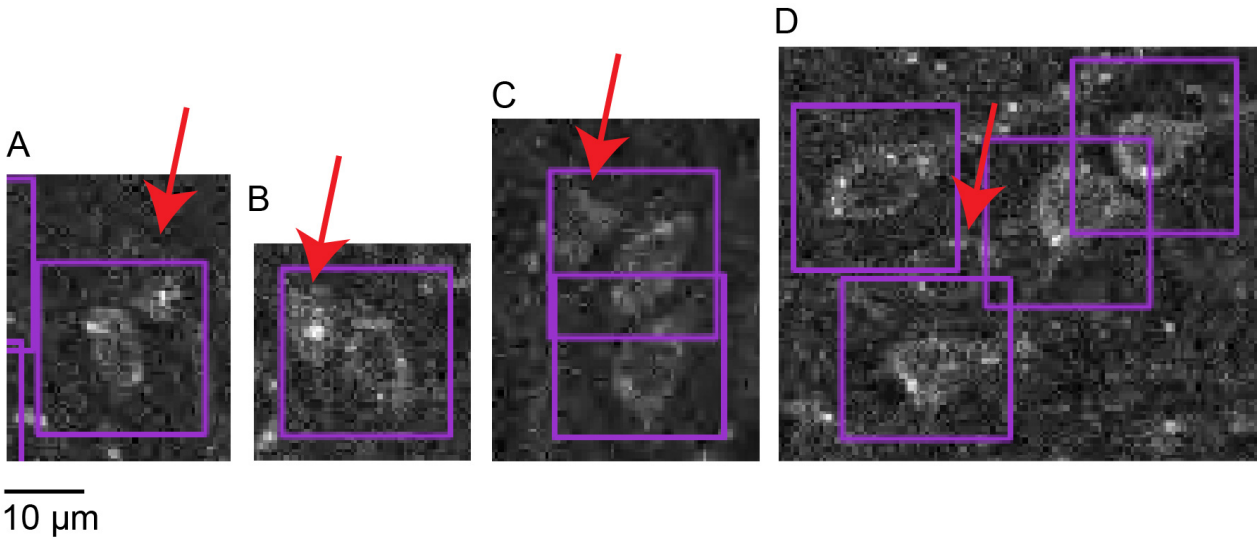

Figure 15: Example images of missed neuron detections by the Faster-RCNN model. Four example images from cortex where the purple bounding box represent the rabies virus-infected neuron detected by the Faster-RCNN model and the red arrow shows the neurons that model missed.

The faster R-CNN model showed limitations in accurately detecting neurons within high density regions of the confocal images such as in the cortex.Particularly overlapping neurons (Figure 15B) and neurons with close boundaries resulted in missed detections (Figure

15A). In two example images (Figure 15C and D), neuron that is close to two or more neurons was missed. In both examples, the bounding box of one or more neurons overlap the neuron that was missed.

4 Biological results

In the first part of this chapter, I focus primarily on the third-order brains (n=6), analyzing the distribution of layer 5 pyramidal neurons (L5PNs) infected with the rabies virus. And in the final part of this chapter, I will compare the distribution of rabies-infected neurons in facial nucleus across all the higher-order brains.

4.1 Third-order brains

4.1.1 Quantitative organization of motoneurons in the facial nucleus

The rabies virus-infected motoneurons (MNs) were restricted to the C-row representation of intrinsic vibrissa muscles within the ventrolateral facial nucleus ipsilateral to the injected muscle (Figure 16). The number of first-order MNs in the facial nucleus remained small and relatively stable across second and third-order transsynaptic transport (median: 9; 25th/75th percentile: 6/21; n=5). Compared to our previous study using Cholera Toxin subunit B (CTB) to determine the location and size of the MN pool (Guest et al., 2018), approximately 10-30% of MNs controlling the protraction of the C3 vibrissa were infected with the rabies virus. Importantly, rabies virus-infected MNs are localized within the C3 MN pool. These observations show that the rabies virus did not spread beyond the localized injected site within the muscle and confirm that MNs of the intrinsic muscles are not connected.

4.1.2 Quantitative organization of premotor neurons in the brainstem

In third-order brains, rabies virus injection into the vibrissa intrinsic muscle show extensive infection across all previously identified premotor brainstem nuclei associated with vibrissa muscle (Takatoh et al., 2013) and in additional brainstem regions (Figure 17A). The total number of infected neurons in brainstem nuclei where we see labeling in second-order brains was 31557 (Mean ± SD: 10519 ± 2788). It is important to note that infected

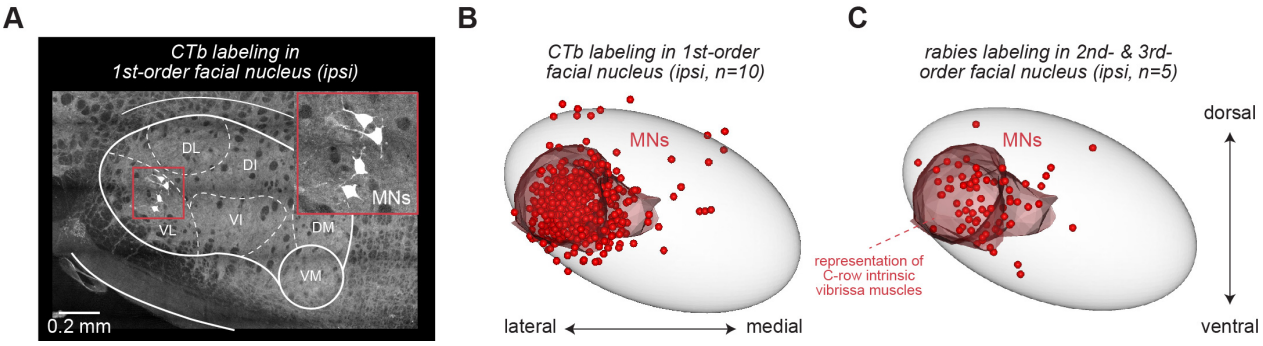

Figure 16: Comparison of motoneurons distribution in the ventrolateral facial nucleus. (A) Example image of the CTB labeled motoneurons in first-order ipsilateral facial nucleus. (B) Spatial distribution of motoneurons of the first-order motoneurons in the facial nucleus after registration in standard facial nucleus reference frame. Data from Guest et al., 2018. (C) Spatial distribution of motoneurons of the second-order (n=2) and third-order (n=3) motor neurons in the facial nucleus after registration in standard facial nucleus reference frame. CTB, Cholera toxin subunit B; VL, ventrolateral; DL, Dorsolateral; DI, Dorsal intermediate; DM, Dorsomedial; VM, Ventromedial.

brainstem nuclei in third-order brains contain both second-order and third-order infected neurons. The substantial increase in infected neurons at this synaptic order highlights the extensive projection from brainstem to the premotor nuclei.

Compared to second-order brains, third-order brains showed a notable reduction in hemispheric bias with the ipsilateral-to-contralateral ratio (third order:1.64 vs second order: 4.6). This reduction was evident in Gi, where labeling was more evenly distributed between hemispheres (ipsilateral: 3826; contralateral: 3295). This suggests that motor control from this nucleus, at disynaptic connections to MNs, is bilaterally integrated. However, trigeminal nuclei still maintained ipsilateral dominance (ipsilateral: 5106; contralateral: 1076), indicating lateral organization of sensory brainstem nuclei even at third-order level.

4.1.3 Third-order rabies virus spread within the cerebral cortex

In third-order brains, the rabies virus infections was observed in L5PNs in the cerebral cortex , including the neurons in brainstem, midbrain and cerebellum (Figure 18). A major finding in the infected cortical neurons is that these vL5PNs are distributed across multiple cortical areas in both hemispheres including the primary and secondary motor cortices (M2

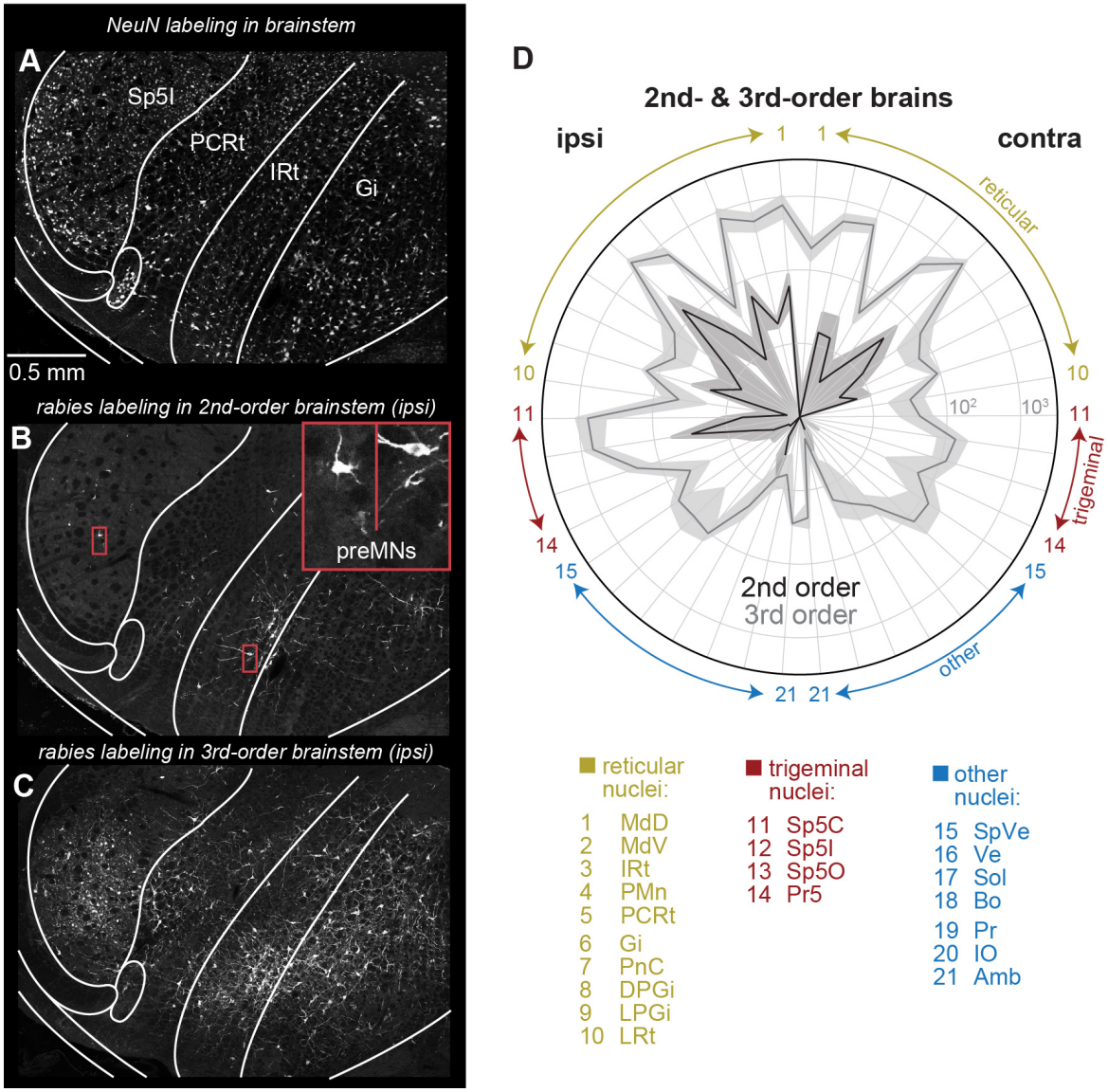

Figure 17: Comparison of preMNs in the brainstem nuclei. (A) Example confocal image of NeuN labeling in brainstem. (B, C) Example confocal images of rabies labeling in 2nd-order brainstem and 3rd-order brainstem. (D)Radar plots show rabies labeled preMNs per nuclei in 2nd-order brainstem (n=2, mean ± STD, dark shading), and how the numbers of rabies labeled neurons increase in these 21 'premotor' nuclei in 3rd-order brainstem (n=3, light shading). See Table 7 for a list of abbreviations.

and M2), the primary and secondary somatosensory cortices (S1 and S2), and the anterior insular cortex (AI). Nearly two-thirds of these neurons are located outside the contralateral M1, with approximately 30% located in the ipsilateral hemisphere, predominantly in motor areas (Figure 18C). In total, more than 60% of the rabies labeled cortical neurons are located in cortical motor areas. About 40% of the infected cortical neurons are located in the somatosensory areas of the cerebral cortex. More than two-thirds of these are located in the contralateral somatosensory cortex. Less than 5% of the infected cortical neurons are located in the AI of both hemisphere with no significant difference between contralateral and ipsilateral AI. These observations emphasize three points. First, rabies-infected L5PNs establish disynaptic connection to the MNs. Second, cortical motor control extends beyond primary motor cortex, involving multiple cortical regions. Third, the findings provide anatomical evidence supporting the bilateral nature of cortical control over vibrissa protraction, as observed in functional studies of cortical motor stimulation (Matyas et al., 2010).

4.1.4 Mapping of vL5PNs in primary motor cortex (M1)

To quantitatively compare cortical labeling between hemispheres, a flat map of the cortex was reconstructed, with each voxel representing L5PN density within a 200μm × 200μm area (Figure 19). The rabies virus-infected vL5PNs located in M1 are distributed across the entire body map in each hemisphere (Figure 19A and 19C). Notably, small numbers of vL5PNs are located even in the hindlimb representations of contralateral and ipsilateral M1. Despite this widespread distribution, the highest density of vL5PNs is concentrated in the contralateral M1 region ($vM1_{contra}$) commonly associated with vibrissa protraction (Petersen, 2014). A second distinct peak density of vL5PNs is located in ipsilateral M1 ($vM1_{ipsi}$) lateral to the $vM1_{contra}$ (Figure 19C). And a third dense region is located in contralateral M2 (vM2). These results show that the vibrissa control involves a widespread region of M1 and M2, with distinct hotspots in contralateral and ipsilateral M1 for evoking vibrissal protraction.

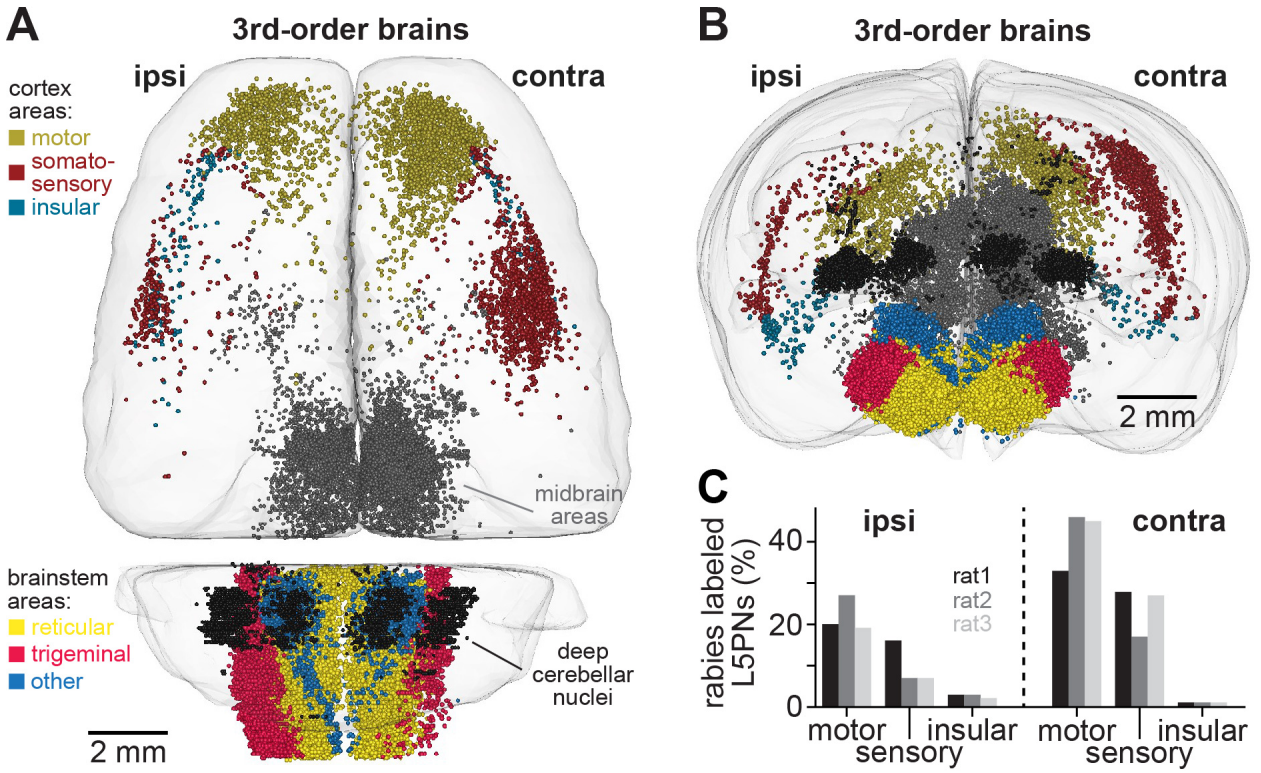

Figure 18: Spatial distribution of rabies virus-infected neurons in third-order spread. (A) Top view onto average brain shows soma locations of all rabies labeled neurons from three brains where rabies virus did not spread beyond L5. (B) Coronal view of panel A (C) Bar graph comparing rabies-labeled L5PNs in ipsilateral vs. contralateral motor, somatosensory, and insular cortex across third-order brains(normalized to the total number of L5PNs per rat).

4.1.5 Distribution of vL5PNs in somatosensory cortex

Another major area of rabies-infected L5PNs distribution (~35%) lies in the somatosensory cortex. Compared to M1, where infected L5PNs were spread across both hemispheres of M1, majority of the infected L5PNs were concentrated in primary somatosensory cortex (S1) (Figure 19A-B). The vibrissa-related region of S1, barrel field (vS1), is structurally defined in layer 4 of the S1. When overlaid with the reconstructed barrel field, the distribution of infected L5PNs revealed that most were located within the contralateral vS1.

Additionally, infected L5PNs extended into adjacent areas associated with facial muscle representation, as well as in the secondary somatosensory cortex (S2). Interestingly, while majority of the L5PNs in vS1 were contralateral, the L5PNs were evenly distributed in S2

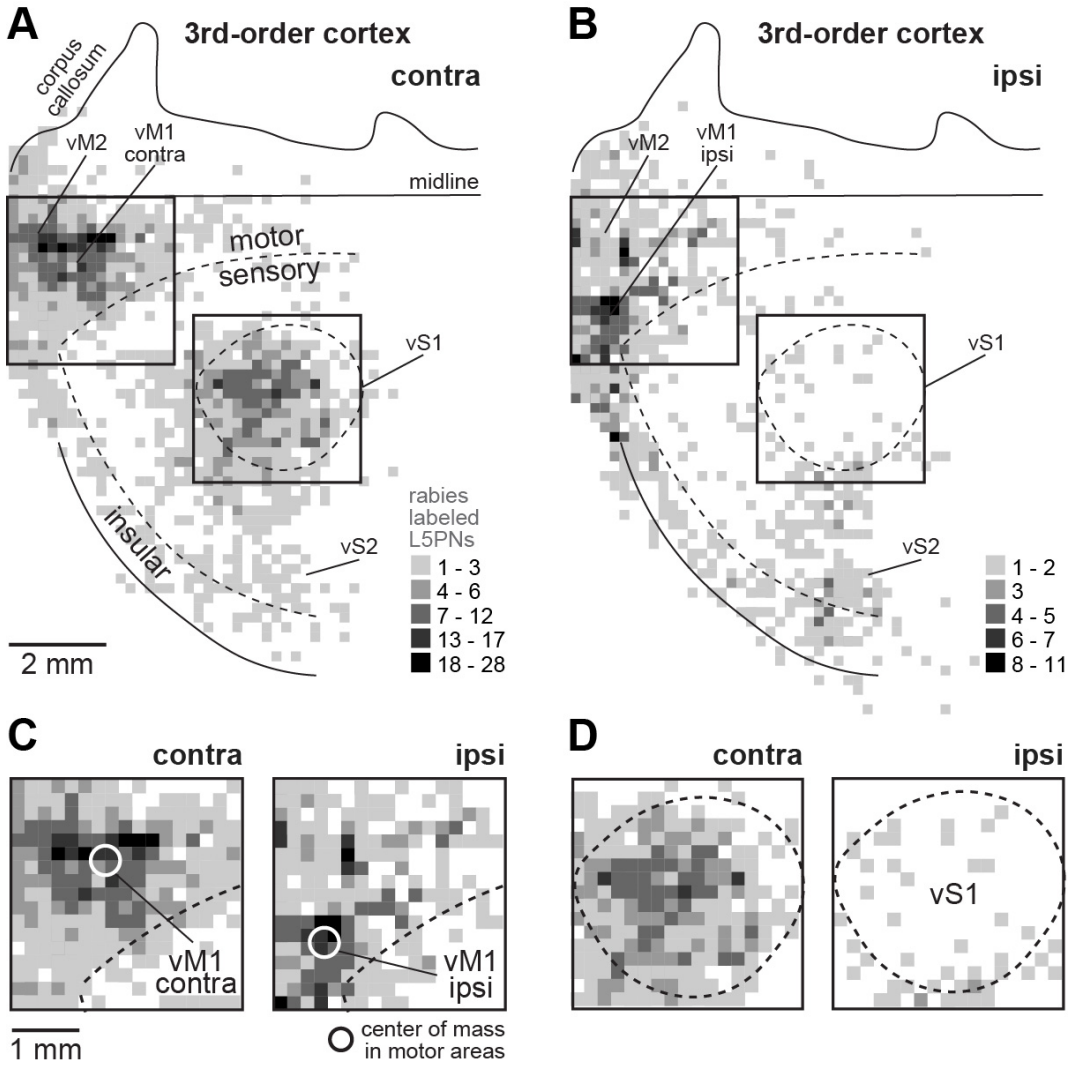

Figure 19: Distribution of rabies-infected cortical neurons (flat map view). (A) Distribution of L5PNs infected with rabies virus in contralateral hemisphere. Each voxel is L5PN density per 200µm x 200µm. Dashed lines represent cytoarchitectonic borders between motor, somatosensory and insular cortex, and vibrissae-related primary somatosensory cortex (vS1). (B) same as in panel A for ipsilateral cortex (C) Enlarged boxes around motor areas in panel A and panel B. (D) same as in panel C for primary somatosensory cortex. vM1, vibrissa primary motor cortex; vM2, vibrissa secondary motor cortex; vS2, vibrissae-related secondary somatosensory cortex

between two hemispheres. This suggests that while vS1 provides a strong unilateral descending motor output for vibrissal control, S2 play a more bilateral role. Taken together, this findings support the idea that somatosensory cortex serves as a critical area for descending motor commands.

To investigate the relationship between sensory input and motor output of an individual

muscle in vS1, the distribution of infected L5PNs was overlaid with the barrel columns (Figure 20B). Barrel columns were reconstructed from tangential sections of one of the third-order brains. A tangential section, with a cutting plane perpendicular to vS1, allowed clear visualization of the barrel columns (Figure 20A). This analysis revealed that among all the barrel columns, most of the infected vL5PNs were located beneath the C3 barrel column, which corresponds to the injection site of the vibrissa muscle (Figure 20). Additionally, vL5PNs were widely distributed across multiple surrounding barrel columns, including the B-, D-, and E-rows (Figure 20C). A key difference between sensory and motor representation in vS1 is that sensory input follows a one-to-one mapping, where each vibrissa corresponds directly to a specific barrel column. In contrast, motor output exhibits a broader ”barrel field-to-one” mapping, where both the primary and surrounding barrel columns contribute to the control of a single vibrissa muscle.

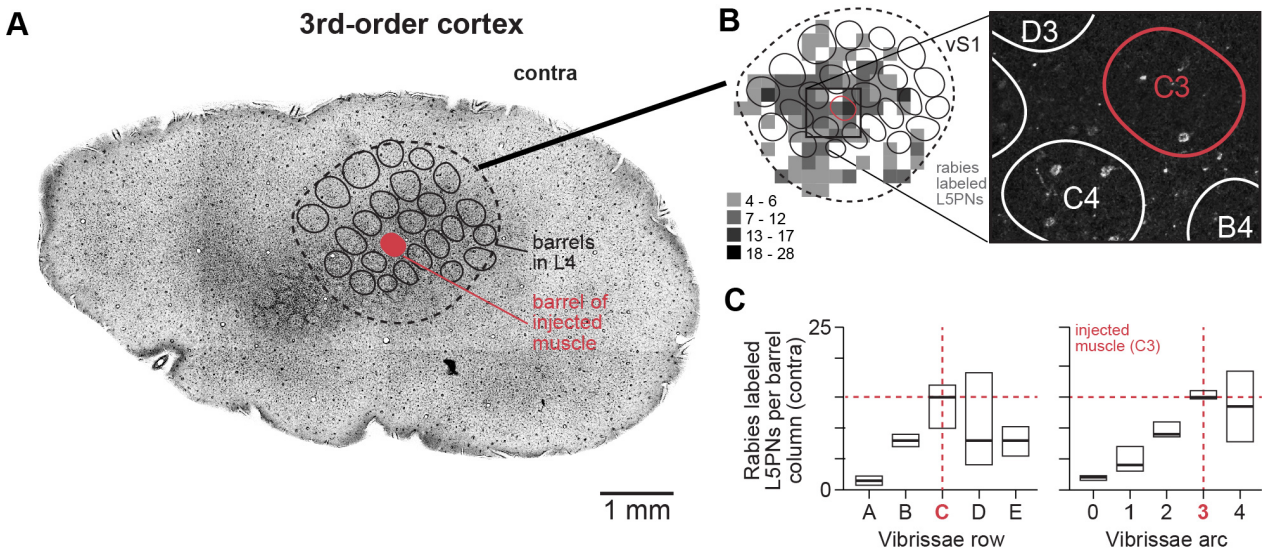

Figure 20: Spatial distribution of the rabies-infected neurons in the barrel cortex. (A) Brightfield image of 50 µm thick section of contralateral hemisphere cut tangentially to vS1 from a third-order brain. The outlines and labeled structures represent the L4 barrel field. (B) Left: Enlarged view of the barrel field from panel A, showing density distribution (without lowest density bin). Right: Confocal image for a deeper L5 section showing rabies virus-infected L5PNs relative to barrel outlines (white). (C) Quantification of L5PNs per cortical barrel column (n=21, median ± 25th/75th percentile) for the brain in panel E. Barrel columns were grouped by vibrissae row (left) and arc (right).

4.1.6 Vibrissa vs. forelimb cortical motor control

To determine whether cortical motor control of the vibrissa corresponds to that of other muscles in rats, rabies virus was injected into a forelimb muscle (Figure 21A; n=3). The extensor digitorum communis (EDC) muscle functions to extend and spread the digits as part of grasping movements. In all cases, rabies-infected neurons were confined to layer 5 of the cerebral cortex (Figure 21B). These layer 5 pyramidal neurons (fL5PNs) were found in both hemispheres, with the majority (93%) located in the contralateral cerebral cortex . In contralateral hemisphere, the fL5PNs were primarily distributed in the primary motor cortex (fM1) and primary somatosensory cortex (fS1), with smaller populations in the secondary motor cortex (fM2) and secondary somatosensory cortex (fS2)(Figure 21C). In the ipsilateral hemisphere, a small number of fL5PNs were sparsely distributed across fM1, fS1, fM2, and fS2 (Figure 21D).

Several key differences characterize the cortical origins of descending output to the EDC compared to the vibrissa muscle. First, fL5PNs are predominantly located in the contralateral hemisphere of M1, whereas vL5PNs are more bilaterally distributed throughout M1 with the densest region in vM1. Second, a greater proportion of fL5PNs originate from sensory areas, particularly fS1, whereas vL5PNs primarily arise from motor regions. Specifically, nearly 50% of fL5PNs are found in fS1, while only about 20% of vL5PNs originate from vS1. Third, fM2 contributes only a minor proportion of fL5PNs, with fewer than 3% located in the contralateral hemisphere. Finally, unlike vibrissa-related L5PNs, fL5PNs do not originate from the insular cortex in both hemisphere. These differences suggest forelimb control is unilateral from motor and somatosensory area, while vibrissa control engages a broader, more bilateral motor area and unilateral somatosensory area.

To further examine the intersection of forelimb and vibrissa L5PN distributions, contralateral maps of L5PNs from EDC and vibrissa injections were overlapped (Figure 22A). In S1, fL5PNs and vL5PNs exhibited only minor overlap, primarily at the border between vS1 and fS1 (16%). In contrast, extensive overlap was observed in the motor areas . In M1, 84%

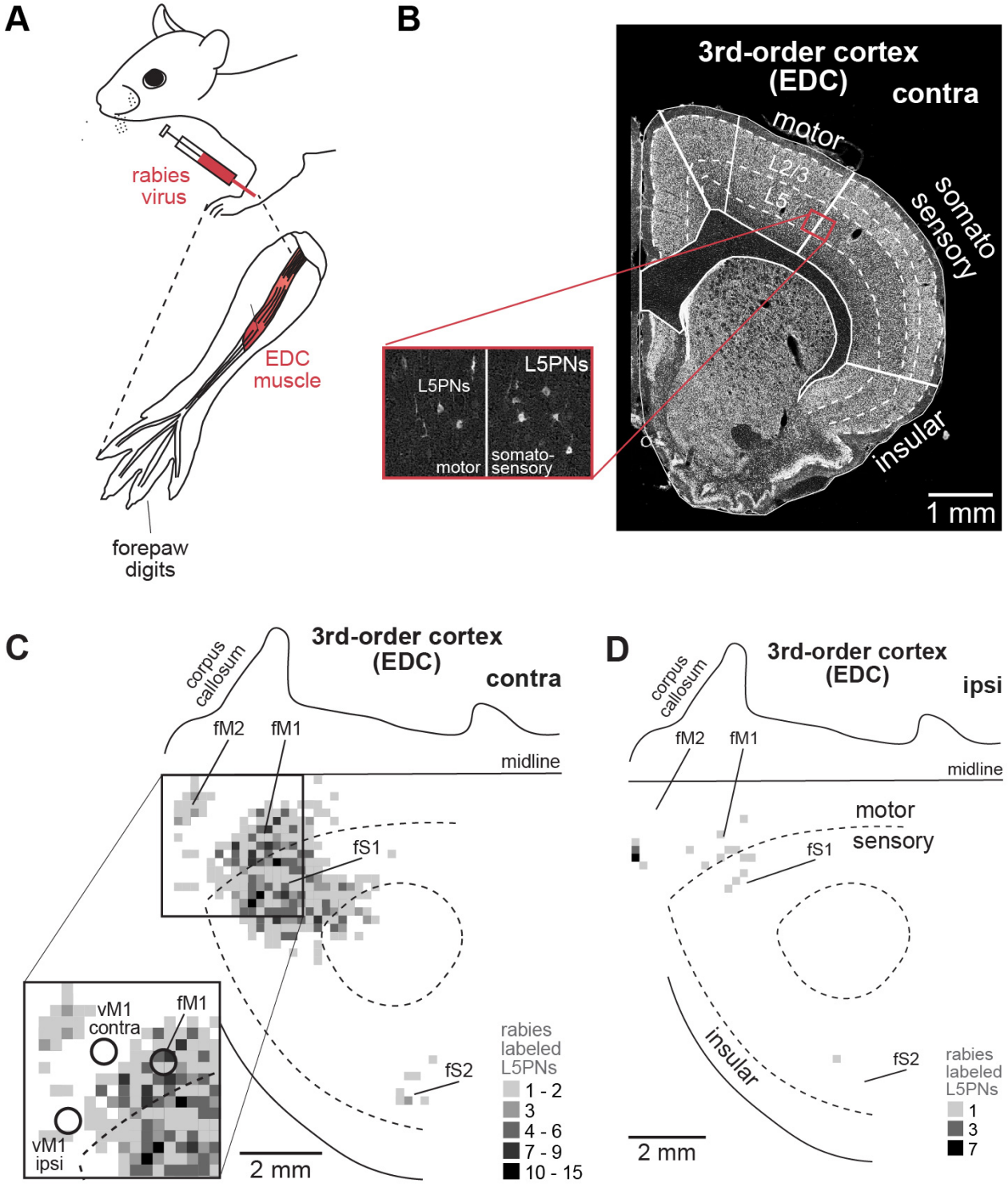

Figure 21: Cortical output system that controls a single forelimb muscle. (A) Rabies virus was injected to a single the extrinsic digitorium communis (EDC) muscle in forelimb that control digits. (B) Example brightfield image of coronal section contralateral to the injected EDC muscle. (C) Distribution of L5PNs infected with rabies virus (3rd-order, n=3) of the contralateral hemisphere. (D) Same as panel C for the ipsilateral hemisphere. fM1, forelimb primary motor cortex; fM2, forelimb secondary motor cortex; fS1, forelimb primary somatosensory cortex; fS2, forelimb secondary somatosensory cortex

of fL5PNs overlapped with vL5PNs, while 38% of vL5PNs overlapped with fL5PNs (Figure 22B). The overlap map revealed three distinct zones within M1: moving rostral from the M1-S1 border, there is first a small EDC-only region, followed by a larger region of EDC and vibrissae overlap, and finally, an even larger vibrissa-only region encompassing $vM1_{contra}$ and $vM1_{ipsi}$. In M2, two zones were identified: one containing both EDC and vibrissa representations, and a second, larger vibrissa-only region. Notably, no separate representation of EDC was observed in M2, which may be due to the relatively small number of fL5PNs in this region. And the distribution of the vL5PNs in the secondary somatosensory is al .These findings show that there is extensive overlap in motor areas between two muscle. However, both muscles have distinct representations in somatosensory areas. This suggests fundamental differences in how the sensory and motor cortices represent different body parts in the rat cerebral cortex.

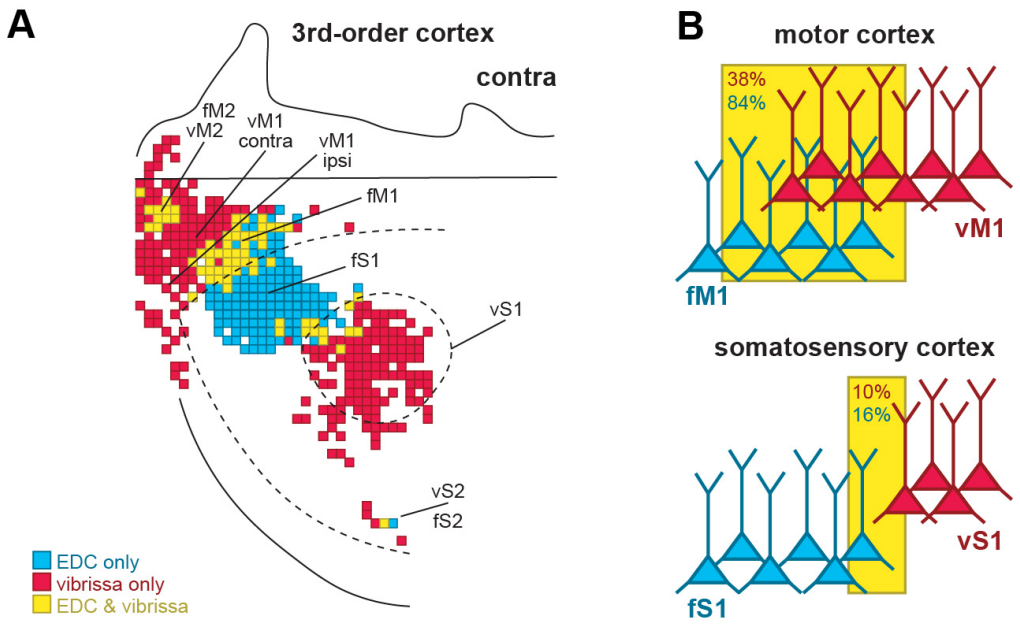

Figure 22: Comparison of contralateral hemisphere labeling between vibrissa and extensor digitorum communis (EDC) muscle. (A) Overlap of the L5PN density maps of the contralateral hemisphere from Fig 19A and Fig 21C. Blue represents EDC control regions (fM1, fS1), red represents vibrissa control regions (vM1, vS1), and yellow represents both EDC and vibrissa. (B) Graphical representation of overlap of vL5PNs and fL5PNs in motor cortex and somatosensory cortex.

4.2 Higher-order brains

In this study, ten rabies virus-infected brains showed cortical neurons infection beyond layer 5 showing further progression of the retrograde transsynaptic transport. In these brains, we observed both infection of new brain regions and a significant increase in number of infected neurons within previously identified areas, such as brainstem, midbrain, cerebellum and cortex (Figure 26-34). To illustrate this, I will focus on the facial nucleus, a first-order brain region.

4.2.1 Facial nucleus

In second and third-order brains, approximately 10-30% of motoneurons(MNs) innervating a single vibrissa muscle were labeled on the ipsilateral side relative to the injection (Figure 16). As transsynaptic order increased, the number of motoneurons infected by rabies virus also increased (Table 11). In two brains, rabies virus labeling was still exclusively observed in the ipsilateral FN(number of MNs = 13 and 19). However, in other eight brains, there were rabies-infected MNs in both ipsilateral and contralateral facial nucleus (ipsilateral: median = 75; 25th/75th percentile= 54/90; n=8 vs contralateral: median=65;25th/75th percentile= 35/78; n=8). These results show that even within higher-order brains, there exists variability in the extent of transsynaptic spread. Some brains exhibit labeling exclusively in the ipsilateral FN, while others show labeling in both ipsilateral and contralateral GN, with varying number of rabies-infected MNs.

Rabies virus-infected MNs in higher order show two categories of soma size (Figure 23A). In second and third-order brains, most of the MN infected with rabies virus have large dendritic arbor and large volume relative to other neurons in the brainstem (Guest et al., 2018). For example, a MN in Figure 23A have 144 dendritic arbors and a total soma volume of 14907 μm^3. Comparative there are MNs with smaller size. For example, two MNs in higher-order brain (Figure 23B and C) have only 28 and 46 dendritic arbors respectively. The soma volumes are also small(864 μm^3 and 1491 μm^3). When we compare

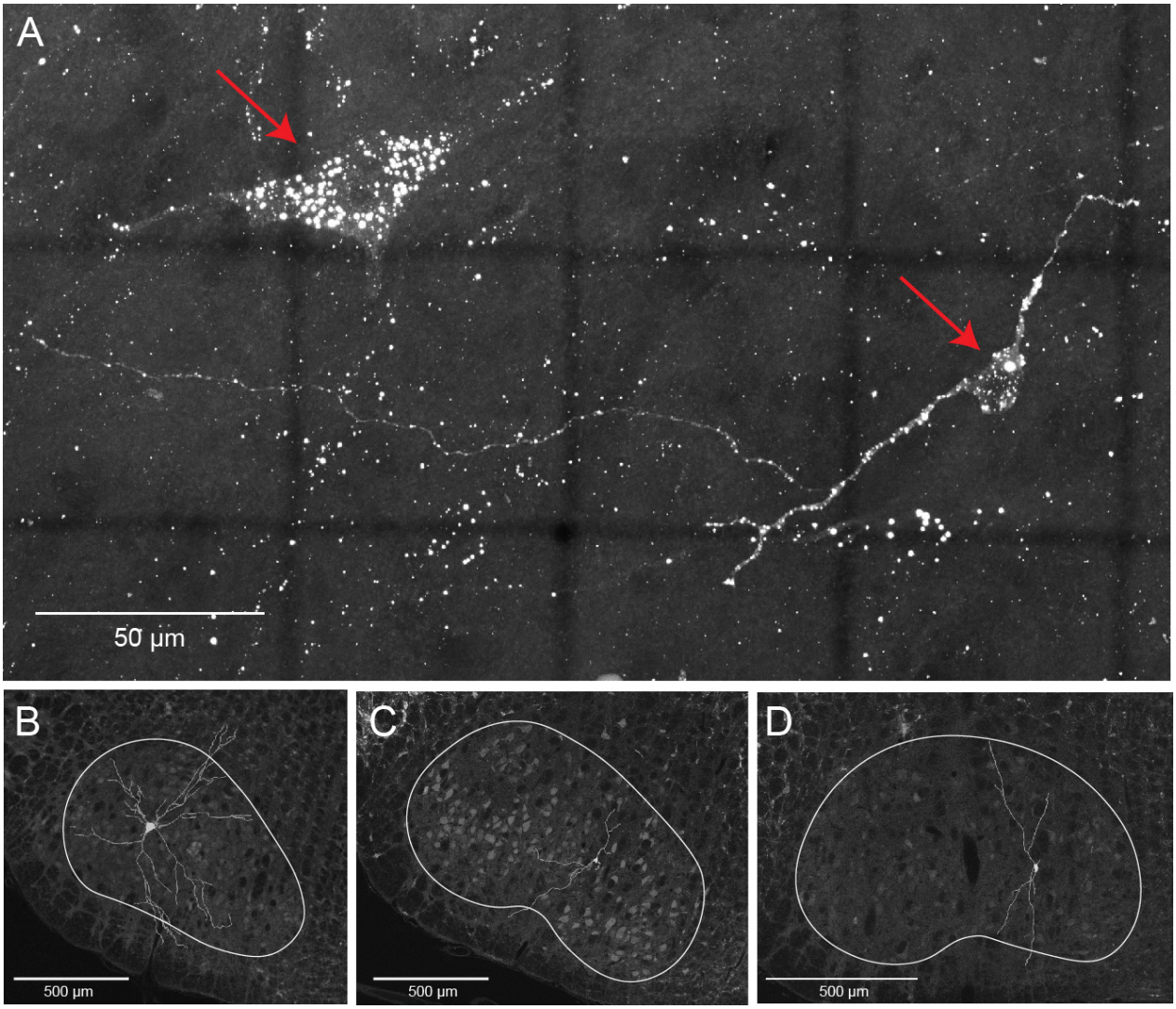

Figure 23: Morphology of two type of motoneurons in the facial nucleus. (A) High resolution image with two motoneurons (shown with red arrow) in a facial nucleus of higher-order brain (zoomed image of Panel C). (B) 3D reconstruction of a vMN from second-order brain. (C) and (D) 3D reconstruction of vMNs from higher-order brain.

the volume, the difference is tenfold. Similarly, when we compare the dendritic arbors, there is difference of fourfold. We also observe that large MNs exhibit outward-extending dendritic arborization from the FN whereas smaller MNs show only a couple of dendritic arbors outside of FN.

Further analysis of the cross-sectional areas of the rabies-infected MNs at different synaptic orders (second: n=1; third: n=1; higher order: n=4) showed a bimodal distribution of MN size (Figure 24. The mean cross-sectional area of all MNs from every fifth section in the

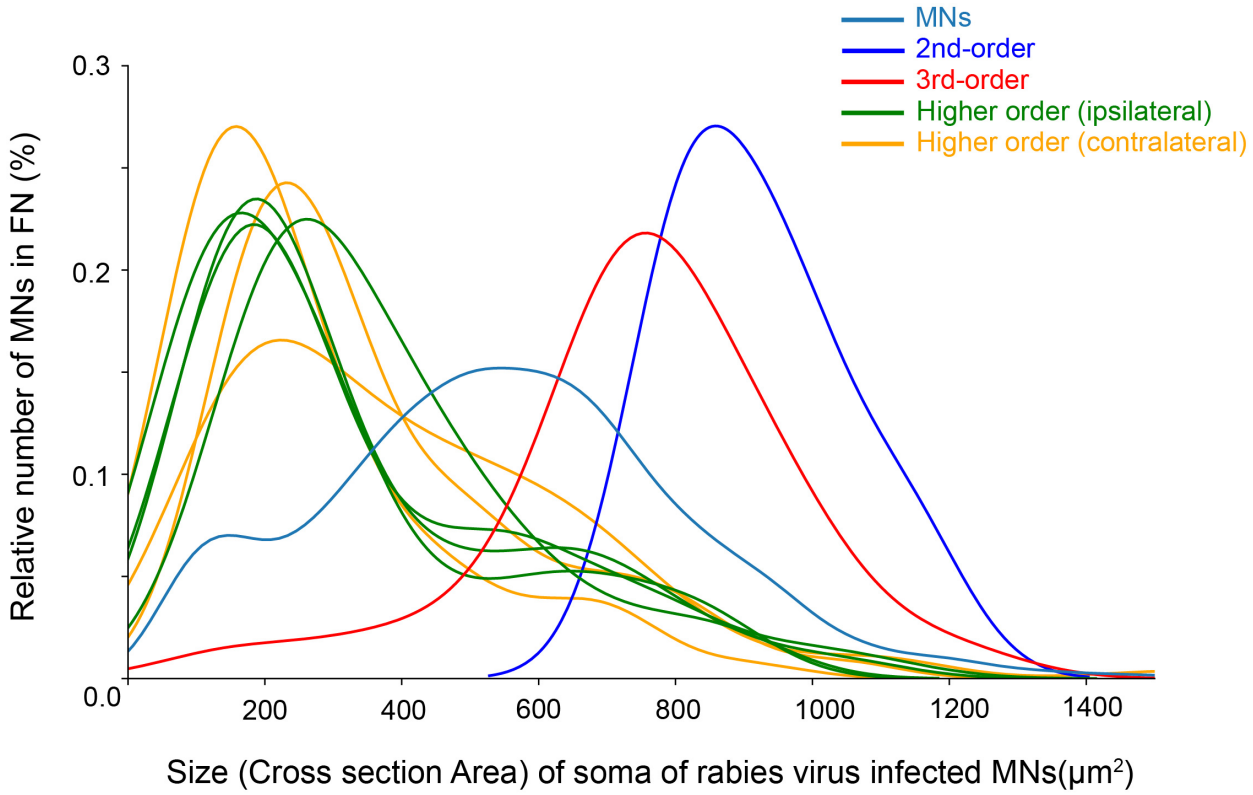

Figure 24: Distribution of neuron size across second, third and higher order brains in facial nucleus. Comparison of neuron size of rabies-infected MNs in second(purple; n=1), third(red; n=1) and higher order ((ipsilateral: green; n=4) and (contralateral:yellow; n=3)) with all neurons (light blue; n=6) in facial nucleus.

facial nucleus across first, second and third-order brains(n=6) was 549.30 ± 267.00 μm^2. Rabies-infected MNs in second- and third-order brains were significantly larger (919.93 ± 128.33 μm^2 and 755.61 ± 207.04 μm^2, respectively. However, in higher-order brains, infected MNs on the ipsilateral side (342.86 ± 248.08μm^2, 200.40 ± 231.18μm^2, 335.96 ± 237.37μm^2, and 362.51 ± 191.73 μm^2) and on the contralateral side (364.90 ± 214.96 μm^2, 258.82 ± 191.92 μm^2, and 403.61 ± 261.33 μm^2) had smaller mean areas. These findings show that in higher-order brains predominantly smaller MNs are infected whereas in the first three synaptic orders, labeling is restricted to larger MNs.

5 Discussion

In this thesis, I mapped the anatomical basis for motor control of a single vibrissa muscle across rat brain. After wild-type rabies virus was injected into a vibrissa muscle in rats, consistent retrograde transsynaptic transport of the virus was observed in motoneurons within the facial nucleus, premotor neurons across various brainstem nuclei, layer 5 pyramidal neurons (L5PNs) in the cerebral cortex.

First, I presented the cortical areas that provide disynaptic input to the MNs of a single muscle. The findings show that disynaptic drive from cortex to MNs originate from five distinct cortical areas: primary motor cortex (M1), primary somatosensory cortex(S1), secondary motor cortex (M2), secondary somatosensory cortex (S2), and anterior insular cortex (AI). In particular, M1 has subregions for contralateral or ipsilateral vibrissa muscles. The cortical control for a single vibrissa muscle is more complex than a single forelimb muscle as some of the forelimb motor control originate from areas that are comprised within those of M1, M2 and S2 that control vibrissa muscles. In contrast, S1 output pathways are disjoint, with separate pathways for forelimb and vibrissae control.

Second, in higher-order brains, where rabies-infected neurons extend beyond L5PNs, an increase in infected motoneurons (MNs) is observed in the facial nucleus of both hemispheres, predominantly affecting smaller MNs. Additionally, rabies virus-infected neurons are present in nearly all brain regions across different specimens.

Finally, application of a Faster RCNN for automated detection of rabies-infected neurons achieved high recall (0.8), with a precision of 0.684 and F1 score of 0.735, demonstrating its potential in rabies-infected neuron detection in densely labeled datasets.

5.1 Robustness of rabies virus as multitransynaptic tracer

This study is the first to use the replication-competent strain (N2c) of the rabies virus in rats to map the cortical control of the vibrissa muscle through its retrograde transsynaptic properties. Therefore, it is important to address the technical features of the approach, such as the specificity of neuronal infection in each synaptic order.

In facial nucleus, only 10-30% of MNs were infected, predominantly localized in the ventrolateral region. There is no spread to areas associated with other muscles. Even in second- and third-order brains, the infections remained sparse and confined to the VL part of the FN (Figure 16). Despite the brain-wide spread of the virus in higher order, the total increase within the FN remained limited. In addition, analyses of the size, shape and location of the MN showed that they correspond to those innervating the C3 vibrissa (Guest et al., 2018). These findings demonstrate high specificity of rabies virus in infecting MNs within the FN.

In the second-order brains, all the twenty-one premotor areas of the brainstem known to influence vibrissa protraction were infected by the rabies virus (Figure 17). This selective infection indicates the rabies virus's precision in targeting premotor neurons (preMNs) directly connected to MNs. These infected neurons includes all the excitatory and inhibitory preMNs that innervate the injected muscle (Takatoh et al., 2013). A more detailed investigation of these regions will reveal their specific influence to vibrissa movement.

In the cerebral cortex, rabies-virus infection is restricted to layer 5. Particularly in the motor cortex, the L5PNs were densely concentrated in the region most strongly associated with whisker movement. Similarly, in the sensory cortex, infection was predominantly observed in the contralateral hemisphere, specifically beneath the barrel column corresponding to the injected C3 muscle. The precise targeting confirms the virus's ability to trace direct multitransynaptic pathways without off-target infection (Kelly & Strick, 2000; Ugolini, 2010). These findings highlight the robustness and specificity of retrograde transsynaptic transport of rabies virus.

5.2 Third-order brains

5.2.1 Multiple cortical regions involved in vibrissa control

Understanding vibrissa movement's cortical control requires integrating anatomical and functional perspectives on descending projections to the brainstem (Petersen, 2014). Previous anatomical studies using anterograde and retrograde tracers have mapped descending projections from the cortex to brainstem circuits involved in vibrissa control (Economo et al., 2018; Smith et al., 2015). Additionally, functional studies have identified motor-related activity in multiple cortical regions, demonstrating their role in modulating vibrissa movement (Brecht et al., 2006; Ebbesen et al., 2017; Hattox et al., 2002). However, these approaches primarily focus on individual pathways or functional subregions, making it challenging to a comprehensive map of cortical projections to preMNs. The current thesis reveals the cortical regions that control vibrissa movement through disynaptic connections to motoneurons via premotor neurons (preMNs).

A key finding from this study is that more than two-thirds of vL5PNs with disynaptic connections to the motoneurons controlling a single vibrissa muscle originate from areas outside of contralateral M1 (Figure 18C). These regions include M2, S1, S2, and insular cortex. This expansion of motor control beyond M1 is not unique to the vibrissa system, as similar patterns have been observed for other muscle groups, including the nose and hindlimb (Kurnikova et al., 2019; Maurer et al., 2023). Descending projections originating from the supplementary motor areas (SMA) also play a significant role in the regulation and execution of voluntary movements in macaques (Strick et al., 2021). This expansion depends on the level of dexterity and complexity of the motor skill required for the muscle involved, with more intricate and finely tuned movements engaging a broader array of cortical areas beyond M1 (Mountcastle et al., 1975). Together, this finding represents the importance of the distributed nature of cortical motor control.

In this thesis, I also demonstrate the presence of rabies virus-infected neurons in both

hemispheres of the cortex. While this anatomical evidence highlights bilateral cortical contributions to vibrissa motor control, most previous studies have primarily examined contralateral projections (Matyas et al., 2010; Sreenivasan et al., 2015). This focus is partly due to the limitations of traditional monosynaptic retrograde tracers, which do not capture the multitransynaptic nature of motor control circuits, leaving the extent of bilateral projections less explored. However, functional studies using optogenetic stimulation (Auffret et al., 2018) and intracortical microstimulation (ICMS) (Halley et al., 2020) have demonstrated bilateral vibrissa movement when stimulating the motor cortex. Further research is needed to understand better how these pathways contribute to coordinated motor control.

Over one-third of vL5PNs were located in the primary somatosensory cortex (vS1), with labeling strictly confined to the contralateral hemisphere. More specifically, these neurons were concentrated in the barrel cortex, a region traditionally associated with sensory processing. This finding aligns with emerging evidence suggesting that vS1 is not merely a sensory relay but also plays an active role in motor control (Matyas et al., 2010). The barrel cortex is known to integrate sensory feedback with motor output, contributing to precise vibrissa positioning during exploratory behaviors (Feldmeyer et al., 2013; Petersen, 2014). However, stimulation studies have demonstrated distinct motor effects, with optogenetic activation of vS1 induces retraction of the whiskers (Auffret et al., 2018). Therefore, disynaptic connections from vS1 to motoneurons provide a parallel pathway from somatosensory cortex for controlling vibrissa movement.

Despite the widespread distribution of vL5PNs within M1, the dense concentration of vL5PNs is in vibrissa-related areas in M1 (Figure 19). This observation aligns with functional maps showing vibrissae movements can be evoked by M1 stimulations, even in the hindlimb area (Halley et al., 2020). Electrophysiological data further indicate that single L5PNs in rodent M1 can influence both vibrissa and other muscle activity (Mercer Lindsay et al., 2019). This finding may provide a neural framework for coordinating movements across distant body regions, enabling adaptable motor behaviors.

5.2.2 vM1, vS1 and reciprocal control of vibrissa muscles

Recent studies have shown that stimulation of vM1 evokes vibrissa protraction, while stimulation of vS1 triggers vibrissa retraction (Matyas et al., 2010). Similarly, stimulation of the reticular nuclei, which receive input from vM1, results in protraction, whereas stimulation of the trigeminal nuclei, which receive input from vS1, produces retraction (Sreenivasan et al., 2015). These observations have formed the basis of the current model, suggesting that the vM1-to-reticular pathway is primarily responsible for vibrissa protraction, while the vS1-to-trigeminal pathway governs vibrissa retraction (Figure 25A). However, this raises an intriguing question: How can the findings in this thesis, which show that vS1 is a significant source of vL5PNs with disynaptic connections to motoneurons innervating a protractor muscle, be reconciled with this model?

The proposed model resolves this contradiction by proposing distinct trigeminal preMNs: one excites retractor MNs, while the other inhibits protractor MNs (Figure 25B). Under this model, vL5PNs in vS1 could connect to both sets of preMNs, thereby exciting the MNs of retractor muscles while simultaneously inhibiting the MNs of protractor muscles. Supporting this idea, retrograde transsynaptic transport of rabies virus from the protractor muscle revealed a substantial number of second-order preMNs in the trigeminal nuclei. Furthermore, this model predicts that inactivation of vS1 would remove a source of inhibition to the MNs of protractor muscles. Consistent with this prediction, Matyas et al. demonstrated that inactivation of vS1 enhances vibrissa protraction in response to vM1 stimulation (Matyas et al., 2010). This dual role of vS1 connections provides a more nuanced understanding of its influence on motor control.

In the proposed model, vM1 serves as a source of vibrissa protraction, while vS1 provides reciprocal inhibition that suppresses vibrissa protraction. Evidence suggests that a similar arrangement exists for cortical control of vibrissa retraction (Ebbesen et al., 2017; Matyas et al., 2010). This would require that vL5PNs in vM1 connect to two sets of premotor neurons (preMNs) in the reticular nuclei: one that excites the motoneurons (MNs) of protractor

muscles and another that inhibits the MNs of retractor muscles. Consequently, the model predicts that retrograde transsynaptic transport of rabies virus from injections into a retractor muscle would label significant numbers of third-order vL5PNs not only in vS1 but also in vM1.

It remains unclear whether individual vL5PNs in vM1 branch to simultaneously excite vibrissa protraction and inhibit vibrissa retraction, or if vL5PNs in vS1 branch to excite vibrissa retraction and inhibit vibrissa protraction. Additionally, it is possible that vS1 contains a subset of vL5PNs that contribute to vibrissa protraction. These questions will require further investigation using double-labeling techniques with viral transport from both protractor and retractor muscles, as well as physiological studies to examine branching patterns. Despite these uncertainties, our findings strongly indicate that both vM1 and vS1 serve as sources of activation for vibrissa muscle agonists while simultaneously providing reciprocal inhibition for vibrissa muscle antagonists.

One important implication of our findings is the emphasis on cortical inhibition in regulating muscle activity. As noted earlier, the number of vL5PNs in vS1 is substantial, comparable to the number of vL5PNs in vM1. According to our model, the primary effect of the descending signals from vS1 is inhibitory. This suggests that a significant component of the cortical motor command involves active inhibition, which plays a critical role in shaping vibrissa muscle activity. This highlights the importance of inhibitory mechanisms in fine-tuning motor output and coordinating complex motor behaviors (Ebbesen & Brecht, 2017).

The findings from rabies virus injections into the EDC muscle suggest that the model proposed for cortical control of vibrissae may extend to other motor systems. In the forelimb, motor and sensory cortices appear to exert opposing influences on movement, mirroring the observation in vibrissa control. Stimulation studies demonstrate that activation of fS1 induces retractive movements, such as wrist flexion, whereas stimulation of fM1 elicits forward movements, including forepaw elevation and wrist extension (Halley et al., 2020).

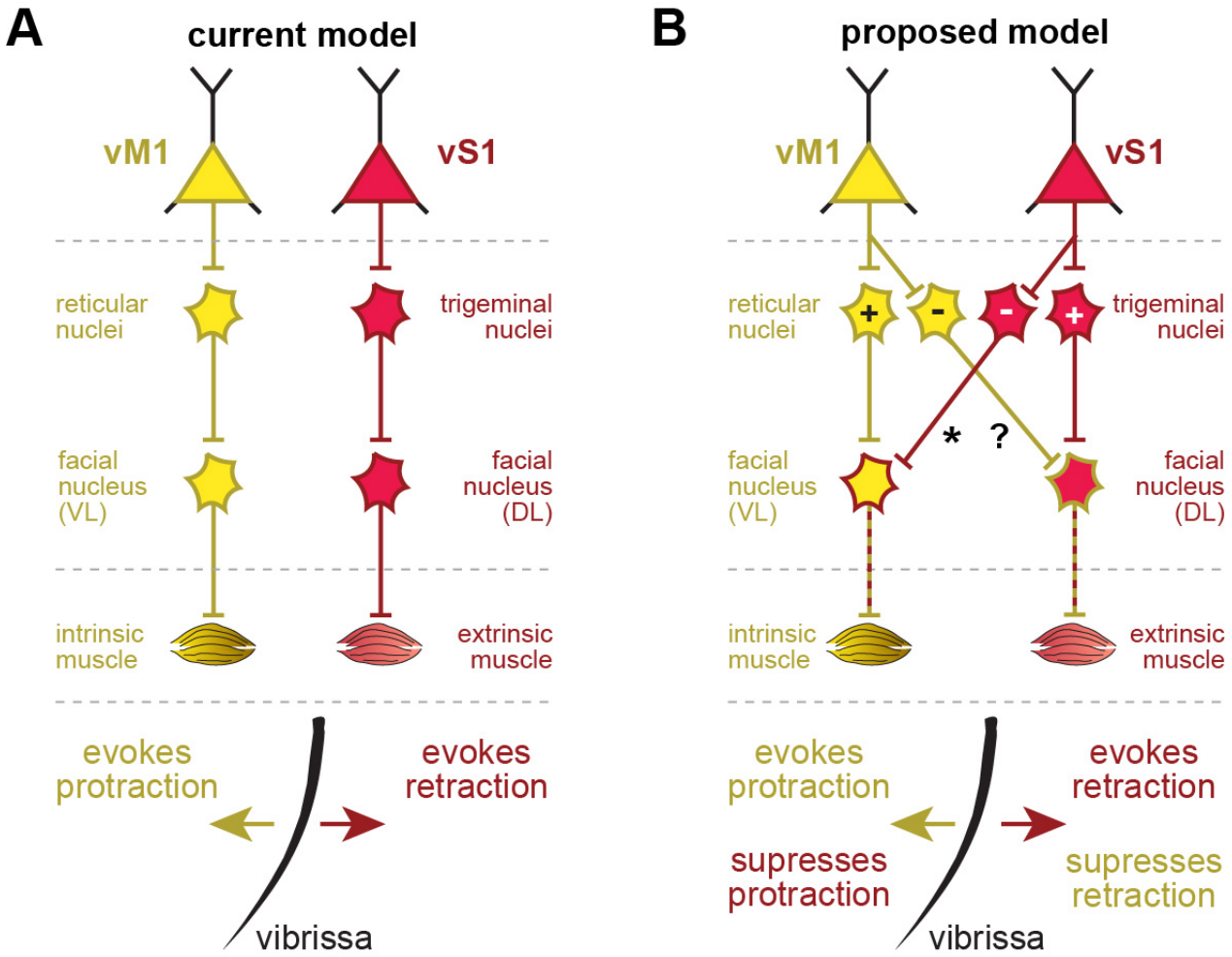

Figure 25: Comparison of current and proposed models for cortical control of vibrissa movement. (A) In the current model, vM1 controls intrinsic muscle (vM1->reticular nuclei ->MNs in VL facial nucleus-> protraction by intrinsic muscle) and vS1 controls extrinsic muscle from a separate pathways (vS1->trigeminal nuclei ->MNs in DL facial nucleus-> retraction by extrinsic muscle). (B) In the proposed model, vS1 and vM1 exert reciprocal inhibitory effects on both intrinsic and extrinsic muscles, suggesting a more integrated system for finer whisker movement control. The asterisk (*) denotes the pathway demonstrated by the current results. The question mark (?) denotes a predicted pathway. vM1, vibrissa primary motor cortex; vS1, vibrissa primary somatosensory cortex, VL, ventrolateral; DL, dorsolateral; MNs, motoneurons.

In addition, because fL5PNs appear only in third-order brains, fL5PNs have disynaptic connections to the motoneurons (MNs) of EDC, a forelimb muscle responsible for wrist extension and digit spreading. This push-pull mechanism between primary motor and somatosensory cortex may represent a fundamental organizational principle of descending control across multiple muscle groups.

5.2.3 Insular cortex

The rabies-infected neurons observed in both hemispheres of the insular cortex at the third-synaptic order following vibrissa muscle injections provide compelling evidence for a more direct involvement of this region in the motor control. This finding challenges the conventional view that the insular cortex primarily serves diverse roles in emotion, sensory-emotional integration, learning, risk estimation, empathy, stress, and anxiety (Gogolla, 2017). Recent study found that there are projection from the insular cortex to the brainstem (Gehrlach et al., 2020). These findings open new avenues for understanding how the insular cortex integrates sensory, emotional, and motor information to guide behaviors. Further research is needed to explore the functional significance of these projections and their contribution to motor control across different contexts and muscle groups.

In contrast to vibrissa injection, rabies infection was notably absent in the insular cortex following injections into the forelimb muscle (extensor digitorum communis, EDC). The forelimb, which is primarily involved in locomotion and object manipulation, rely on direct voluntary motor control from M1 and S1 (Halley et al., 2020). It also received motor control input from S2 (Neafsey & Sievert, 1982). Additionally, I show that S2 is also involved in motor control. In comparison, the insular cortex could play a significant role in the contextual modulation of vibrissa movement. This distinction is supported by clinical observations in humans with volitional facial paresis. The individual with this condition loses the ability to voluntarily control facial muscles on one side of the face, typically due to damage in the motor cortex or corticobulbar tract. However, spontaneous or emotionally driven facial movements, such as smiling or laughing, often remain intact (Hopf et al., 1992). Therefore, the insular cortex's contextual modulation of movement may not be universal across all muscle groups but may be specific to certain functional contexts.

5.3 Higher-order brains

There is a substantial increase in rabies-infected neurons in higher-order brains, where transsynaptic transport of the rabies virus extends beyond layer 5 of the cerebral cortex. This increase was observed in previously labeled regions, including the facial nucleus, brainstem nuclei, midbrain, cerebellum, and cerebral cortex (Figure 14). Additionally, rabies-infected neurons were identified in new brain regions that had not been previously observed in second- and third-order brains(Figure 26-34). Further analysis is needed to understand how these additional connections contribute to motor output.

Categorizing higher-order brains is challenging due to complex projections across multiple regions. The minimal labeling in the facial nucleus offers critical insights, which I will discuss in the next section.

5.3.1 Facial nucleus

No rabies-infected motoneurons (MNs) exist in the contralateral facial nucleus, with this labeling only appearing in higher-order brains. The unilateral facial nucleus labeling indicates the absence of direct projections or cross-talk between the two facial nuclei. This suggests that motoneurons control their respective muscles without directly modulating activity across hemispheres. Instead, interhemispheric coordination of facial movements likely occurs through upstream premotor circuits (Mercer Lindsay et al., 2019). The finding highlights the role of higher-order brain regions in integrating bilateral vibrissa motor control.

The observation of two distinct types of motoneurons (MNs) in the facial nucleus—larger MNs in lower-order brains and smaller MNs in higher-order brains—suggests functionally distinct roles in motor control (Figure 24). Larger MNs, primarily found in lower-order brains, are well-established as the main drivers of vibrissa protraction, directly controlling muscle contraction (Ashwell, 1982; Guest et al., 2018; Hinrichsen & Watson, 1984; Wat-

son et al., 1982). In contrast, the presence of smaller MNs in higher-order brains indicates its role as interneurons. Anterograde labeling has shown that these smaller MNs project to respiratory brainstem nuclei (Li et al., 2004), and functional study suggests that interneurons in the facial nucleus may modulate respiration (C. Zhang et al., 2004). Given that whisking is closely synchronized with breathing in rodents, these interneurons may contribute to coordinating vibrissae movements with respiratory rhythms during exploratory behaviors (Moore et al., 2013). However, since their labeling appears only in higher-order brains, their influence on motor control may be more indirect, integrating contextual or rhythmic modulation rather than driving immediate movement.

5.4 Machine learning

This thesis demonstrated the first application of Faster R-CNN for the automated detection of rabies-infected neurons in confocal microscopy images from rat brain. Faster R-CNN models exhibited its highest accuracy in less dense regions which can be useful in analyzing first, second, and third-order brain regions where neurons are sparsely distributed and labeling is less challenging. This aligns with observations that show deep learning techniques perform well in less complex regions (Yoon et al., 2019). However, the challenge of low accuracy in high-density regions remains with this model as reported by Cauzzo et al., 2024. This is mainly due to overlapping which create ambiguous boundaries that were difficult for the model to segment. Alternative architectures, such as Mask R-CNN, may offer potential solutions (Bharati & Pramanik, 2020).

Furthermore, inconsistent labeling introduced noise in the training data, reducing model performance. This can be improved using a standardized annotation techniques (D. Zhang et al., 2012). The impact of datasets size and diversity was also evident, with models trained on more diverse datasets from larger dataset demonstrate improved performance. Use of neuronal morphology for improved performance is also a promising approach (Mata et al., 2019). This is consistent with the broader trend of using supervised machine learn-

ing for phenotyping that captures cytoarchitectures (Štajduhar et al., 2023). Similarly, CNNs have been successfully used to detect healthy neurons in acute slices with YOLOv3, achieving high precision and recall (Yip et al., 2021).

Despite these limitations, the findings provided the potential benefits of deep learning for neuron detection in confocal images of rabies-infected brain tissues. Addressing the challenges, particularly the lower accuracy in high-density regions, will be crucial in developing a robust and efficient tool for high-throughput analysis.

5.5 Outlook

The findings of this thesis reveal that cortical motor control of a single vibrissa muscle extends beyond the primary motor cortex (M1) and includes the primary somatosensory cortex (S1), the secondary motor cortex (M2), secondary somatosensory cortex (S2), and the insular cortex. vS1 and vM1 differ in their projections to vibrissa muscles, with vS1 projecting unilaterally and vM1 projecting bilaterally. A comparison of forelimb and vibrissa muscle shows representation in M1 overlap, whereas S1 maintains a topologically disjoint organization. These distinct representations in M1 and S1 highlight their differing contributions to muscle control. Further functional mapping and circuit-tracing approaches can help explore how M1 and S1 interact at the brainstem level to coordinate motor output. Additionally, the role of the insular cortex in vibrissa and facial motor control remains unclear. Future functional studies should investigate its involvement in voluntary motor control.

Interestingly, in the facial nucleus, this study demonstrates a strikingly sparse distribution of infected motoneurons (MNs) in higher-order brains, despite the exponential increase in infected neurons in other brain regions, including the cerebral cortex, cerebellum, and midbrain. High-resolution connectomics combined with functional mapping could provide deeper insights into why the motoneuron pool remains limited despite extensive motor input.

The Faster RCNN performed well in detecting rabies-infected neurons, particularly in low-density regions, but challenges remain. Refining model architectures could enhance detection accuracy in densely labeled areas across different brain regions and accelerate large-scale neuron detection for anatomical studies.

In conclusion, this thesis provides the anatomical basis for cortical control of a single vibrissa muscle in rats. It reveals a distributed organization spanning multiple cortical areas and offers new insights into the hierarchical structure of motor control.

6 Abstract

How does the cerebral cortex control a single muscle to orchestrate movement? Rabies virus was injected into the intrinsic muscle that protracts the rat C3 vibrissa. The retrograde transneuronal transport of rabies virus was used to identify the most direct output pathways from the cerebral cortex to a single muscle that moves facial vibrissae.

The results show that the most direct cortical output pathways responsible for control of this muscle originate from almost entire primary motor cortex (M1), vibrissae-related primary somatosensory cortex – barrel cortex(S1), secondary somatosensory (S2)and motor cortex(M2), and insular cortex. Apart from the barrel cortex, all these regions exhibit bilateral organization. Interestingly, M1 contains distinct subregions in both hemispheres that can differentially contribute to the control of contralateral and ipsilateral vibrissa muscles.

For comparison, the rabies virus was also injected into a single forepaw muscle, extensor digitorium communis (EDC). The direct cortical output pathways for forelimb motor control originate majority from contralateral cortical regions that were also represented by the vibrissae, particularly in M1, M2, and S2 and minor overlap in S1. However, output pathways from S1 are topographically organized and remain segregated for forelimb and vibrissae movements. This topological distinction suggests fundamental differences in how cortex integrate information for different muscle groups.

Surprisingly, while infected neurons were observed in the insular cortex for vibrissa control, no neurons were detected in this region for forelimb control. This suggests that its role is specific to facial motor functions. This also highlights that the cortical output system for controlling a single vibrissa muscle is more complex than that for a single forelimb muscle.

In the final part of this study, I also examined the distribution of rabies-infected motoneurons (vMNs) in the facial nucleus (FN) in higher-order brains. I observed a higher number of infected vMNs along with labeling in the contralateral FN, indicating the presence of indirect interhemispheric projections. Additionally, mean size of these vMNs was lower

compared to second and third-order brains, indicating potential differences in functional roles or connectivity patterns of these vMNs.

In conclusion, the findings reveal that multiple functionally distinct cortical areas, both within and beyond the primary motor cortex (M1), contribute in parallel to the control of individual muscles. The evidence shows that robustness rabies virus tracing is a powerful tool for studying the anatomical basis of motor control in rats. These insights offer a foundation for further research into the hierarchical and integrative mechanisms underlying motor control in mammals.

7 List of figures

8 List of tables

9 References

Ashwell, K. W. (1982). The adult mouse facial nerve nucleus: Morphology and musculotopic organization. *Journal of anatomy*, *135*, 531–8.

Auffret, M., Ravano, V. L., Rossi, G. M., Hankov, N., Petersen, M. F., & Petersen, C. C. (2018). Optogenetic Stimulation of Cortex to Map Evoked Whisker Movements in Awake Head-Restrained Mice. *Neuroscience*, *368*, 199–213. https://doi.org/10.1016/j.neuroscience.2017.04.004

Berg, R. W., & Kleinfeld, D. (2003). Rhythmic whisking by rat: Retraction as well as protraction of the vibrissae is under active muscular control. *Journal of Neurophysiology*, *89*(1), 104–117. https://doi.org/10.1152/jn.00600.2002

Bharati, P., & Pramanik, A. (2020). Deep Learning Techniques—R-CNN to Mask R-CNN: A Survey. In A. K. Das, J. Nayak, B. Naik, S. K. Pati, & D. Pelusi (Eds.), *Computational Intelligence in Pattern Recognition* (pp. 657–668, Vol. 999). Springer Singapore. https://doi.org/10.1007/978-981-13-9042-5_56

Brecht, M., Grinevich, V., Jin, T.-E., Margrie, T., & Osten, P. (2006). Cellular mechanisms of motor control in the vibrissal system. *Pflügers Archiv - European Journal of Physiology*, *453*(3), 269–281. https://doi.org/10.1007/s00424-006-0101-6

Brecht, M., Preilowski, B., & Merzenich, M. M. (1997). Functional architecture of the mystacial vibrissae. *Behavioural Brain Research*, *84*(1-2), 81–97. https://doi.org/10.1016/S0166-4328(97)83328-1

Cauzzo, S., Bruno, E., Boulet, D., Nazac, P., Basile, M., Callara, A. L., Tozzi, F., Ahluwalia, A., Magliaro, C., Danglot, L., & Vanello, N. (2024). A modular framework for multi-scale tissue imaging and neuronal segmentation. *Nature Communications*, *15*(1), 4102. https://doi.org/10.1038/s41467-024-48146-y

Dercksen, V. J., Hege, H.-C., & Oberlaender, M. (2014). The filament editor: An interactive software environment for visualization, proof-editing and analysis of 3D neuron morphology. *Neuroinformatics*, *12*(2), 325–339. https://doi.org/10.1007/s12021-013-9213-2

Deschênes, M., Kurnikova, A., Elbaz, M., & Kleinfeld, D. (2016). Circuits in the Ventral Medulla That Phase-Lock Motoneurons for Coordinated Sniffing and Whisking. *Neural Plasticity*, *2016*, 1–9. https://doi.org/10.1155/2016/7493048

Diamond, M. E., von Heimendahl, M., Knutsen, P. M., Kleinfeld, D., & Ahissar, E. (2008). 'Where' and 'what' in the whisker sensorimotor system. *Nature Reviews Neuroscience*, *9*(8), 601–612. https://doi.org/10.1038/nrn2411

Dörfl, J. (1982). The musculature of the mystacial vibrissae of the white mouse. *Journal of anatomy*, *135*, 147–54.

Dum, R. P., & Strick, P. L. (1991). The origin of corticospinal projections from the premotor areas in the frontal lobe. *The Journal of Neuroscience*, *11*(3), 667–689. https://doi.org/10.1523/JNEUROSCI.11-03-00667.1991

Ebbesen, C. L., & Brecht, M. (2017). Motor cortex — to act or not to act? *Nature Reviews Neuroscience*, *18*(11), 694–705. https://doi.org/10.1038/nrn.2017.119

Ebbesen, C. L., Doron, G., Lenschow, C., & Brecht, M. (2017). Vibrissa motor cortex activity suppresses contralateral whisking behavior. *Nature Neuroscience*, *20*(1), 82–89. https://doi.org/10.1038/nn.4437

Economo, M. N., Viswanathan, S., Tasic, B., Bas, E., Winnubst, J., Menon, V., Graybuck, L. T., Nguyen, T. N., Smith, K. A., Yao, Z., Wang, L., Gerfen, C. R., Chandrashekar, J., Zeng, H., Looger, L. L., & Svoboda, K. (2018). Distinct descending motor cortex pathways and their roles in movement. *Nature*, *563*(7729), 79–84. https://doi.org/10.1038/s41586-018-0642-9

Egger, R., Narayanan, R. T., Helmstaedter, M., de Kock, C. P. J., & Oberlaender, M. (2012). 3D reconstruction and standardization of the rat vibrissal cortex for precise registration of single neuron morphology (K. Briggman, Ed.). *PLoS Computational Biology*, *8*(12), e1002837. https://doi.org/10.1371/journal.pcbi.1002837

Feldmeyer, D., Brecht, M., Helmchen, F., Petersen, C. C. H., Poulet, J. F., Staiger, J. F., Luhmann, H. J., & Schwarz, C. (2013). Barrel cortex function. *Progress in Neurobiology*, *103*, 3–27. https://doi.org/10.1016/j.pneurobio.2012.11.002

Gehrlach, D. A., Weiand, C., Gaitanos, T. N., Cho, E., Klein, A. S., Hennrich, A. A., Conzelmann, K.-K., & Gogolla, N. (2020). A whole-brain connectivity map of mouse insular cortex. *eLife*, *9*, e55585. https://doi.org/10.7554/eLife.55585

Girshick, R., Donahue, J., Darrell, T., & Malik, J. (2014). Rich Feature Hierarchies for Accurate Object Detection and Semantic Segmentation. *2014 IEEE Conference on Computer Vision and Pattern Recognition*, 580–587. https://doi.org/10.1109/CVPR.2014.81

Gogolla, N. (2017). The insular cortex. *Current Biology*, *27*(12), R580–R586. https://doi.org/10.1016/j.cub.2017.05.010

Guest, J. M., Seetharama, M. M., Wendel, E. S., Strick, P. L., & Oberlaender, M. (2018). 3D reconstruction and standardization of the rat facial nucleus for precise mapping of vibrissal motor networks. *Neuroscience*, *368*, 171–186. https://doi.org/10.1016/j.neuroscience.2017.09.031

Haidarliu, S., Nelinger, G., Gantar, L., Ahissar, E., & Saraf-Sinik, I. (2023). Functional anatomy of mystacial active sensing in rats. *Anatomical Record (Hoboken, N.J.: 2007)*. https://doi.org/10.1002/ar.25305

Haidarliu, S., Simony, E., Golomb, D., & Ahissar, E. (2010). Muscle architecture in the mystacial pad of the rat. *The Anatomical Record: Advances in Integrative Anatomy and Evolutionary Biology*, *293*(7), 1192–1206. https://doi.org/10.1002/ar.21156

Halley, A. C., Baldwin, M. K. L., Cooke, D. F., Englund, M., & Krubitzer, L. (2020). Distributed Motor Control of Limb Movements in Rat Motor and Somatosensory Cortex: The Sensorimotor Amalgam Revisited. *Cerebral Cortex*, *30*(12), 6296–6312. https://doi.org/10.1093/cercor/bhaa186

Hattox, A. M., Priest, C. A., & Keller, A. (2002). Functional circuitry involved in the regulation of whisker movements. *The Journal of Comparative Neurology*, *442*(3), 266–276. https://doi.org/10.1002/cne.10089

Herfst, L. J., & Brecht, M. (2008). Whisker movements evoked by stimulation of single motor neurons in the facial nucleus of the rat. *Journal of Neurophysiology*, *99*(6), 2821–2832. https://doi.org/10.1152/jn.01014.2007

Hill, D. N., Bermejo, R., Zeigler, H. P., & Kleinfeld, D. (2008). Biomechanics of the vibrissa motor plant in rat: Rhythmic whisking consists of triphasic neuromuscular activity. *Journal of Neuroscience*, *28*(13), 3438–3455. https://doi.org/10.1523/JNEUROSCI.5008-07.2008

Hinrichsen, C. F., & Watson, C. D. (1984). The facial nucleus of the rat: Representation of facial muscles revealed by retrograde transport of horseradish peroxidase. *The Anatomical Record*, *209*(3), 407–415. https://doi.org/10.1002/ar.1092090321

Hopf, H. C., Müller-Forell, W., & Hopf, N. J. (1992). Localization of emotional and volitional facial paresis. *Neurology*, *42*(10), 1918–1923. https://doi.org/10.1212/wnl.42.10.1918

Isokawa-Akesson, M., & Komisaruk, B. R. (1987). Difference in projections to the lateral and medial facial nucleus: Anatomically separate pathways for rhythmical vibrissa

movement in rats. *Experimental Brain Research*, *65*(2), 385–398. https://doi.org/10.1007/BF00236312

Kelly, R. M., & Strick, P. L. (2000). Rabies as a transneuronal tracer of circuits in the central nervous system. *Journal of Neuroscience Methods*, *103*(1), 63–71. https://doi.org/10.1016/S0165-0270(00)00296-X

Kelly, R. M., & Strick, P. L. (2003). Cerebellar loops with motor cortex and prefrontal cortex of a nonhuman primate. *The Journal of Neuroscience*, *23*(23), 8432–8444. https://doi.org/10.1523/JNEUROSCI.23-23-08432.2003

Klein, B. G., & Rhoades, R. W. (1985). Representation of whisker follicle intrinsic musculature in the facial motor nucleus of the rat. *The Journal of Comparative Neurology*, *232*(1), 55–69. https://doi.org/10.1002/cne.902320106

Kleinfeld, D., Berg, R. W., & O'Connor, S. M. (1999). Anatomical loops and their electrical dynamics in relation to whisking by rat. *Somatosensory & Motor Research*, *16*(2), 69–88. https://doi.org/10.1080/08990229970528

Kleinfeld, D., Moore, J. D., Wang, F., & Deschênes, M. (2014). The brainstem oscillator for whisking and the case for breathing as the master clock for orofacial motor actions. *Cold Spring Harbor Symposia on Quantitative Biology*, *79*, 29–39. https://doi.org/10.1101/sqb.2014.79.024794

Kurnikova, A., Deschênes, M., & Kleinfeld, D. (2019). Functional brain stem circuits for control of nose motion. *Journal of Neurophysiology*, *121*(1), 205–217. https://doi.org/10.1152/jn.00608.2018

Li, C., Guanb, Z., Chanc, Y., & Zhenga, Y. (2004). Projections from facial nucleus interneurons to the respiratory groups of brainstem in the rat. *Neuroscience Letters*, *368*(1), 25–28. https://doi.org/10.1016/j.neulet.2004.06.080

Mata, G., Radojević, M., Fernandez-Lozano, C., Smal, I., Werij, N., Morales, M., Meijering, E., & Rubio, J. (2019). Automated Neuron Detection in High-Content Fluorescence Microscopy Images Using Machine Learning. *Neuroinformatics*, *17*(2), 253–269. https://doi.org/10.1007/s12021-018-9399-4

Matyas, F., Sreenivasan, V., Marbach, F., Wacongne, C., Barsy, B., Mateo, C., Aronoff, R., & Petersen, C. C. H. (2010). Motor control by sensory cortex. *Science*, *330*(6008), 1240–1243. https://doi.org/10.1126/science.1195797

Maurer, L., Brown, M., Saggi, T., Cardiges, A., & Kolarcik, C. L. (2023). Hindlimb muscle representations in mouse motor cortex defined by viral tracing. *Frontiers in Neuroanatomy*, *17*, 965318. https://doi.org/10.3389/fnana.2023.965318

Mercer Lindsay, N., Knutsen, P. M., Lozada, A. F., Gibbs, D., Karten, H. J., & Kleinfeld, D. (2019). Orofacial movements involve parallel corticobulbar projections from motor cortex to trigeminal premotor nuclei. *Neuron*, *104*(4), 765–780.e3. https://doi.org/10.1016/j.neuron.2019.08.032

Mitchinson, B., Pearson, M., Melhuish, C., & Prescott, T. J. (2006). A Model of Sensorimotor Coordination in the Rat Whisker System. In S. Nolfi, G. Baldassarre, R. Calabretta, J. C. T. Hallam, D. Marocco, J.-A. Meyer, O. Miglino, & D. Parisi (Eds.). D. Hutchison, T. Kanade, J. Kittler, J. M. Kleinberg, F. Mattern, J. C. Mitchell, M. Naor, O. Nierstrasz, C. Pandu Rangan, B. Steffen, M. Sudan, D. Terzopoulos, D. Tygar, M. Y. Vardi, & G. Weikum (**typeredactors**), *From Animals to Animats 9* (pp. 77–88, Vol. 4095). Springer Berlin Heidelberg. https://doi.org/10.1007/11840541_7

Moore, J. D., Deschênes, M., Furuta, T., Huber, D., Smear, M. C., Demers, M., & Kleinfeld, D. (2013). Hierarchy of orofacial rhythms revealed through whisking and breathing. *Nature*, *497*(7448), 205–210. https://doi.org/10.1038/nature12076

Mountcastle, V. B., Lynch, J. C., Georgopoulos, A., Sakata, H., & Acuna, C. (1975). Posterior parietal association cortex of the monkey: Command functions for operations within extrapersonal space. *Journal of Neurophysiology*, *38*(4), 871–908. https://doi.org/10.1152/jn.1975.38.4.871

Neafsey, E., & Sievert, C. (1982). A second forelimb motor area exists in rat frontal cortex. *Brain Research*, *232*(1), 151–156. https://doi.org/10.1016/0006-8993(82)90617-5

Paxinos, G., & Watson, C. (2006). *The rat brain in stereotaxic coordinates* (6th ed.). Academic Press Inc.

Petersen, C. C. H. (2007). The Functional Organization of the Barrel Cortex. *Neuron*, *56*(2), 339–355. https://doi.org/10.1016/j.neuron.2007.09.017
MAG ID: 2100212553.

Petersen, C. C. H. (2014). Cortical Control of Whisker Movement. *Annual Review of Neuroscience*, *37*(1), 183–203. https://doi.org/10.1146/annurev-neuro-062012-170344
MAG ID: 2163040994.

Petersen, C. C. H. (2019). Sensorimotor processing in the rodent barrel cortex. *Nature Reviews Neuroscience*, *20*(9), 533–546. https://doi.org/10.1038/s41583-019-0200-y

Rathelot, J.-A., & Strick, P. L. (2006). Muscle representation in the macaque motor cortex: An anatomical perspective. *Proceedings of the National Academy of Sciences*, *103*(21), 8257–8262. https://doi.org/10.1073/pnas.0602933103

Smith, J. B., Watson, G. D. R., Alloway, K. D., Schwarz, C., & Chakrabarti, S. (2015). Corticofugal projection patterns of whisker sensorimotor cortex to the sensory trigeminal nuclei. *Frontiers in Neural Circuits*, *9*. https://doi.org/10.3389/fncir.2015.00053

Sreenivasan, V., Karmakar, K., Rijli, F. M., & Petersen, C. C. H. (2015). Parallel pathways from motor and somatosensory cortex for controlling whisker movements in mice.

The European Journal of Neuroscience, *41*(3), 354–367. https://doi.org/10.1111/ejn.12800

Štajduhar, A., Lipić, T., Lončarić, S., Judaš, M., & Sedmak, G. (2023). Interpretable machine learning approach for neuron-centric analysis of human cortical cytoarchitecture. *Scientific Reports*, *13*(1), 5567. https://doi.org/10.1038/s41598-023-32154-x

Stalling, D., Westerhoff, M., & Hege, H.-C. (2005). Amira - a highly interactive system for visual data analysis. In *The visualization handbook* (pp. 749–67).

Strick, P. L., Dum, R. P., & Rathelot, J.-A. (2021). The cortical motor areas and the emergence of motor skills: A neuroanatomical perspective. *Annual Review of Neuroscience*, *44*(1), annurev–neuro–070918–050216. https://doi.org/10.1146/annurev-neuro-070918-050216

Takatoh, J., Nelson, A., Zhou, X., Bolton, M. M., Ehlers, M. D., Arenkiel, B. R., Mooney, R., & Wang, F. (2013). New modules are added to vibrissal premotor circuitry with the emergence of exploratory whisking. *Neuron*, *77*(2), 346–360. https://doi.org/10.1016/j.neuron.2012.11.010

Tang, Y., Rampin, O., Giuliano, F., & Ugolini, G. (1999). Spinal and brain circuits to motoneurons of the bulbospongiosus muscle: Retrograde transneuronal tracing with rabies virus. *The Journal of comparative neurology*, *414*(2), 167–92.

Ugolini, G. (2010). Advances in viral transneuronal tracing. *Journal of Neuroscience Methods*, *194*(1), 2–20. https://doi.org/10.1016/j.jneumeth.2009.12.001

Watson, C. R., Sakai, S., & Armstrong, W. (1982). Organization of the facial nucleus in the rat. *Brain, Behavior and Evolution*, *20*(1-2), 19–28. https://doi.org/10.1159/000121578

Wineski, L. E. (1985). Facial morphology and vibrissal movement in the golden hamster. *Journal of Morphology*, *183*(2), 199–217. https://doi.org/10.1002/jmor.1051830208

Woolsey, T. A., & Van der Loos, H. (1970). The structural organization of layer IV in the somatosensory region (SI) of mouse cerebral cortex. The description of a cortical field composed of discrete cytoarchitectonic units. *Brain Research*, *17*(2), 205–242. https://doi.org/10.1016/0006-8993(70)90079-x

Yip, M. C., Gonzalez, M. M., Valenta, C. R., Rowan, M. J. M., & Forest, C. R. (2021). Deep learning-based real-time detection of neurons in brain slices for in vitro physiology. *Scientific Reports*, *11*(1), 6065. https://doi.org/10.1038/s41598-021-85695-4

Yoon, J.-S., Choi, E. Y., Saad, M., & Choi, T.-S. (2019). Automated integrated system for stained neuron detection: An end-to-end framework with a high negative predictive rate. *Computer Methods and Programs in Biomedicine*, *180*, 105028. https://doi.org/10.1016/j.cmpb.2019.105028

Zhang, C., Yan, H., Li, C., & Zheng, Y. (2004). Possible involvement of the facial nucleus in regulation of respiration in rats. *Neuroscience Letters*, *367*(3), 283–288. https://doi.org/10.1016/j.neulet.2004.06.047

Zhang, D., Islam, M. M., & Lu, G. (2012). A review on automatic image annotation techniques. *Pattern Recognition*, *45*(1), 346–362. https://doi.org/10.1016/j.patcog.2011.05.013

10 Appendix

Table 3: Table of rabies virus-infected neurons in cortex of third-order brains.

cortex regions	Abbre.	Ipsi	Contra
motor cortex	M1/M2	875	1677
superior colliculus	S1/S2	293	1286
Insular cortex	AI	120	70
	Total	1288	3033

Table 4: Table of rabies virus-infected neurons in midbrain of third-order brains.

Midbrain regions	Abbre.	Ipsi	Contra
zona incerta	ZI	12	77
superior colliculus	SC	956	2257
subthalamic nucleus	SubTH	1	1
red nucleus	RN	20	104
periaqueductal gray	PAG	518	584
substantia nigra	SN	41	105
	Total	1548	3128

Table 5: Table of rabies virus-infected neurons in cerebellum of third-order brains.

cerebellum regions		Ipsi	Contra
deep cerebellar nucleus, medial		866	584
deep cerebellar nucleus, lateral		1186	1866
	Total	2052	2450

Table 6: Table of rabies virus-infected neurons in brainstem of second-order brains.

Brainstem regions	**Abbre.**	**ipsilateral**	**contralateral**
medullary reticular nucleus, dorsal	MdD	121	2
medullary reticular nucleus, ventral	MdV	40	30
intermediate reticular nucleus	IRt	116	28
paramedian reticular nucleus	PMn	16	7
parvicellular reticular nucleus	PCRt	54	13
gigantocellular reticular nucleus	Gi	285	73
pontine reticular nucleus	PnC	29	22
dorsal paragigantocellular nucleus	DPGi	15	8
lateral paragigantocellular nucleus	LPGi	37	13
lateral reticular nucleus	LRt	3	0
spinal trigeminal nucleus, caudal	Sp5C	12	0
spinal trigeminal nucleus, interpolaris	Sp5I	61	0
spinal trigeminal nucleus, oralis	SP5O	8	0
principal sensory trigeminal nucleus	Pr5	5	0
spinal vestibular nucleus	SpVe	3	2
vestibular nucleus	Ve	3	0
solitary tract	Sol	0	1
Bötzinger complex	Bo	4	2
prepositus nucleus	Pr	7	3
inferior olive	IO	1	0
ambiguus nucleus	Amb	1	0
	Total	830	204

Table 7: Table of rabies virus-infected neurons in brainstem of third-order brains.

Brainstem regions	**Abbre.**	**ipsilateral**	**contralateral**
medullary reticular nucleus, dorsal	MdD	2323	595
medullary reticular nucleus, ventral	MdV	1608	1580
intermediate reticular nucleus	IRt	2404	1870
paramedian reticular nucleus	PMn	156	126
parvicellular reticular nucleus	PCRt	2057	1312
gigantocellular reticular nucleus	Gi	3826	3295
pontine reticular nucleus	PnC	337	293
dorsal paragigantocellular nucleus	DPGi	224	191
lateral paragigantocellular nucleus	LPGi	450	272
lateral reticular nucleus	LRt	138	99
spinal trigeminal nucleus, caudal	Sp5C	2272	129
spinal trigeminal nucleus, interpolaris	Sp5I	2084	412
spinal trigeminal nucleus, oralis	SP5O	615	357
principal sensory trigeminal nucleus	Pr5	135	178
spinal vestibular nucleus	SpVe	299	383
vestibular nucleus	Ve	281	382
solitary tract	Sol	309	106
Bötzinger complex	Bo	73	69
prepositus nucleus	Pr	23	49
inferior olive	IO	19	6
ambiguus nucleus	Amb	85	71
non-premotor areas		3684	2439
	Total	23402	14215

Table 8: Recall performance of Faster R-CNN Models on test datasets.

Test data ID	Model 1	Model 2	Model 5	Model 4	Model 5
1	0.554007	0.69338	0.770035	0.682927	0.691638
2	0.660935	0.791953	0.821183	0.751719	0.742435
3	0.63934	0.810418	0.865927	0.790777	0.792485
4	0.70892	0.815336	0.858842	0.852269	0.856338
5	0.615258	0.860336	0.885972	0.838187	0.849467
6	0.552834	0.813016	0.79846	0.76725	0.796781
7	0.705802	0.843983	0.865935	0.846139	0.854175
8	0.76759	0.844142	0.860829	0.822295	0.833993
9	0.556617	0.793607	0.804132	0.74693	0.763009
10	0.961729	0.856705	0.86766	0.844873	0.875402
11	0.867576	0.913512	0.924637	0.906872	0.912435

Table 9: Precision performance of Faster R-CNN Models on test datasets.

Test data ID	Model 1	Model 2	Model 5	Model 4	Model 5
1	0.987578	0.768	0.71637	0.798371	0.764933
2	0.997403	0.787205	0.740453	0.843895	0.82022
3	0.996451	0.757584	0.718233	0.823355	0.817274
4	0.996919	0.678739	0.669758	0.743989	0.759789
5	0.998336	0.687039	0.634175	0.728602	0.740297
6	0.999241	0.547047	0.522879	0.613886	0.607535
7	0.998059	0.681437	0.648173	0.699174	0.705263
8	0.997987	0.546833	0.508177	0.579675	0.58579
9	0.99738	0.613212	0.575476	0.680639	0.680139
10	1	0.429786	0.420115	0.484826	0.480667
11	0.998761	0.52866	0.488899	0.554167	0.558484

Table 10: F1-score of Faster R-CNN Models on test datasets.

Test data ID	Model 1	Model 2	Model 5	Model 4	Model 5
1	0.709821	0.728938	0.742233	0.73615	0.726441
2	0.795035	0.789572	0.778731	0.795145	0.779392
3	0.778915	0.783111	0.785195	0.806737	0.804689
4	0.828608	0.740793	0.752606	0.794457	0.80518
5	0.761325	0.763984	0.73922	0.779562	0.791133
6	0.71184	0.654026	0.631932	0.682053	0.689407
7	0.826865	0.75405	0.741394	0.765668	0.772609
8	0.867756	0.663714	0.639082	0.679991	0.688196
9	0.714491	0.691844	0.670855	0.712246	0.719195
10	0.980491	0.572409	0.566119	0.616104	0.620584
11	0.928558	0.669736	0.639608	0.687947	0.692874

Table 11: Number of rabies virus-infected MNs in ipsilateral and contralateral facial nucleus in higher-order brains.

Higher-order Brains (HB)	Ipsilateral FN	Contralateral FN	Total
HB1	13	0	13
HB2	19	0	19
HB3	21	13	34
HB4	59	33	92
HB5	39	54	93
HB6	73	75	148
HB7	77	80	157
HB8	94	36	130
HB9	101	78	179
HB10	89	113	202

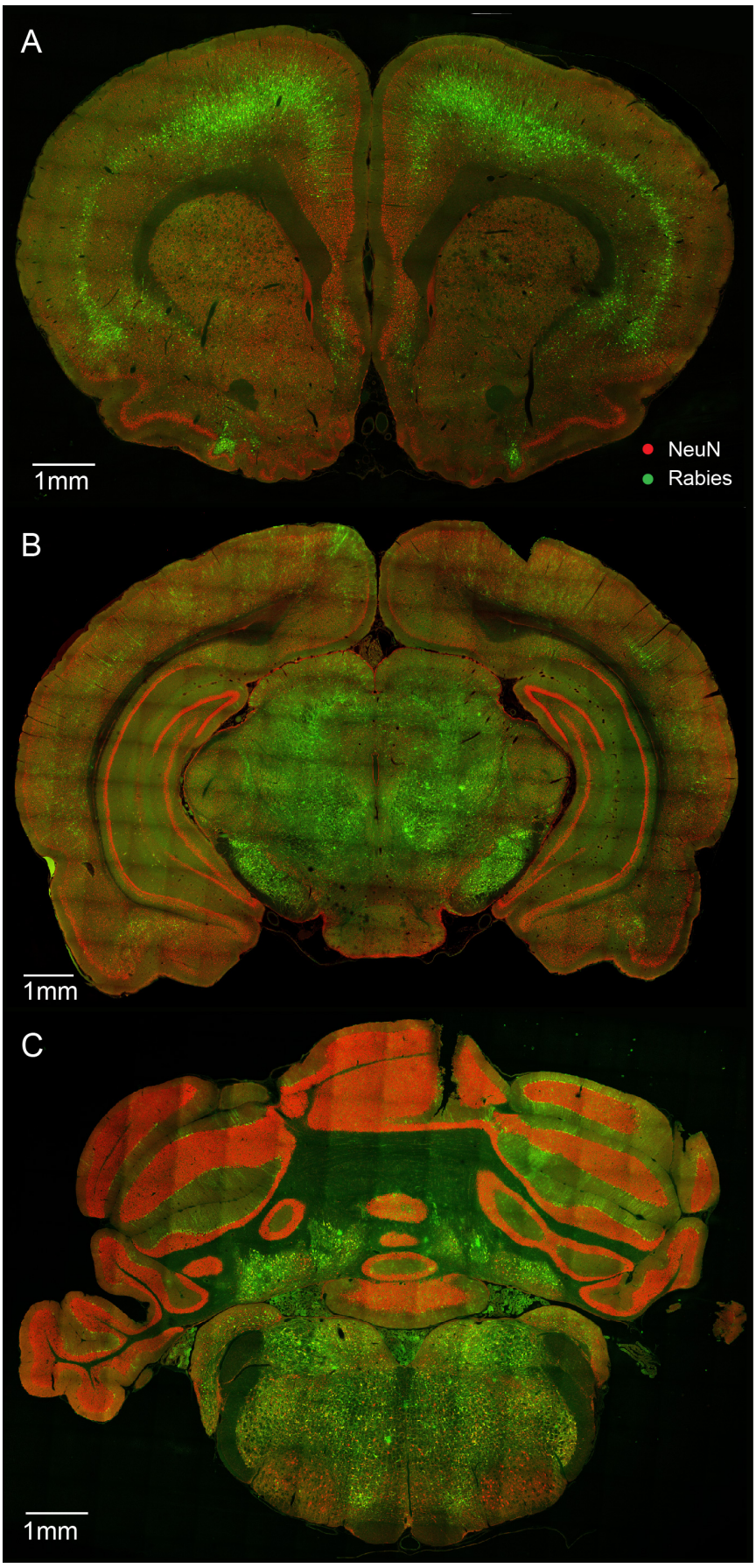

Figure 26: Example confocal images of rabies virus-infected neurons in a higher-order brain (HB2). (A) Cerebral Cortex (B) Midbrain (C) Cerebellum and Brainstem .

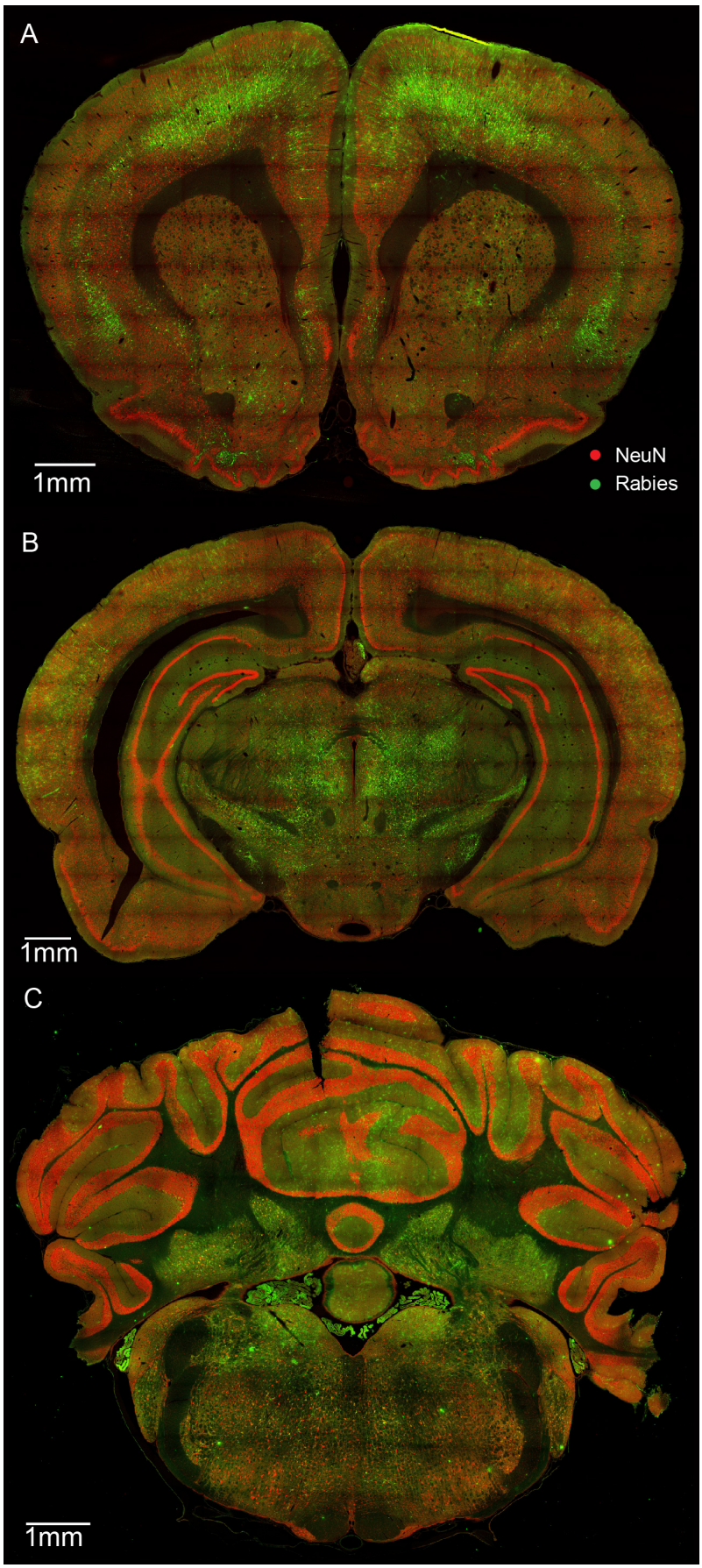

Figure 27: Example confocal images of rabies virus-infected neurons in a higher-order brain (HB3). (A) Cerebral Cortex (B) Midbrain (C) Cerebellum and Brainstem .

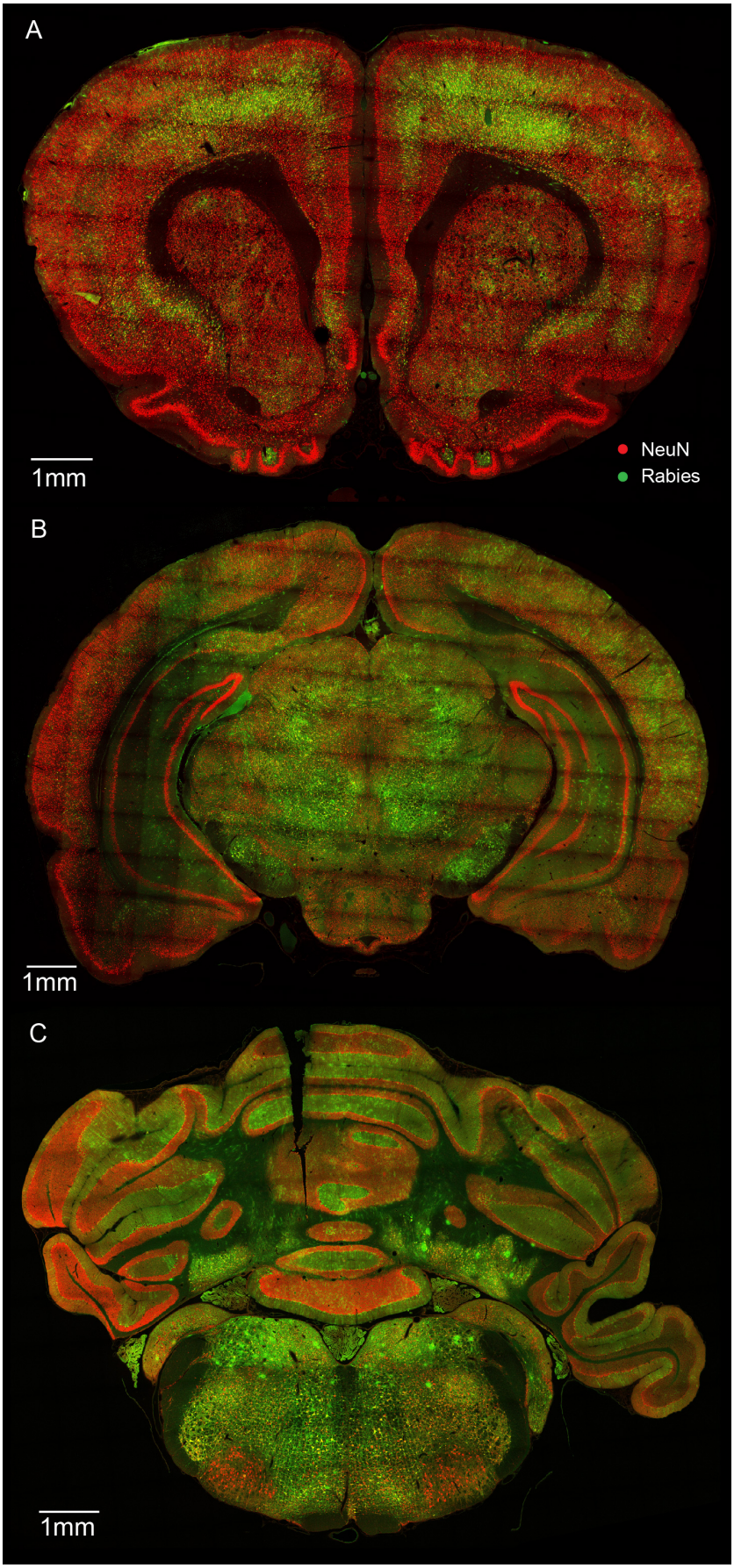

Figure 28: Example confocal images of rabies virus-infected neurons in a higher-order brain (HB4). (A) Cerebral Cortex (B) Midbrain (C) Cerebellum and Brainstem.

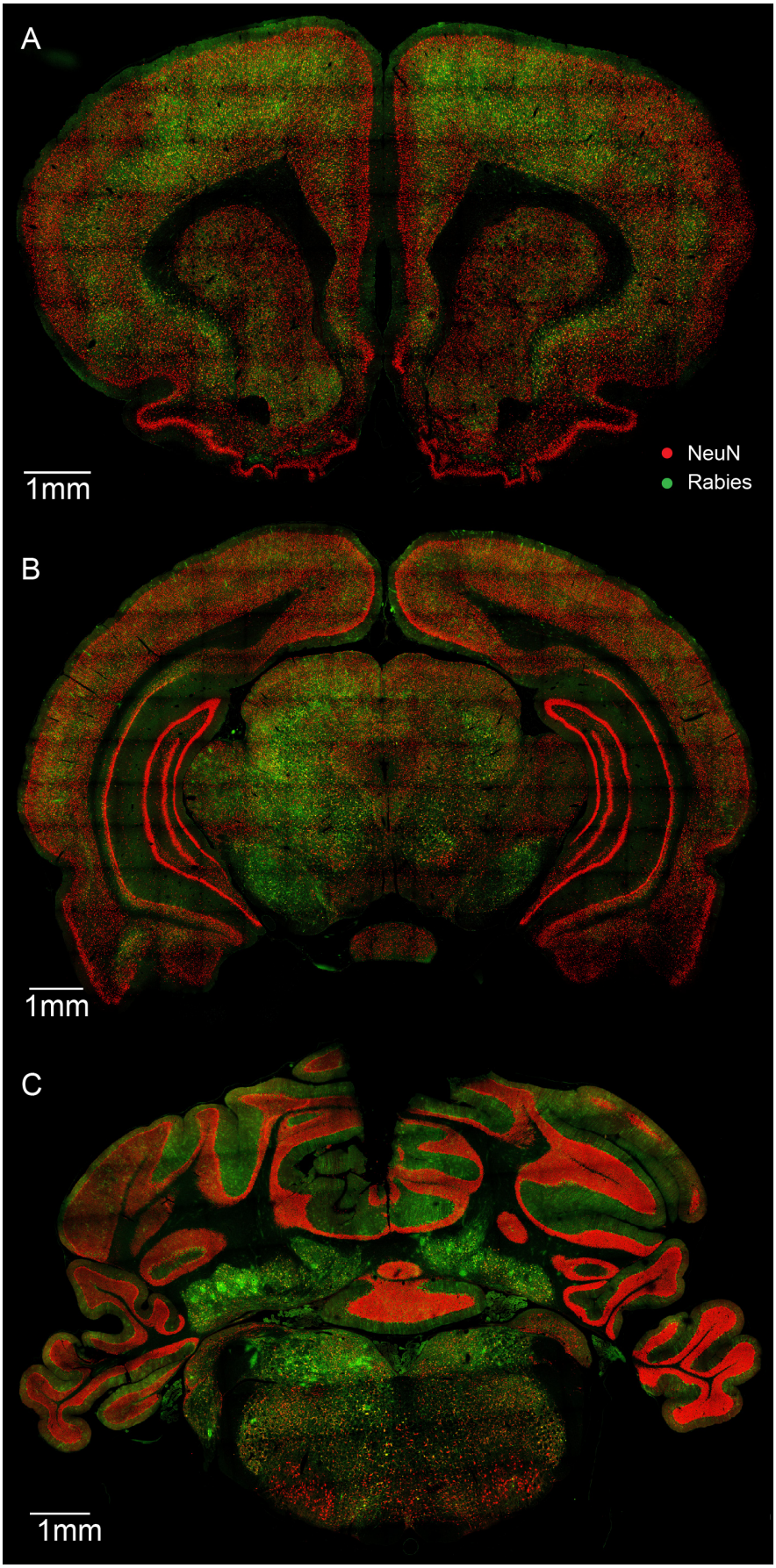

Figure 29: Example confocal images of rabies virus-infected neurons in a higher-order brain (HB5). (A) Cerebral Cortex (B) Midbrain (C) Cerebellum and Brainstem.

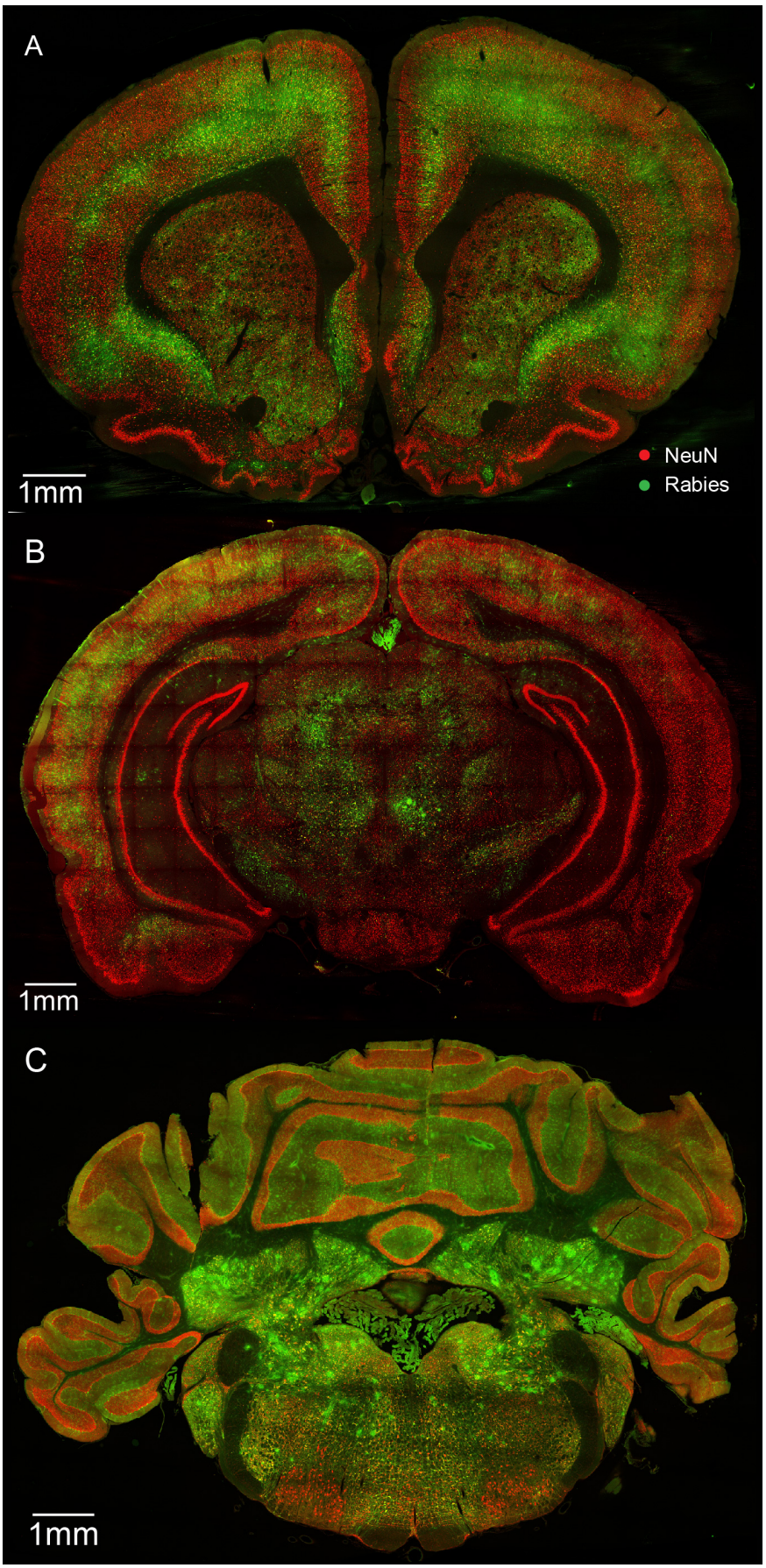

Figure 30: Example confocal images of rabies virus-infected neurons in a higher-order brain (HB6) . (A) Cortex (B) Midbrain (C) Cerebellum and brainstem .

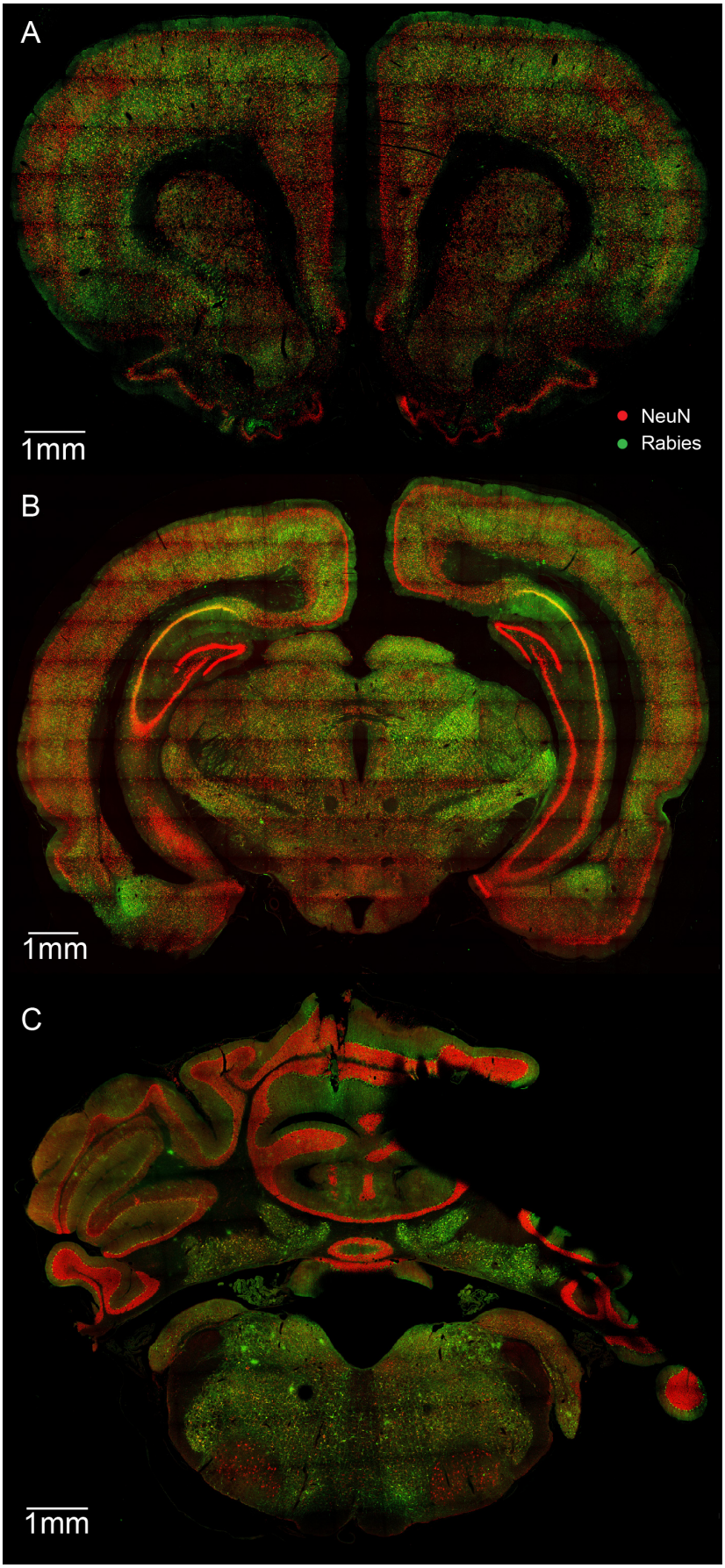

Figure 31: Example confocal images of rabies virus-infected neurons in a higher-order brain (HB7). (A) Cerebral Cortex (B) Midbrain (C) Cerebellum and Brainstem.

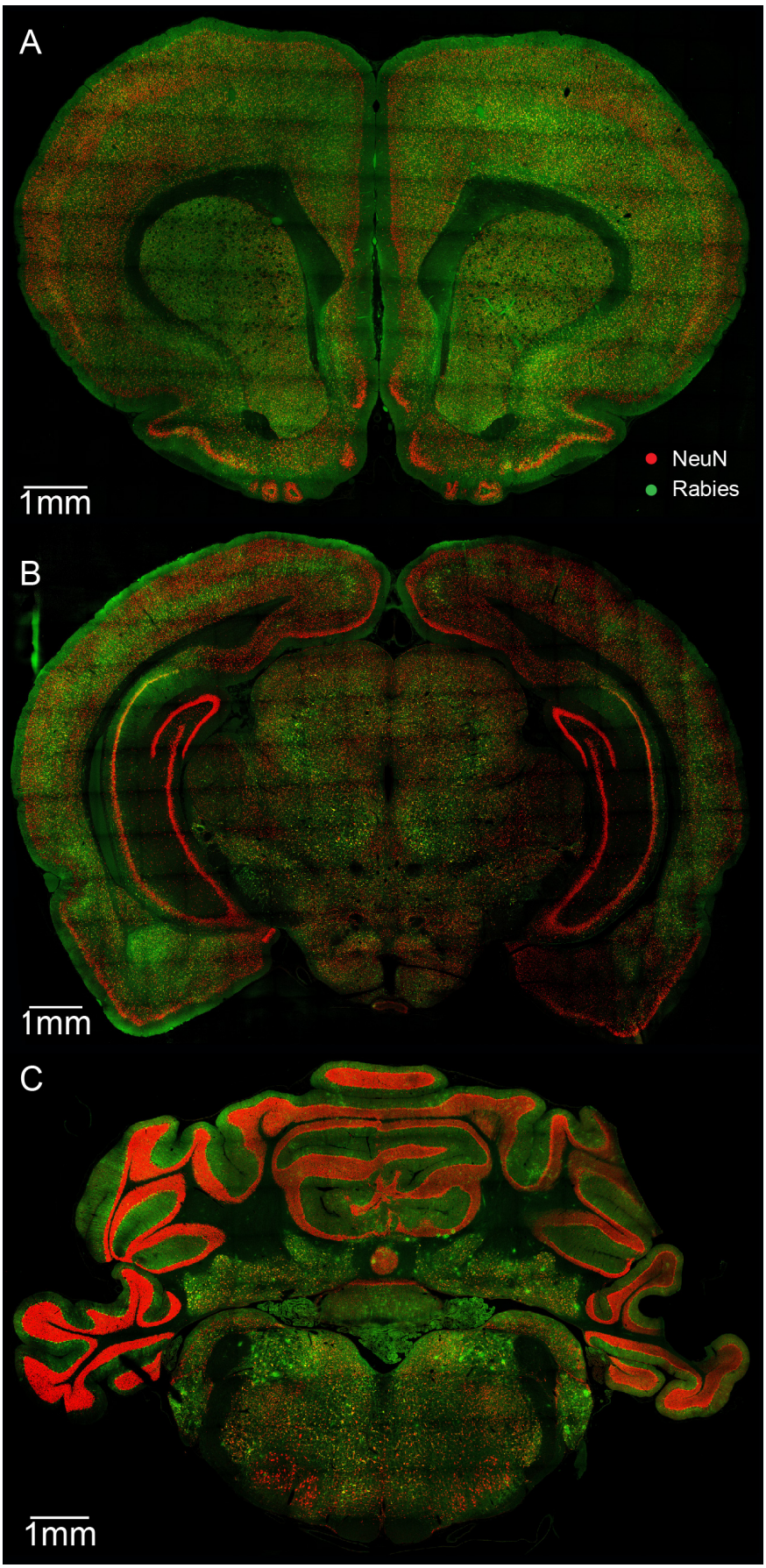

Figure 32: Example confocal images of rabies virus-infected neurons in a higher-order brain (HB8). (A) Cerebral Cortex (B) Midbrain (C) Cerebellum and Brainstem .

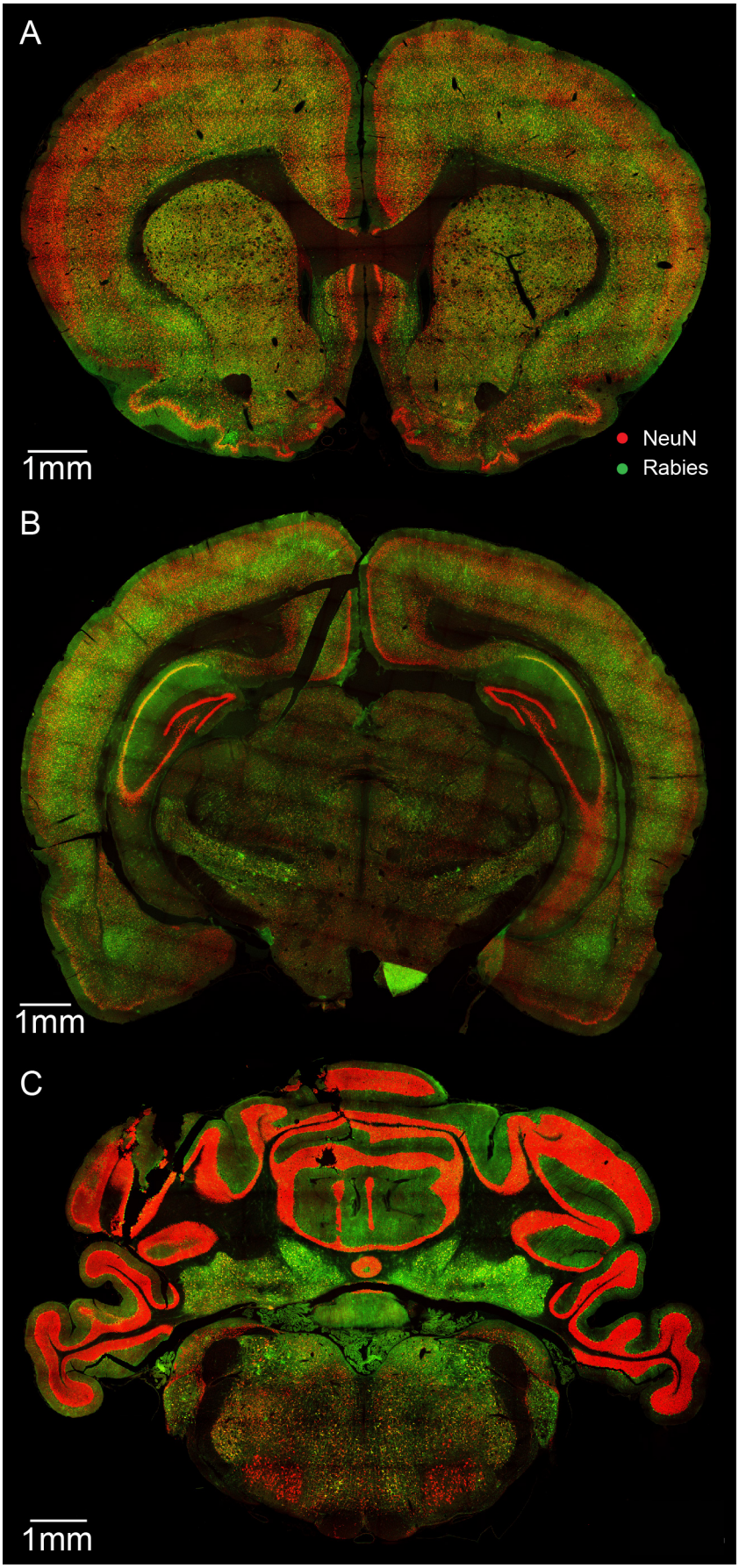

Figure 33: Example confocal images of rabies virus-infected neurons in a higher-order brain (HB9). (A) Cerebral Cortex (B) Midbrain (C) Cerebellum and Brainstem .

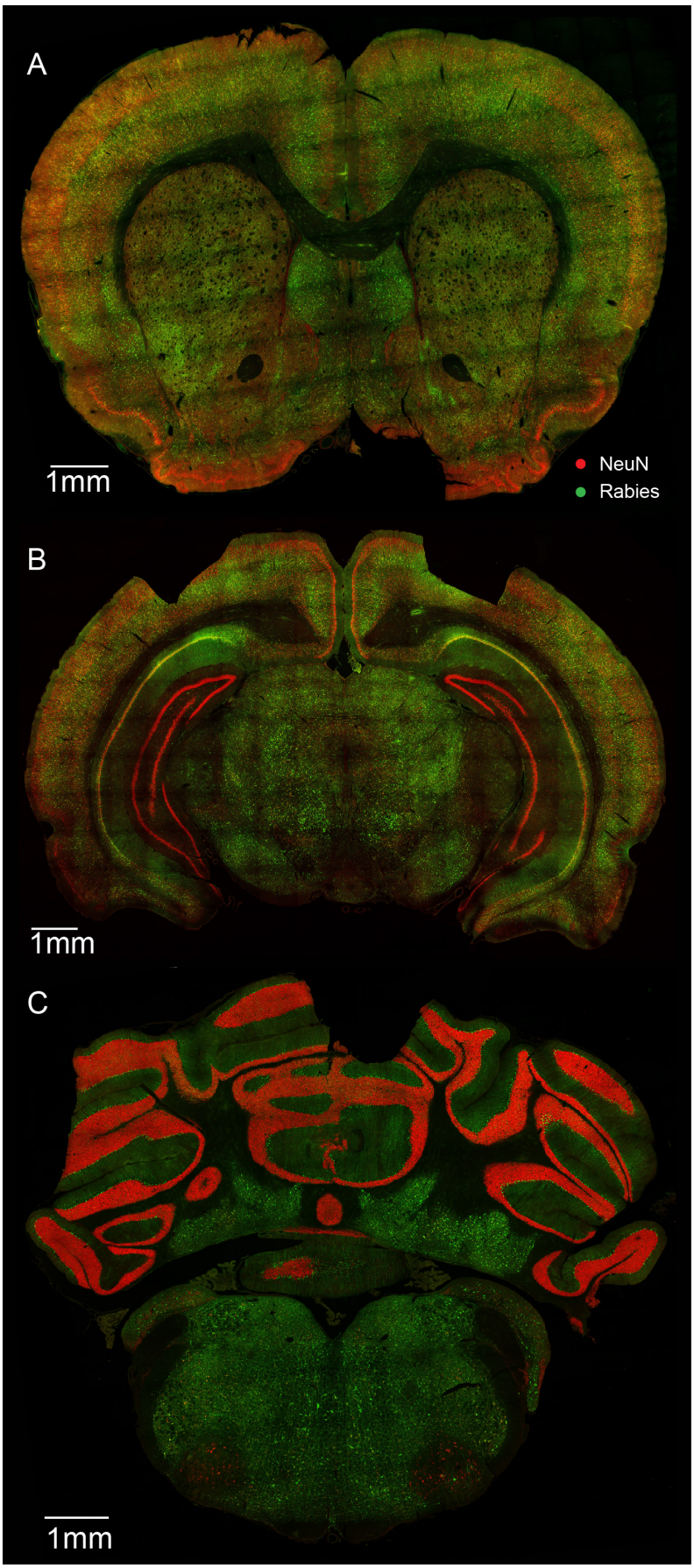

Figure 34: Example confocal images of rabies virus-infected neurons in a higher-order brain (HB10). (A) Cerebral Cortex (B) Midbrain (C) Cerebellum and Brainstem.

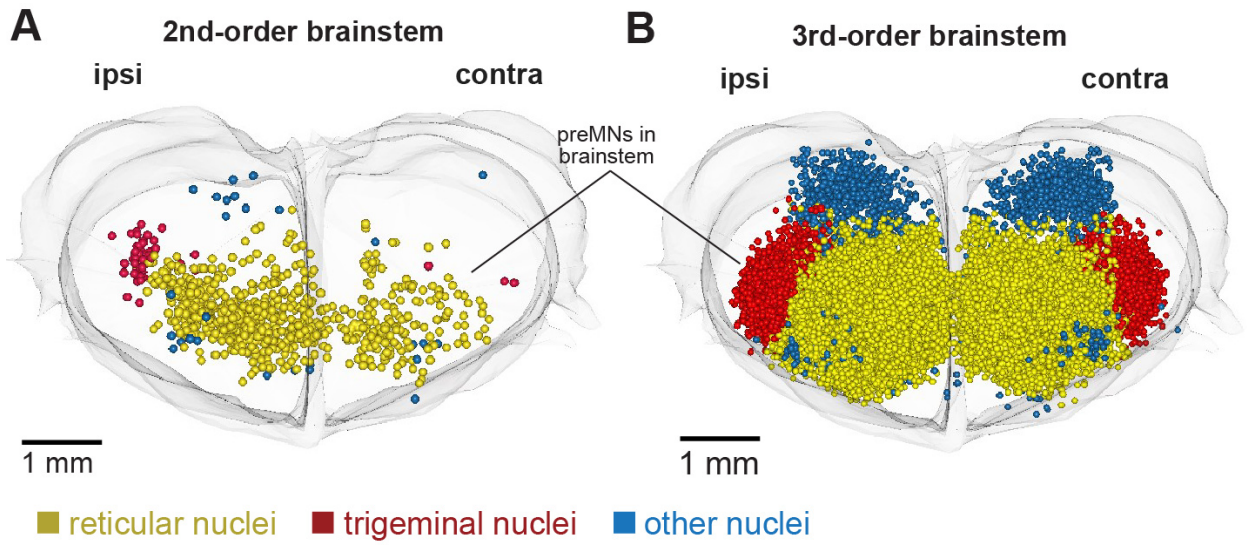

Figure 35: Distribution of rabies-infected neurons in the brainstem of second and third-order brains. (A) Coronal view of average brainstem shows soma locations of all rabies virus-infected neurons from two brains where rabies virus did not spread beyond brainstem. (B) Coronal view of average brainstem shows soma locations of all rabies virus-infected neurons from three brains where rabies virus reached layer 5 pyramidal neurons.

11 Acknowledgements

First, I would like to thank my advisor, Prof. Dr. Marcel Oberlaender. Your support and your expertise have been invaluable in shaping this work and fostering my growth as a researcher.

My thesis advisory committee include, Prof. Dr. Heinz Beck, Prof. Dr. Christian Steinhäuser, and Prof. Dr. Martin Schwarz. Your constructive feedback have been instrumental in refining my research.

I am fortunate to have worked with an incredible group of colleagues. Dr. Mike Guest, who started this project in 2015, was very helpful to continue this work. Mythreya was very helpful in getting me started with analysis of data. Dr. Daniel Udvary, your expertise with all things related to computers in the lab is truly inspiring. Dr. Felipe Yanez and Dr. Fernando Messore, I will certainly miss our engaging conversations and thoughtful feedback. A special thanks to Arco and Rieke for always meticulously reviewing my work, and to Dr. Rajeevan Narayanan for your support and guidance in the lab. Matthew, Maria, Bjorge, and Su, although I could not join the climbing gym, I am always happy to join in on other occasions. I am also grateful to the students I had the privilege of supervising—Fiorella Maria Gomez, Moritz, Keshav, and Kerstin. A special mention to Chantal, Shantanu, Dinuka, Enru, Michelle, and Isabella—it has been a pleasure knowing you, and I hope we stay in touch.

My thesis has been made possible thanks to my collaborators in University of Pittsburgh. Prof. Dr. Peter L. Strick, thank you for your invaluable guidance and expertise. Dr. Jean-Alban Rathelot, I truly appreciate your generosity in sharing your data, which significantly enhanced this project. Special thanks to Mike Page, Dr. Adam Lin, Mitsutoshi Hanada, and Dr. Christina M. Cerkevich—your assistance with flatmap tool and machine learning tool has been incredibly valuable.

I would also like to acknowledge the administrative and technical staff at MPINB-caesar.

A special thank you to Bettina Bosse for your assistance in all the administrative works.

This thesis is dedicated to my parents and my sister, whose unconditional love and belief in me have been the foundation of both my personal and academic journey. To my partner, Shreeya Amatya, your constant support, patience, and sacrifices have been my anchor through every step of this process. To my friends, thank you for bringing joy, balance, and perspective into my life beyond academia.

This thesis would not have been possible without the contributions, encouragement, and belief of all these incredible people. Thank you for being an indispensable part of this journey.